

THE PHYSICS OF MEMBRANE EMULSIFICATION AND
APPLICATIONS FOR CONTROLLED DRUG DELIVERY

Robert Frederick Meyer

A DISSERTATION

in

Chemical and Biomolecular Engineering

Presented to the Faculties of the University of Pennsylvania

in

Partial Fulfillment of the Requirements for the

Degree of Doctor of Philosophy

2010

Supervisor of Dissertation

John C. Crocker

Associate Professor, Chemical and Biomolecular Engineering

Graduate Group Chairperson

Raymond J. Gorte

Professor, Chemical and Biomolecular Engineering

Dissertation Committee

Steven J. Siegel, Associate Professor, Psychiatry

Talid R. Sinno, Associate Professor, Chemical and Biomolecular Engineering

Kathleen J. Stebe, Professor and Chair, Chemical and Biomolecular Engineering

Karen I. Winey, Professor, Chemical and Biomolecular Engineering

For Laura Lynn Meyer

Thank you!

Acknowledgements

This thesis would be incomplete without an acknowledgement of those who contributed to its successful completion. When I began the journey towards this degree in the spring semester of 2004, the day that I write the acknowledgements section of my thesis seemed infinitely far away. At the start, the only encouragement I received was from my wife Laura. Yet throughout the journey, I've met many kindred spirits who have helped me along the way.

Of course, the first set of people I think of are my fellow members of the Crocker Lab. Coming from industry where every project is a group effort, the solitude of graduate research proved challenging at times. Despite the lack of similarity when comparing our research, Ben Rogers provided the sounding board that kept me going, and helped me realize the difference between a regular crazy idea, and a crazy idea that just might work. The unmatched work ethic of Marie Ung always drove me to try harder. Klebert Feitosa, Valeria Garbin and Shang Tee provided the perspective of someone who had completed their PhD. And when I needed a break, everyone was always willing to stop what they were doing to go search for the perfect cup of coffee – despite the fact that no one else likes coffee.

I should note that the final fifteen months of my time in graduate school were spent while concurrently working full time at Merck & Co. This dual workload weighed heavily on my body and mind, and thus maintaining focus on finishing successfully proved challenging. However, through a fortunate twist of fate, a Crocker Lab alumnus landed a job at Merck and bought a house near mine, and thus my car pool relationship

with Kathleen Van Citters was born. Suffice it to say, during my time riding with Kathleen, we invented the phrase "car pool therapy". If these last fifteen months were compared to Dante's Inferno, then Kathleen was my Virgil.

The kindred spirits outside my lab also deserve praise. First, I admire the ability of Brendon Ricart to defeat me in anything resembling a competition. As a fellow engineer on leave from Merck, we already had a lot in common, but what I found most valuable was what he taught me about life, liberty, and most importantly, the pursuit of happiness. Second, Calixte Monast proved to me that there is at least one other person on this planet that likes my music. Finally, Michael Beste provided the guidance of a tenured professor while still being a graduate student. Of course they all deserve the traditional thanks of providing help when I needed it, but those specific items set them apart.

John Crocker deserves a paragraph to himself. When I tracked him down one day after his lecture, and pitched to him the seeds of a research project, he took those seeds and helped them grow into this thesis. Even though I came from industry, and couldn't pay him for his time, he took me in and gave me a home in his lab. All he asked for in return was a few publications, preferably publications that will eventually be cited. It would be impractical to list all that I've learned from him, but suffice it to say, he's taught me more than any teacher I had before him.

I am grateful to Merck & Co., Inc. for giving me the time off to pursue this degree. And there have been many at Merck that have made this dissertation possible. I specifically want to thank Bill Egan, Celia Cruz, Neil MacPhail and Scott Reynolds for helping me along the way.

Finally, I have to thank my family. First on the list, of course, is my lovely wife Laura. Of the fifteen years we've been dating or married, I've been in school for thirteen of them, and she has encouraged me every step of the way. Of course, freshly brewed coffee was one important form of encouragement. I'm not sure what our life will look like after October 4th, 2010, but I'm looking forward to it. Grady the dog and Mowgli the cat provided a furry back to scratch when I needed a break from typing. And Carter Thomas Meyer, age two at the time of this writing, let me know that there are things more important in life than graduate research. Finally, Carter's Aunt Jenni and Uncle Chris, thank you for everything you've done, not least of which is entertaining Carter when he thought that playing was more important than graduate research.

ABSTRACT

THE PHYSICS OF MEMBRANE EMULSIFICATION AND APPLICATIONS FOR CONTROLLED DRUG DELIVERY

Robert F. Meyer

John C. Crocker

In many applications employing particles, the distribution of particle sizes has significant influence over the properties of the resultant material, and this holds especially true for many pharmaceutical products. In the case of depot formulations made of drug-loaded polymer microspheres, particle size significantly impacts the rate and duration of drug release. Thus, if particle size can be controlled, formulation characteristics can be engineered to better meet the needs of the specific situation. Cross-flow membrane emulsification (XME) is a method for manufacturing uniformly sized emulsion droplets which can be used for many applications, including production of drug-loaded polymer microspheres. In XME, a dispersed phase is forced through an orifice in a planar membrane into a simple shear flow set up by a second continuous phase flowing parallel to the membrane surface, thereby generating an emulsion. Though XME has become a popular technique for researchers generating monodisperse emulsions, there has been insufficient characterization of the physics of the XME

process. This is true for both simple binary fluid systems, as well as the more complex fluid systems used for the generation of drug-loaded microspheres. In this work, we describe a unique XME system that allows for visualization of the process, providing access to details likely unseen by previous researchers. First employing our system for the study of pure fluids, we successfully show that a simple force balance can be used to model the size of emulsion droplets as a function of process conditions. We also show that the range of applicability of our model corresponds to the region of simple fluid dripping, and that the XME process undergoes a dripping-jetting transition much like the common household faucet. Extending the methods to a more complex case when dissolved polymers, drugs and surfactants are present, we find generally that our earlier results hold true, but only if dynamic interfacial tension is taken into account. Ultimately we show that drug-loaded polymer microspheres of uniform size can be reliably and predictably manufactured across a range of process conditions, and thus we conclude that XME has the potential to produce advanced controlled release formulations.

Table of Contents

ACKNOWLEDGEMENTS	III
ABSTRACT	VI
TABLE OF CONTENTS	VIII
LIST OF TABLES	XII
LIST OF FIGURES	XIII
CHAPTER 1: INTRODUCTION	1
1.1 RESEARCH MOTIVATION	1
1.2 BACKGROUND.....	2
1.3 RESEARCH AIMS	4
1.4 THESIS OUTLINE	5
1.5 REFERENCES	7
CHAPTER 2: LITERATURE REVIEW	9
2.1 MARKETED LONG ACTING RELEASE MEDICATIONS AND THEIR FORMULATIONS	9
2.2 METHODS OF MANUFACTURE FOR LONG ACTING RELEASE FORMULATIONS	11
2.3 METHODS OF MANUFACTURE FOR UNIFORMLY SIZED EMULSIONS	12
2.4 REVIEW OF CROSS-FLOW MEMBRANE EMULSIFICATION	16
2.5 APPLICATION OF CONTROLLED EMULSIFICATION FOR ENGINEERED DRUG RELEASE.....	20
2.6 REFERENCES	21
CHAPTER 3: MATERIALS, METHODS, AND PRELIMINARY RESULTS	23
3.1 CROSS-FLOW MEMBRANE EMULSIFICATION.....	23
3.1.1 <i>Membrane Emulsifier</i>	24
3.1.2 <i>Microscope and optics</i>	30

3.1.3	<i>Computer and Data Acquisition System</i>	31
3.2	CONTINUOUS PHASE AND DISPERSED PHASE FLUID PREPARATION	33
3.2.1	<i>Simple Systems</i>	33
3.2.2	<i>Complex Systems</i>	33
3.3	PHYSICAL PROPERTY MEASUREMENTS.....	34
3.3.1	<i>Viscosity</i>	34
3.3.2	<i>Density</i>	35
3.3.3	<i>Interfacial Tension</i>	35
3.3.4	<i>Pendant Drop Profile Analysis</i>	36
3.3.5	<i>Drop Weight Method</i>	40
3.3.6	<i>Contact Angle Analysis</i>	43
3.4	PRELIMINARY RESULTS FROM PHYSICAL PROPERTY MEASUREMENTS	44
3.4.1	<i>Interfacial tension measurements of normal alcohols</i>	44
3.4.2	<i>Physical properties of binary solutions of n-hexanol and dichloromethane</i>	45
3.4.3	<i>Viscosity of polymer solutions</i>	46
3.4.4	<i>Zimm theory</i>	49
3.5	SIZING OF MICROSPHERES	50
3.6	DOWNSTREAM PROCESSING OF DRUG AND POLYMER LOADED EMULSION DROPLETS	50
3.7	COMPUTATIONAL FLUID DYNAMICS	51
3.7.1	<i>Continuous Phase Flow Simulations</i>	51
3.7.2	<i>Cross-flow membrane emulsification simulations</i>	53
3.7.3	<i>Cross-flow membrane emulsification simulation results</i>	54
3.8	MODEL DRUG HALOPERIDOL.....	55
3.9	IN VITRO DRUG RELEASE MEASUREMENT SYSTEM	56
3.9.1	<i>Drug release microenvironment</i>	56
3.9.2	<i>Reactor and Flow System</i>	57
3.9.3	<i>Dual-Channel Spectrophotometer</i>	58

3.9.4	<i>Pure haloperidol dissolution experimental results</i>	63
3.10	MATHEMATICS OF FLUID FLOW THROUGH A RECTANGULAR CHANNEL.....	64
3.11	REFERENCES	67
CHAPTER 4: UNIVERSAL DRIPPING AND JETTING IN A TRANSVERSE SHEAR FLOW .68		
4.1	INTRODUCTION	69
4.2	METHODS.....	70
4.3	QUALITATIVE RESULTS	71
4.4	DEVELOPMENT OF DROPLET SIZE MODEL	72
4.5	MODELING OF THE DRIPPING-JETTING TRANSITION	76
4.6	SUMMARY	79
4.7	ACKNOWLEDGEMENTS.....	80
4.8	REFERENCES	80
CHAPTER 5: PRODUCING MONODISPERSE DRUG-LOADED POLYMER		
MICROSPHERES VIA CROSS-FLOW MEMBRANE EMULSIFICATION: THE EFFECTS OF		
POLYMERS AND SURFACTANTS82		
5.1	INTRODUCTION	83
5.2	BACKGROUND.....	85
5.3	METHODS.....	87
5.3.1	<i>Experimental Apparatus</i>	87
5.3.2	<i>Membranes</i>	88
5.3.3	<i>Video Microscopy</i>	89
5.3.4	<i>Materials</i>	90
5.3.5	<i>Preparation of CP and DP</i>	91
5.3.6	<i>Microsphere Drying</i>	91
5.3.7	<i>Sizing of Microspheres</i>	91
5.3.8	<i>Physical Properties</i>	92

5.3.9	<i>Calculation and Measurement of Channel Shear Rate</i>	93
5.4	RESULTS AND DISCUSSION.....	94
5.5	SUMMARY.....	112
5.6	ACKNOWLEDGEMENTS.....	113
5.7	REFERENCES.....	113
CHAPTER 6: FUTURE WORK.....		115
6.1	FORMULATION REQUIREMENTS.....	115
6.2	PREVIOUS STUDIES OF HALOPERIDOL LAR FORMULATIONS.....	119
6.3	FUTURE XME AND IN VITRO RELEASE EXPERIMENTS.....	119
6.4	ACHIEVING THE OPTIMAL RELEASE PROFILE.....	121
6.5	REFERENCES.....	123

List of Tables

Table 3.1 – Summary of pore dimensions of membranes used for XME.	26
Table 3.2 – Scale calibration factors for lenses used to view XME.	32
Table 3.3 – Sensor calibration values.	33
Table 3.4 – Definitions of viscosity terms.	47
Table 3.5 – Physical properties of fluids in Fluent simulation.....	53
Table 3.6 – Physical and chemical properties of haloperidol.	56
Table 4.1 – Liquids used and some of their physical properties at 18°C.....	71
Table 5.1 – Formulations of decanol and polymer-loaded systems.....	91
Table 5.2 – Physical properties of decanol and polymer-loaded systems.	93
Table 5.3 – Rosen equation fit parameters.....	104
Table 6.1 – Pharmacokinetic parameters for haloperidol.	117
Table 6.2 – Starting compositions for once monthly haloperidol LAR formulation.	120

List of Figures

Figure 1.1 – Pharmacokinetic profiles of immediate release (IR) and long acting release (LAR) formulations of naltrexone.	3
Figure 2.1 – Oil-in-water emulsion / solvent extraction method for producing drug-loaded polymer microspheres.	12
Figure 2.2 – Diagram of cross-flow membrane emulsification (XME).	16
Figure 3.1 – Schematic of the XME process and important parameters.	23
Figure 3.2 – Representation of membrane emulsifier flow channels, membrane & optical path.	24
Figure 3.3 – Bottom view of membrane holder top, and top view of membrane holder bottom.	25
Figure 3.4 – SEM images of laser and mechanically drilled membranes.	27
Figure 3.5 – SEM images of electrical discharge machined membranes.	28
Figure 3.6 – Process flow diagram for XME.	30
Figure 3.7 – Diagram of microscope system used during membrane emulsification experiments.	31
Figure 3.8 – Ubbelohde viscometer.	35
Figure 3.9 – Instrument set up used for interfacial tension measurements.	35
Figure 3.10 – Coordinate system for pendant drop profile analysis.	36
Figure 3.11 – Drop of 1-pentanol in water attached to 90 μm pore.	38
Figure 3.12 – Laplace equation fit to 1-pentanol image edge coordinates.	38
Figure 3.13 – Volume and surface expansion rates during PDPA.	40
Figure 3.14 – Average interfacial tension and relative standard deviation during PDPA.	40
Figure 3.15 – Calculated drop period and corresponding flow rate to maintain $We = 0.1$	43
Figure 3.16 – Schematic of pendant or sessile drops during contact angle experiments.	44
Figure 3.17 – Inverted image of water + 1% PVA on SS in a medium of DCM.	44
Figure 3.18 – Comparison of experimental and reported values of interfacial tension at 20°C.	45
Figure 3.19 – Physical properties of mixtures of n-hexanol and dichloromethane.	46
Figure 3.20 – Viscosity dependence on polymer concentration for PLG dissolved in DCM.	48
Figure 3.21 – Shear viscosity dependence on polymer concentration for PLG dissolved in DCM.	48
Figure 3.22 – Contours of velocity magnitude calculated in Fluent.	52
Figure 3.23 – Computational mesh used for CFD simulations of membrane emulsification.	53
Figure 3.24 – Volume fraction contours shown at the symmetry plane during a cross-flow membrane emulsification simulation.	54
Figure 3.25 – Dimensionless droplet diameter vs. capillary number from Fluent simulations.	55
Figure 3.26 – Haloperidol molecular structure.	55
Figure 3.27 – Reactor and flow system used for drug release studies.	58
Figure 3.28 – Spectrophotometer optics and electronics configuration.	60
Figure 3.29 – Timing circuit and peak-hold circuit used within the spectrophotometer.	61
Figure 3.30 – Calibration curve of spectrophotometers using haloperidol.	62
Figure 3.31 – Haloperidol dissolution into PBS at 37°C with 0.02% sodium azide and 1% polysorbate 20.	64
Figure 3.32 – Geometry of a rectangular channel.	64
Figure 3.33 – Velocity profiles calculated for flow in a rectangular duct.	66
Figure 4.1 – Dripping and jetting at various We for $Ca = 8 \times 10^{-4}$ and $Oh_{DP} = 4 \times 10^{-2}$	72
Figure 4.2 – Droplet diameter D versus shear rate $d\nu/dz$ for all fluid systems, and collapse of scaled droplet size $(1/k)D/D_0$ as a function of Ca	75
Figure 4.3 – Increase in neck length L_n relative to droplet diameter D as We is increased, and corresponding decrease in droplet diameter ratio D/D_0 as the dripping-jetting transition $L_n/D = 1$ is exceeded.	77
Figure 4.4 – Dripping to jetting phase behavior as a function of We , Ca and Oh_{DP}	78
Figure 5.1 – Schematic of the XME process and the important parameters, and scale rendering of the CP fluid channel, membrane and optical path.	84
Figure 5.2 – Membranes manufactured via different methods.	89

Figure 5.3 – Example images of PLG droplets.....	90
Figure 5.4 – Drop diameter as a function of CP shear rate for the PLG and decanol systems.	94
Figure 5.5 – Drop diameter as a function of DP flow rate Q_{DP} or velocity v_{DP} for the PLG and decanol systems.	95
Figure 5.6 – Distance from membrane surface as a function of continuous phase velocity v_{CP} for the PLG system with a CP containing 1% PVA.....	97
Figure 5.7 – Droplet neck diameter D_n as a function of time t for the PLG and decanol systems.....	99
Figure 5.8 – Interfacial tension γ as a function of drop period Δt for the PLG and decanol systems, as measured using the drop weight method.	102
Figure 5.9 – Interfacial tension γ as a function of drop period Δt for the PLG and decanol systems as calculated during XME.....	103
Figure 5.10 – Scaled diameter ratio $(1/k)D/D_0$ as a function of capillary number Ca for the PLG and decanol systems.....	106
Figure 5.11 – Diameter histograms for wet and dry drug loaded PLG particles produced over a 10min time period, measured independently via image analysis.	107
Figure 5.12 – Fully dry drug loaded PLG particles produced over a 10min time period.	107
Figure 5.13 – Droplet deformation D_r , and droplet size D/D_0 as a function of Ca_{drop} for the PLG system.....	110
Figure 5.14 – Ratio of Ca to the critical value Ca_c where droplet rupture occurs, calculated as a function of the diameter ratio D/D_0 and viscosity ratio λ	111
Figure 6.1 - Plot of average haloperidol blood serum concentration following a loading dose regimen of 100 mg haloperidol equivalent (administered as haloperidol decanoate).....	118

Chapter 1: Introduction

1.1 Research Motivation

For many chronic conditions, the success a drug has in managing a disease is directly related to how well the drug concentration is maintained within the therapeutic window that maximizes efficacy and minimizes side effects. Traditional drug therapy usually consists of an oral dosage form that is administered once daily. Although this has been standard for many years, this route of administration can lead to variability due to many factors, including poor patient compliance to the recommended dosing schedule, and interaction of the drug or formulation with food and drink. Furthermore, this administration route suffers from the drawbacks that many drugs are degraded or poorly absorbed in the gut, and first-pass metabolism can significantly reduce the amount of drug that reaches circulation. Oral administration also results in a drug being dosed to the entire body, rather than being delivered to only the desired location. Because these mechanisms increase the total amount of drug that must be administered to reach the target concentration in the blood, and because different patients absorb and metabolize drugs differently, significant variability can be seen between patients taking oral medication. Ultimately, deviation of drug concentration outside of the therapeutic window can lead to a higher incidence of side effects or relapse, and in some instances, it can lead to patient hospitalization.

Parenteral drug formulations circumvent many problems associated with oral administration, and thus have inherent advantages over traditional therapy. Although they are more expensive to manufacture and generally must be administered by a medical

professional, parenterals have benefits such as lower dose, local delivery, and reduced variability between patients. Long acting release (LAR) parenteral formulations in particular have been shown to improve patient compliance, reduce drug variability and side effects, improve clinical outcomes, and decrease hospitalizations and the cost of care¹⁻⁴. For these reasons, advancing the science geared towards development of such treatment forms is a valuable research goal.

1.2 Background

There are many approaches for developing LAR parenteral formulations, and embedding drug in a matrix of polymer is certainly one of the more popular strategies. In a classical method used to manufacture drug-loaded microparticles, an organic solvent is mixed with drug and a biodegradable polymer to form the dispersed phase, while water and surfactant form the continuous phase. The dispersed phase is emulsified in the continuous phase, and then the organic solvent is extracted and evaporated, resulting in solid drug-loaded polymer microspheres. After washing and drying, the microspheres form a drug product suitable for parenteral administration. Microspheres such as these have been developed as several drug products used to provide release periods ranging from 1 week to 6 months.

There have been at least 10 commercial products of this type developed for the U.S. market over the last 20 years⁵. Although these LAR products all improve upon formulations that are administered daily, no formulation has achieved the gold standard of a constant drug release rate over an extended period. Instead, current LAR formulations reduce the daily rise and fall of drug levels in the body, and instead provide

drug levels that rise and fall a few times a month. As an example of this, we examine clinical data from a study that compared an oral and LAR formulation of naltrexone, an opioid receptor antagonist used for treatment of alcohol dependence.

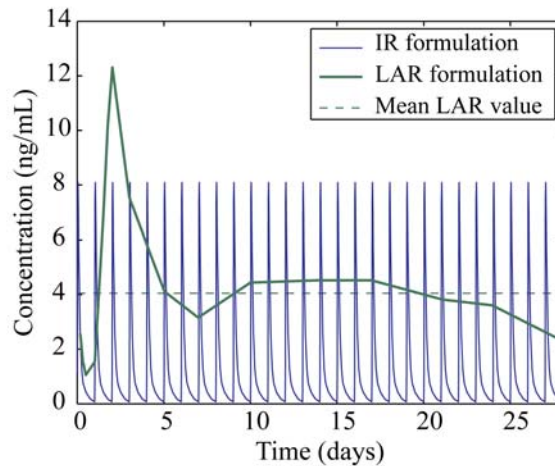


Figure 1.1 – Pharmacokinetic profiles of immediate release (IR) and long acting release (LAR) formulations of naltrexone.

Figure 1.1 displays our graphical representation of pharmacokinetic data extracted from a clinical study comparing an immediate release (IR) 50 mg once-daily oral dose of naltrexone to a LAR 380 mg once-monthly intramuscular microsphere injection³. For drugs such as naltrexone, the optimal formulation would rapidly raise the level of drug in the patient's blood stream to the desired concentration, and would then maintain that same concentration, releasing additional drug at the same rate that the body eliminates it from circulation. The LAR formulation clearly eliminates the daily rise and fall of drug levels in the blood when compared to the IR formulation, but it is far from the ideal formulation, which would maintain concentrations at near constant levels. Instead, it exhibits a tri-phasic release profile, with peaks on days 0, 3 and ~15. Although this is not of significance for this drug, in many cases the spike seen in the LAR formulation can

cause increased side effects or disease flare-up⁶. Thus, microsphere formulations that can better control rate and extent of drug release will in many cases result in improved patient care and better clinical outcomes.

Because drug is released from microspheres by both diffusion through and degradation of the polymer matrix, stringent control over particle size is a convenient method for manipulating release rate. This general concept has been demonstrated by several researchers who used high shear emulsification to produce microspheres with wide particle size distributions, then sieved the product into several size fractions, each with its own unique release profile⁷⁻⁹. The transport of drug through the microspheres was modeled as a function of particle diameter, while also taking polymer degradation rate into account. Finally, Berchane et al.⁹ showed that by mixing microspheres with different sizes and polymer molecular weights, they could achieve a pre-specified release profile.

1.3 Research Aims

Because most emulsification techniques used for generating polymer microspheres result in polydisperse particle size distributions, a technique that allows for accurate and precise particle size control would be a significant improvement in the state of the art. In this thesis, we aim to develop a robust and scalable manufacturing method for continuously producing sterile monodisperse polymer microspheres. We aim to develop a theoretical understanding of how process conditions affect particle size, by first studying the emulsification of pure, simple fluids. Then we aim to expand this understanding to non-ideal fluid systems used for generating drug-loaded polymer

microspheres. We aim to use this understanding to demonstrate our manufacturing method's utility for producing large quantities of drug loaded polymer microspheres. Finally, we aim to lay the groundwork for developing an ideal microsphere formulation exhibiting the desired rate and extent of release, including development of a system for testing this drug release in vitro.

1.4 Thesis Outline

This thesis is organized as follows. In Chapter 2, we first review polymer-based controlled release dosage forms in general. Then we look at the methodology for generating polymer microsphere formulations using emulsification followed by solvent extraction and evaporation. With that as a backdrop, we review the state of the art for producing monodisperse emulsions, including the methods of manufacture and mathematical descriptions of the processes. We focus this review specifically on the technique known as cross-flow membrane emulsification. Then we examine research where monodisperse emulsions were produced from systems containing polymers and surfactants. Finally, we review in greater detail instances where control over particle size was used as a method to manipulate drug release from polymer microsphere formulations.

In Chapter 3, we describe the materials and methods used in this research. Specifically, we describe the apparatus that we developed for manufacturing monodisperse emulsions. We also describe the equipment and methods for examining the emulsion production process. We explain our techniques for measuring physical properties relevant to emulsions, and some results from those measurements. And we

give details on efforts to characterize our emulsification system, through both basic mathematical as well as more advanced numerical modeling. Finally, we provide additional details on the materials used to generate polymer microparticles, the model drug we load into the particles, and our method for measuring drug release from the particles.

In Chapter 4 we describe the production of monodisperse emulsions of simple fluids using cross-flow membrane emulsification. This work, titled "Universal Dripping and Jetting in a Transverse Shear Flow", has been previously published in *Physical Review Letters* in May 2009.¹⁰ A model for predicting the size of droplets as a function of system geometry, process flow rates and physical properties is presented. We also describe where the system transitions from dripping to jetting, and draw comparisons to the well-studied case of the dripping faucet.

Chapter 5 describes our efforts to expand cross-flow membrane emulsification from simple, pure fluid systems to more complicated systems containing dissolved polymers and surfactants. This work, titled, "Producing Monodisperse Drug-Loaded Polymer Microspheres via Cross-Flow Membrane Emulsification: The Effects of Polymers and Surfactants", was previously published in *Langmuir* in September 2010.¹¹ We show that emulsions generated from both simple and complex fluids can be produced across a range of sizes and rates, and the models that describe the size of the resultant droplets work reasonably well for both systems. We show that dynamic interfacial tension affects the size of droplets, especially at low production rates, but that fluid viscosity and elasticity behave ideally under the conditions studied. Finally, we show

that cross-flow membrane emulsification can be used to generate highly uniform solid drug-loaded polymer microspheres.

Chapter 6 contains a description of future work that could be performed to translate the demonstrated manufacturing methods into a commercializable formulation of a model drug, haloperidol. Literature is reviewed that describes LAR formulations of haloperidol, including a manuscript that we contributed to, "A rapid method for creating drug implants: Translating laboratory-based methods into a scalable manufacturing process", published in the *Journal of Biomedical Materials Research Part B: Applied Biomaterials* in May 2010.¹² Specifically, we lay out the calculations for what a 30 day LAR formulation of haloperidol would look like, and describe the emulsification and in vitro release experiments to be performed in order to achieve the goal of generating an ideal drug release profile.

1.5 References

- (1) Kane, J. M.; Garcia-Ribera, C. *The British Journal of Psychiatry* **2009**, *195*, S63-67.
- (2) Chue, P.; Eerdeken, M.; Augustyns, I.; Lachaux, B.; Molcan, P.; Eriksson, L.; Pretorius, H.; David, A. S. *European Neuropsychopharmacology* **2005**, *15*, 111-117.
- (3) Dunbar, J. L.; Turncliff, R. Z.; Dong, Q.; Silverman, B. L.; Ehrich, E. W.; Lasseter, K. C. *Alcoholism: Clinical and Experimental Research* **2006**, *30*, 480-490.
- (4) Ewend, M. G.; Brem, S.; Gilbert, M.; Goodkin, R.; Penar, P. L.; Varia, M.; Cush, S.; Carey, L. A. *Clinical Cancer Research* **2007**, *13*, 3637-3641.
- (5) Wischke, C.; Schwendeman, S. P. *Int. J. Pharm.* **2008**, *364*, 298-327.
- (6) Woo, B. H.; Kostanski, J. W.; Gebrekidan, S.; Dani, B. A.; Thanoo, B. C.; DeLuca, P. P. *J. Controlled Release* **2001**, *75*, 307-315.
- (7) Siepmann, J.; Faisant, N.; Akiki, J.; Richard, J.; Benoit, J. P. *J. Controlled Release* **2004**, *96*, 123-134.
- (8) Berchane, N. S.; Carson, K. H.; Rice-Ficht, A. C.; Andrews, M. J. *Int. J. Pharm.* **2007**, *337*, 118-126.
- (9) Berchane, N. S.; Jebail, F. F.; Andrews, M. J. *Int. J. Pharm.* **2010**, *383*, 81-88.
- (10) Meyer, R. F.; Crocker, J. C. *Phys. Rev. Lett.* **2009**, *102*, 194501.
- (11) Meyer, R. F.; Rogers, W. B.; McClendon, M. T.; Crocker, J. C. *Langmuir* **2010**, *26*, 14479-14487.

(12) Wang, C.-K.; Wang, W.-Y.; Meyer, R. F.; Liang, Y.; Winey, K. I.; Siegel, S. J. *J. Biomed. Mater. Res. Part B Appl. Biomater.* **2010**, *93B*, 562-572.

Chapter 2: Literature Review

2.1 Marketed long acting release medications and their formulations

Development of long acting release (LAR) formulations of drug encapsulated in a matrix of polymer is a commercially viable formulation strategy, and several products of this type are approved for marketing in the United States. Gliadel Wafers[®] (polifeprosan 20 with carmustine implant) are used to treat individuals with high-grade malignant blastoma. The biodegradable discs are implanted directly into the brain during craniotomy, and have been shown to extend patient lives by delivering an extended dose of drug higher than what is tolerable when the drug is delivered systemically¹. Zoladex[®] (goserelin acetate implant) is used for treating patients with advanced cancers of the prostate. The 1 mm diameter biodegradable rod is implanted subcutaneously and releases a synthetic hormone for a 1 or 3 month period. Lupron Depot[®], Vivitrol[®], and Risperdal Consta[®] are all biodegradable microsphere based formulations. Lupron Depot[®] (leuprolide acetate for depot suspension), available in 1 to 4 month formulations, is indicated for men with prostate cancer, similar to Zoladex[®], and is also indicated for women with endometriosis or fibroids, and children with central precocious puberty. Vivitrol[®] (naltrexone for extended-release injectable suspension) is indicated for treatment of alcohol dependence, and is delivered as an intramuscular injection that is dosed every 4 weeks. Risperdal Consta[®] (risperidone) long acting injection, indicated for the treatment of bipolar I disorder as well as schizophrenia, is administered every 2 weeks as a deep intramuscular injection². Finally, NuvaRing[®] (etonogestrel /ethinyl estradiol vaginal ring) is a non-biodegradable contraceptive ring which releases two

hormones over a three week period, and is a popular alternative to daily contraceptive pills. All of these products have been shown clinically to improve patient outcomes relative to short acting daily doses of the same or similar medicines.

The LAR formulations currently available on the U.S. market come in a variety of shapes and sizes, and those specific products just described are formed into the shapes of rings, discs, rods and microspheres. The polymers used to formulate LAR products are just as varied. The non-biodegradable copolymer as ethylene-vinyl acetate (EVA) has been used successfully, and there are several biodegradable polymers in use either in research or on the market, such as polycaprolactone (PCL), poly(lactic acid) (PLA), poly(glycolic acid) (PGA), and copolymers such as poly[bis(*p*-carboxyphenoxy) propane-*co*-sebacic acid] (polifeprosan) and poly(DL-lactide-*co*-glycolide) (PLG)³. The biodegradable polymers are all polyesters, and degrade through hydrolytic cleavage of the ester bond, thus releasing the payload of drug.

Of the many polymers and geometries that could be studied for generating LAR formulations, we choose to focus on PLG based microspheres. The PLG copolymer certainly has been studied the most, and has enjoyed commercial success in a number of products, including Zoladex[®] rods, and Lupron Depot[®], Vivitrol[®], and Risperdal Consta[®] microspheres. A wide variety of types of PLG are available off the shelf. Specifically, the following traits can be altered so as to tune polymer hydrophilicity, crystallinity, degradation rate, and ultimately drug release rate. These traits are adjustable by varying the lactide to glycolide ratio (100:0 to 50:50), the polymer molecular weight (10 kDa to 140 kDa), and the polymer end group (acid or ester terminus). Microspheres are studied frequently as well, and methods for their manufacture are numerous. The particles can be

delivered via injection with a small needle, and including those listed above, at least 10 products have been commercialized for the U.S. market³.

2.2 Methods of manufacture for long acting release formulations

The most basic method for encapsulating drugs within PLG microspheres is known in the literature as the oil-in-water (o/w) emulsion solvent extraction method³. This method is depicted graphically in Figure 2.1. In the method, the continuous phase (CP) is prepared through mixing water with a surfactant, typically poly(vinyl alcohol). The dispersed phase is prepared by mixing the drug and polymer together with an organic solvent, typically dichloromethane. The dispersed phase is then emulsified within the continuous phase using any number of methods. The organic solvent is chosen such that it is sparingly soluble in water, and can thus be extracted slowly over time. As the solvent is extracted, the emulsion droplets shrink and solidify, ultimately yielding solid drug-loaded polymer microspheres. As a final step, the microspheres are washed to remove any residual surfactant, and either filtered and air dried, or lyophilized while contained within a suspending medium.

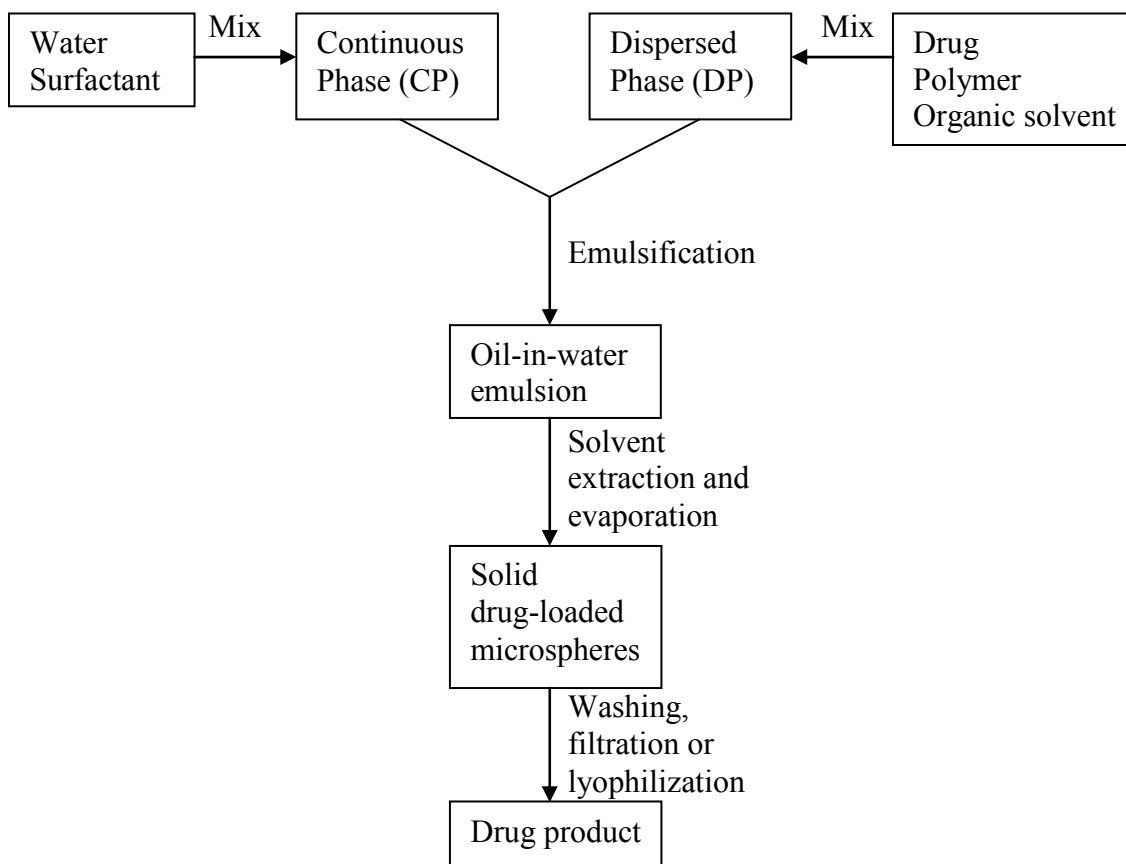


Figure 2.1 – Oil-in-water emulsion / solvent extraction method for producing drug-loaded polymer microspheres.

In order to generate drug-loaded polymer microspheres using the method described above, we need only pick the formulation and the emulsification method. The other steps can follow the common recipes available in the literature. Focusing first on the emulsification method, we seek a technique that is robust, scalable, continuous, and can generate sterile monodisperse particles over a wide size range.

2.3 Methods of manufacture for uniformly sized emulsions

There are many ways to make particles, and the general technique is to start with something big and make it small through application of force. When generating dispersions, high-shear emulsification and spraying processes are two common high-

throughput techniques that result in wide particle size distributions. The key to making uniform particles is to control the balance of forces between what holds particles together, and what tears them apart. For liquids, interfacial tension is the key force holding the liquid together, while a variety of forces can be used to tear a liquid apart. Here we will briefly review some of the major methodologies.

Dripping of a liquid by gravity from a household faucet is the most common example of how uniform droplets can be generated through the application of a force, and perhaps because of its common occurrence, the system has been studied in great detail. Harkins and Brown wrote a classic paper in 1919 that described the size of droplets produced from a dripping needle tip in relation to the diameter of the needle, the fluid density and the strength of the interfacial tension force⁴. The analysis is not as straightforward as one might initially assume, because the size of the drop that falls is always smaller than a simple force balance would predict. They then turned the analysis around, and proposed measuring the weight of a falling drop as a means of determining the interfacial tension of a fluid. This method remains popular today, but a sound theoretical analysis of the system was not developed until recently. In 1993, Eggers wrote a paper that described the nature of the hydrodynamic singularity which occurs when a droplet detaches from a needle tip.⁵ Then in 1994, Eggers and Dupont wrote a paper describing a one-dimensional "slender jet" approximation to the Navier-Stokes equation that could be applied to the case of the dripping faucet⁶. This development was important, because it enabled the use of computers to numerically simulate the dripping faucet geometry in a time-efficient manner. Finally, in 2005 Yildirim et al. published a paper called "Analysis of the Drop Weight Method", which utilized the equations of

Eggers and Dupont to perform a vast number of numerical simulations⁷. They were able to numerically simulate the original results of Harkins and Brown, and also rephrase as a dimensionless correlation the dimensionless drop size as a function of the ratio of gravitational and interfacial tension forces, ultimately showing that by understanding the balance of forces, we can predict the size of particles being made.

Gravity is a good force to use for generating droplets because it is widely available, but other forces such as electrostatic repulsion, mechanical motion, and fluid drag have the benefit of being adjustable, and thus the applied force can be tuned to break off a droplet of exactly the desired size. Electro-hydrodynamic atomization (EHDA) is an interesting application of this idea. In EHDA, a liquid is pumped through a needle tip, and an electric potential is applied between the needle and a counter-electrode. When the electrostatic force exceeds the surface tension force, a thin column of liquid jets from the needle tip, and the column subsequently breaks up into monodisperse drops⁸⁻⁹. The technique suffers from the drawback of painstakingly low flow rates (on the order of 100 $\mu\text{L/hr}$), a problem that can be addressed through multiplexing.¹⁰ Using this method, droplets in the size range of hundreds of nanometers up to around 10 μm have been made for purposes that include drug delivery¹¹⁻¹³.

A particularly exciting example of monodisperse droplet generation using mechanical vibration was described by Berkland et al.¹⁴ In their method, a column of liquid flows through a needle or other orifice so that the liquid jets. Using a piezoelectric transducer, a mechanical vibration is applied to the needle that precisely matches the most unstable wavelength predicted by Rayleigh's classic linear stability analysis¹⁵. This mechanical forcing causes the liquid column to break up into a uniform stream of

droplets, and droplet sizes in the range of 25 to 500 μm have been generated. The method has been used to generate drug-loaded PLG microspheres,¹⁶⁻¹⁷ and by mixing different monodisperse lots, they produced formulations that exhibit a constant release rate. Unfortunately, the method has been patented, and little work has been performed outside of the originating laboratory. Still, their pioneering work was early proof of the concept of engineered release profiles, and we seek to improve upon the efficiency and scalability of their technique.

Another example of monodisperse droplet generation through application of a controlled force was presented by Umbanhowar, Prasad and Weitz.¹⁸ In that work, monodisperse droplets were produced by immersing a bent needle into a fluid vessel undergoing solid body rotation, thus generating a co-flowing liquid stream at the needle tip. The size of the droplets is determined by the balance of drag and interfacial forces, and a model to predict droplet diameter based on this force balance was presented. Droplet diameters between 2 and 200 μm were generated. Subsequent studies in the same laboratory resulted in a related technique, where a circular needle was centered within an outer square tube, and monodisperse emulsions were generated.¹⁹ An even more unique geometry was presented by this laboratory, where a third collection tube was centered downstream from the circular injection needle and the square outer tube. Using this geometry, they were able to generate monodisperse double emulsions, including core-shell microcapsules with tunable wall thickness.²⁰ This technique, commonly called flow focusing, has enjoyed significant popularity and has been the subject of numerous investigations.

2.4 Review of cross-flow membrane emulsification

Instead of making particles by applying drag from a co-flowing liquid stream, a cross-flowing liquid stream can be used. When instead of a capillary, a microporous membrane is used, the technique is called cross-flow membrane emulsification (XME). When comparing all of the techniques for generating monodisperse particles, we find that XME meets our criteria, in that it is robust, scalable, continuous, and can generate sterile monodisperse particles over a wide size range. A diagram depicting the XME process is displayed in Figure 2.2.

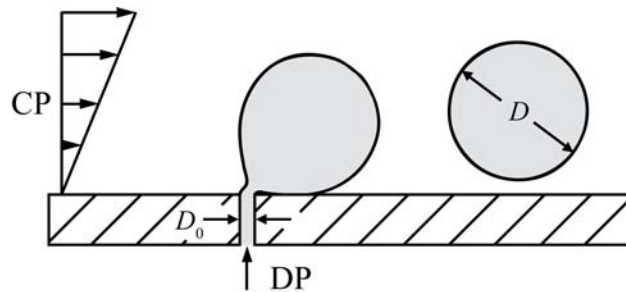


Figure 2.2 – Diagram of cross-flow membrane emulsification (XME).

In XME, the DP is forced by pressure through a membrane containing one or multiple small pores. Meanwhile, the CP flows tangentially over the membrane surface. Because the phases are immiscible, when the DP contacts the CP, a droplet grows at the membrane surface. As the droplet grows, the drag from the CP increases, until such point that the drag force exceeds the interfacial tension force. The droplet then detaches from the membrane surface, and the process repeats. When the flow rates from the two phases are constant, the process reaches a steady state, and the droplet grows to a repeatable size over and over again, yielding a monodisperse emulsion. And by adjusting either the drag force or the interfacial tension force, different sizes of droplets can be produced.

Experiments described in later chapters show that droplet size is either independent or only a weak function of DP flow rate, a result that improves process robustness. If components are fabricated from materials such as stainless steel and fluoroelastomer, then they can be sterilized through autoclaving, and thus are suitable for sterile processing. Finally, the process is scalable, because membranes with multiple pores can be used such that the desired mass throughput is obtained. Thus, the method meets the requirements we set for selection.

Cross-flow membrane emulsification belongs to a more general class of membrane emulsification methods, and these methods are reviewed at the start of Chapters 4 and 5. Looking just at XME, researchers have used numerous techniques to generate the cross-flow shown in Figure 2.2, and a variety of methods have been used to manufacture the microporous membrane. Kosvintsev et al. adapted a cone and plate rheometer, well known to produce constant shear across the surface of the plate²¹. In that study, they used commercially available silicon nitride membranes etched onto a silicon substrate, which exhibit a beautiful uniform array of straight-through microchannels. Surprisingly, their study resulted in fairly polydisperse particles. Furthermore, they concluded that particles produced using the cone and plate geometry were no more uniform than those produced using a standard paddle stirrer. The same research group later went on to produce drug-loaded microparticles using this method, but drug release profiles were not significantly more uniform than those based on conventional emulsification techniques²²⁻²³.

Kobayashi et al. were one of the first research groups to use photolithography to generate silicon microporous membranes, and then use those membrane to generate

emulsions using XME.²⁴⁻²⁵ They were unique in that they generated both circular as well as oblong pores, and they concluded that oblong pores result in a more uniform size distribution, though this result has not been widely repeated by others, and circular pores are still the most common.

Although not purely XME due to the presence of centrifugal forces, an interesting example of membrane emulsification using a rotating laser drilled stainless steel membrane was demonstrated by Vladisavljevic and Williams.²⁶ Their study operated in batch mode, with the membrane tube spinning within an outer stationary fluid vessel, though a continuous set up was also described. They showed that the low shear rates throughout their setup made possible the generation of large, shear labile droplets. Ultimately, their method produced droplets from 80 to 260 μm with uniformity of 5 to 20%.

Perhaps the most popular XME technique involves the use of Shirasu Porous Glass (SPG) as the membrane. In this method, a DP is pumped through a (typically) cylindrical annulus made of microporous glass and into a cross-flowing CP.²⁷ This method has also been successfully used for generating drug-loaded polymer microparticles, and one group of researchers generated PLA microparticles using both the XME SPG technique, as well as via conventional high shear emulsification.²⁸⁻²⁹ They found that both particle size uniformity as well as drug encapsulation efficiency were better for the XME technique. Unfortunately, SPG membranes are fragile, and are not amenable to sterile processing, and thus are unsuitable for commercial applications.

Looking now at the physics of XME, because of the well defined geometry and fluid properties, the basic system is amenable to both classical force balance descriptions,

as well as numerical simulations. Abrahamse et al. published the earliest known computational fluid dynamics (CFD) simulation of the XME process, and we later followed their approach for our own modeling.³⁰ CFD is particularly useful for gaining insight into the details of the XME process, and Abrahamse et al. published results showing how the pressure drop over and velocity within the pore is time-dependent, and also how the CP penetrates into the pore near the point of droplet snap off.

A number of researchers have tried to apply force and/or torque balances to predict droplet size during XME. Peng and Williams were one of the first to apply theory to their experimental results.³¹ They used a single 46 μm glass capillary embedded in epoxy and mounted within a 10 mm x 40 mm stainless steel flow channel. Their theoretical method took into account drag, interfacial, buoyant and inertial forces, and though their graphical representation displayed good agreement between experiment and theory, they presented only 5 experimental data points of droplet size vs. CP flow velocity, with too little supporting information to draw an independent conclusion.

An excellent application of the force balance approach to modeling of droplet size as a function of process conditions was performed by Husny and Cooper-White.³² Their work focused on modeling of droplet formation in T-shaped microchannels, which are a microfluidic analog to XME. Unlike traditional XME, in the T-shaped microchannel geometry the "pore" spans the entire width of the CP channel, and thus the resultant droplets also span nearly the width of the channel. Despite these complications, they presented a sophisticated force balance, as well as copious data to support their predictions. Furthermore, the DP in their fluid system contained a dissolved polymer, poly(ethylene oxide), and they showed the effect of changes of polymer molecular weight

and viscosity ratio, and how under certain conditions satellite droplets resulting from the long fluid neck were produced along with the primary droplets.

2.5 Application of controlled emulsification for engineered drug release

Numerous examples have been presented demonstrating how drug-loaded microparticles can be generated from controlled emulsification techniques. We also refer the reader to three recent review papers that discuss emulsification techniques including those described above, as well as other information of relevance to those seeking to produce polymer based drug-loaded microparticles.^{3, 33-34}

Taking the design to the next level, and using monodisperse particles to engineer formulations with the desired release rate is a problem that has been studied by far fewer researchers. Two research groups have made substantial contributions, and both groups solved the time-dependent diffusion equation with molecular weight dependent diffusivity.³⁵⁻³⁷

$$\frac{\partial c}{\partial t} = \frac{1}{r^2} \frac{\partial}{\partial r} \left(D(M_w(t)) r^2 \frac{\partial c}{\partial r} \right) \quad (2.1)$$

In the equation, c is the drug concentration, r is the radial position within the microsphere, D is the drug diffusivity within the polymer matrix, M_w is polymer molecular weight, and t is time. The relationship of M_w with time is typically reported to be log linear, $\ln(M_w) = mt + b$, and that again is the case here. The Pack Laboratory at the University of Illinois went further, and measured the initial distribution of drug in the microspheres using confocal fluorescence microscopy, and then used those data as the model initial condition. Both research groups were able to validate their models for the

release of drug from monodisperse microspheres, and they also used polymer molecular weight and microsphere size as design parameters for engineering the desired release profile.

This concludes what is only a brief review of the hundreds of papers that we have looked to for ideas and inspiration during the generation of this research. Thus as we begin the chapters devoted to our own research, we end with a quotation often wrongly attributed to Isaac Newton, but still very appropriate for any researcher: "Bernard of Chartres used to compare us to dwarfs perched on the shoulders of giants. He pointed out that we see more and farther than our predecessors, not because we have keener vision or greater height, but because we are lifted up and borne aloft on their gigantic stature."³⁸

2.6 References

- (1) Ewend, M. G.; Brem, S.; Gilbert, M.; Goodkin, R.; Penar, P. L.; Varia, M.; Cush, S.; Carey, L. A. *Clinical Cancer Research* **2007**, *13*, 3637-3641.
- (2) Drug Information Online. www.drugs.com (September 10, 2010),
- (3) Wischke, C.; Schwendeman, S. P. *Int. J. Pharm.* **2008**, *364*, 298-327.
- (4) Harkins, W. D.; Brown, F. E. *Journal of the American Chemical Society* **1919**, *41*, 499-524.
- (5) Eggers, J. *Phys. Rev. Lett.* **1993**, *71*, 3458.
- (6) Eggers, J.; Dupont, T. F. *J. Fluid Mech.* **1994**, *262*, 205-221.
- (7) Yildirim, O. E.; Xu, Q.; Basaran, O. A. *Phys. Fluids* **2005**, *17*, 062107.
- (8) Grace, J. M.; Marijnissen, J. C. M. *J. Aerosol Sci.* **1994**, *25*, 1005-1019.
- (9) Hartman, R. P. A.; Brunner, D. J.; Camelot, D. M. A.; Marijnissen, J. C. M.; Scarlett, B. *J. Aerosol Sci.* **2000**, *31*, 65-95.
- (10) Deng, W.; Klemic, J. F.; Li, X.; Reed, M. A.; Gomez, A. *J. Aerosol Sci.* **2006**, *37*, 696-714.
- (11) Ijsebaert, J. C.; Geerse, K. B.; Marijnissen, J. C. M.; Lammers, J.-W. J.; Zanen, P. *J Appl Physiol* **2001**, *91*, 2735-2741.
- (12) Loscertales, I. G.; Barrero, A.; Guerrero, I.; Cortijo, R.; Marquez, M.; Ganan-Calvo, A. M. *Science* **2002**, *295*, 1695-1698.
- (13) Ding, L.; Lee, T.; Wang, C.-H. *J. Controlled Release* **2005**, *102*, 395-413.
- (14) Berkland, C.; Kim, K. K.; Pack, D. W. *J. Controlled Release* **2001**, *73*, 59-74.
- (15) Rayleigh, L. *P. R. Soc. London* **1879**, *29*, 71-97.

- (16) Berkland, C.; King, M.; Cox, A.; Kim, K.; Pack, D. W. *J. Controlled Release* **2002**, *82*, 137-147.
- (17) Berkland, C.; Kim, K.; Pack, D. W. *Pharm Res* **2003**, *20*, 1055-1062.
- (18) Umbanhowar, P. B.; Prasad, V.; Weitz, D. A. *Langmuir* **2000**, *16*, 347-351.
- (19) Utada, A. S.; Fernandez-Nieves, A.; Stone, H. A.; Weitz, D. A. *Phys. Rev. Lett.* **2007**, *99*, 094502.
- (20) Utada, A. S.; Lorenceau, E.; Link, D. R.; Kaplan, P. D.; Stone, H. A.; Weitz, D. A. *Science* **2005**, *308*, 537-541.
- (21) Kosvintsev, S. R.; Gasparini, G.; Holdich, R. G.; Cumming, I. W.; Stillwell, M. T. *Ind. Eng. Chem. Res.* **2005**, *44*, 9323-9330.
- (22) Gasparini, G.; Kosvintsev, S. R.; Stillwell, M. T.; Holdich, R. G. *Colloid Surface B* **2008**, *61*, 199-207.
- (23) Gasparini, G.; Holdich, R. G.; Kosvintsev, S. R. *Colloids and Surfaces B: Biointerfaces* **2010**, *75*, 557-564.
- (24) Kobayashi, I.; Nakajima, M.; Chun, K.; Kikuchi, Y.; Fujita, H. *AIChE J.* **2002**, *48*, 1639-1644.
- (25) Kobayashi, I.; Mukataka, S.; Nakajima, M. *Langmuir* **2005**, *21*, 7629-7632.
- (26) Vladislavljivic, G. T.; Williams, R. A. *J. Colloid Interf. Sci.* **2006**, *299*, 396-402.
- (27) Yuyama, H.; Watanabe, T.; Ma, G.-H.; Nagai, M.; Omi, S. *Colloids and Surfaces A: Physicochemical and Engineering Aspects* **2000**, *168*, 159-174.
- (28) Liu, R.; Huang, S. S.; Wan, Y. H.; Ma, G. H.; Su, Z. G. *Colloid Surface B* **2006**, *51*, 30-38.
- (29) Liu, R.; Ma, G.; Meng, F.-T.; Su, Z.-G. *J. Controlled Release* **2005**, *103*, 31-43.
- (30) Abrahamse, A. J.; Padt, A. v. d.; Boom, R. M.; Heij, W. B. C. d. *AIChE J.* **2001**, *47*, 1285-1291.
- (31) Peng, S. J.; Williams, R. A. *Chem. Eng. Res. Des.* **1998**, *76*, 894-901.
- (32) Husny, J.; Cooper-White, J. J. *J. Non-Newton. Fluid* **2006**, *137*, 121-136.
- (33) Freitas, S.; Merkle, H. P.; Gander, B. *J. Controlled Release* **2005**, *102*, 313-332.
- (34) Li, M.; Rouaud, O.; Poncelet, D. *Int. J. Pharm.* **2008**, *363*, 26-39.
- (35) Raman, C.; Berkland, C.; Kim, K.; Pack, D. W. *J. Controlled Release* **2005**, *103*, 149-158.
- (36) Berchane, N. S.; Carson, K. H.; Rice-Ficht, A. C.; Andrews, M. J. *Int. J. Pharm.* **2007**, *337*, 118-126.
- (37) Berchane, N. S.; Jebrail, F. F.; Andrews, M. J. *Int. J. Pharm.* **2010**, *383*, 81-88.
- (38) Salisbury, J. M., Daniel D., *The Metalogicon of John of Salisbury*. University of California Press: Berkeley, 1955.

Chapter 3: Materials, Methods, and Preliminary Results

3.1 Cross-Flow Membrane Emulsification

Membrane emulsification describes a wide variety of techniques whereby a dispersed phase (DP) is forced through an orifice in a membrane into an immiscible continuous phase (CP), thereby generating an emulsion. A subset of this wide field is cross-flow membrane emulsification (XME), where nascent drops are formed at the membrane pore while subjected to a transverse shear flow. This process is represented below in Figure 3.1. The drag force exerted by the CP increases as the drop grows larger, until such point that the interfacial tension force can no longer hold onto the drop, after which the drop detaches and the process begins anew. It is this balance of drag and interfacial tension forces which allows for precise control over the size of the droplets which are produced via XME.

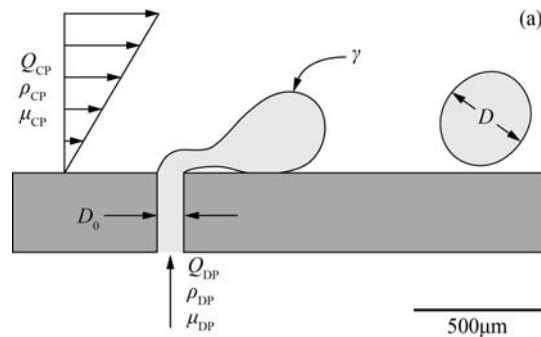


Figure 3.1 – Schematic of the XME process and important parameters.

This chapter is organized as follows. First we describe the method and apparatus for generating emulsions via XME, followed by the visual and data recording systems. Next we describe the preparation of simple and complex fluid pairs, and the measurement of relevant physical and particle properties. We describe the mathematics particular to

the fluid flow in our XME apparatus, and numerical simulations of those flows. Next, downstream processing techniques for generating solid microspheres from emulsions made via XME are described. Finally, we describe a model drug and an inline system for testing drug release from solid microspheres. Where appropriate, we have included preliminary results from the described techniques so as to validate the results and illustrate their utility.

3.1.1 Membrane Emulsifier

A system for producing emulsions via cross-flow membrane emulsification is shown in Figure 3.2 and Figure 3.3. Both CP and DP are pumped into their respective inlets from the bottom of the membrane holder. After changing direction, the CP flows along the membrane surface down a long rectangular channel 6.4 mm wide by 3.2 mm high. In some experiments, a solid insert is placed in the channel to decrease the height to 1.0 mm. In the center of the channel, DP passes through the membrane and into the cross-flowing CP, generating a droplet. The emulsion then travels down the remainder of the channel, and exits the membrane holder at the bottom, and finally proceeds to the collection vessel.

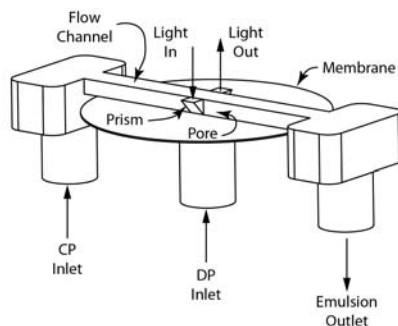


Figure 3.2 – Solid representation of membrane emulsifier flow channels, membrane and optical path.

The membrane holder is machined from two highly polished 4 in. square blocks of aluminum alloy 6061, between which the membrane is sandwiched. Two concentric rings contain double-seal Viton o-rings, thus sequestering the DP from the CP, and the CP from the ambient environment. The membrane holder top and bottom are connected via four ¼"-20 stainless steel screws. The 2 in. diameter membrane rests on the inner o-ring during assembly, and is machined such that the o-ring is compressed appropriately and there is no lip between the membrane and the membrane holder. The two 0.063 in. radius indentations in the membrane holder top are machined to hold two 1/8 in. right angle prisms mounted flush with the fluid channel wall, and a solvent proof optical epoxy holds the prisms in place. A 1 in. diameter sapphire window rests on top of the channel and prisms, and this assembly allows the emulsification process to be viewed from both the top and the side.

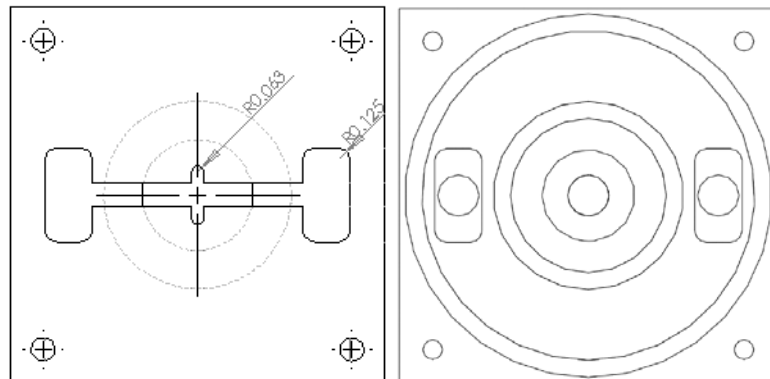


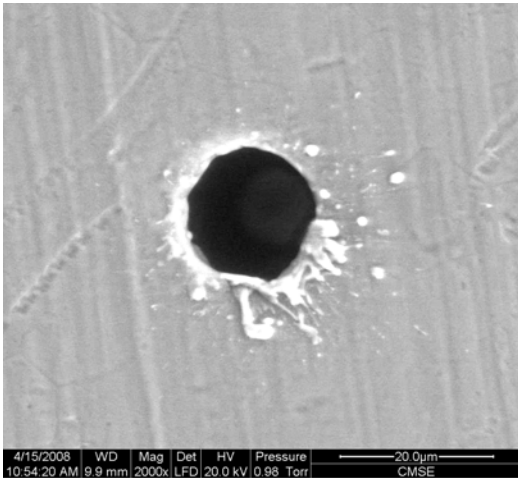
Figure 3.3 – Bottom view of membrane holder top (left), and top view of membrane holder bottom (right).

Disk-shaped membranes are constructed of stainless steel and cut to 50 mm in diameter from 0.30 mm thick sheet stock. For each membrane, a single pore is cut into the center of the membrane using one of three methods: laser drilling (Oxford Lasers, Shirley, MA), mechanical drilling (Roland Research Devices, Trenton, NJ), or electrical

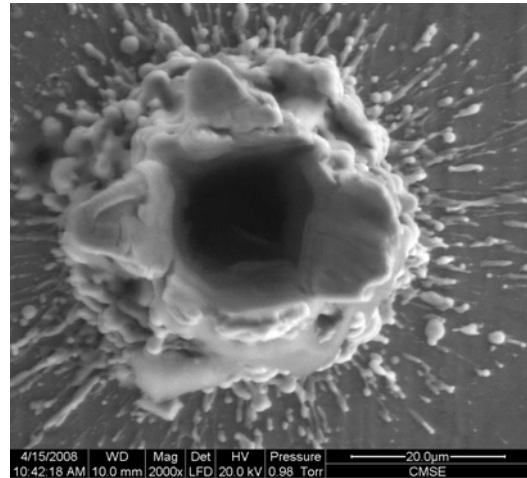
discharge machining (EDM) (Makino / Hummingbird Precision Machine Co., Lacey, WA). The pore dimensions for the various membranes are shown in Table 3.1, as measured via image analysis by fitting an ellipse to the pore perimeter. Electron micrographs showing the different membrane pores are provided in Figure 3.4 and Figure 3.5.

Table 3.1 – Summary of pore dimensions of membranes used for XME.

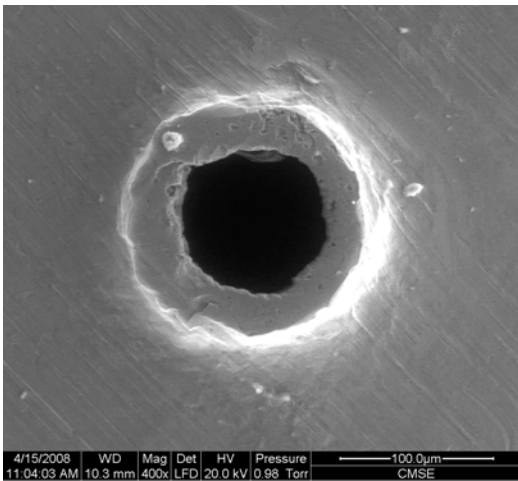
No.	Side	Method of Manufacture	Major Dia. (μm)	Minor Dia. (μm)	Average Dia. (μm)	Area (μm^2)	Perimeter (μm)
1	Front	Laser drilled	17	17	17	226	53
1	Back	Laser drilled	12	11	11	101	36
2	Back	Laser drilled	20	20	20	308	62
3	Front	Mech. drilled	94	93	94	6904	295
3	Back	Mech. drilled	174	171	173	23425	543
4	Front	EDM	24	24	24	451	75
5	Front	EDM	43	43	43	1464	136
6	Front	EDM	64	64	64	3213	201
7	Front	EDM	79	79	79	4868	247
8	Front	EDM	101	100	101	7959	316



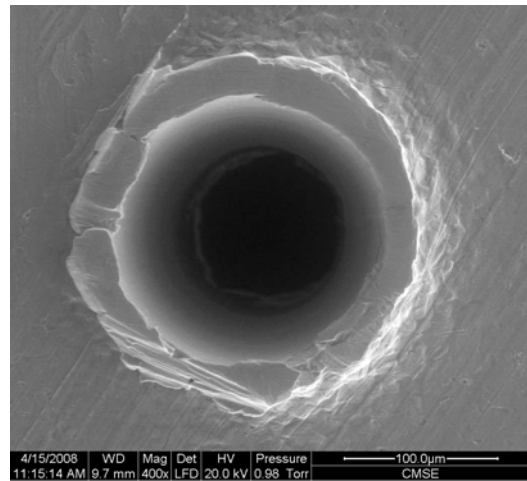
(a) Membrane 1 front side



(b) Membrane 1 back side

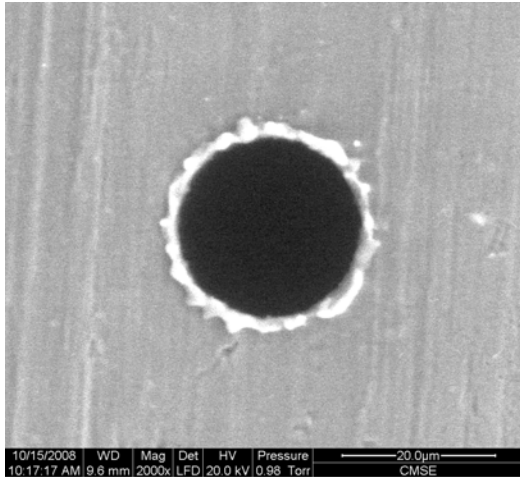


(c) Membrane 3 front side

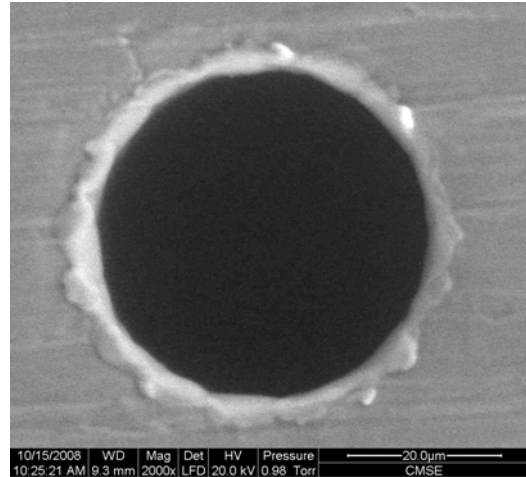


(d) Membrane 3 back side

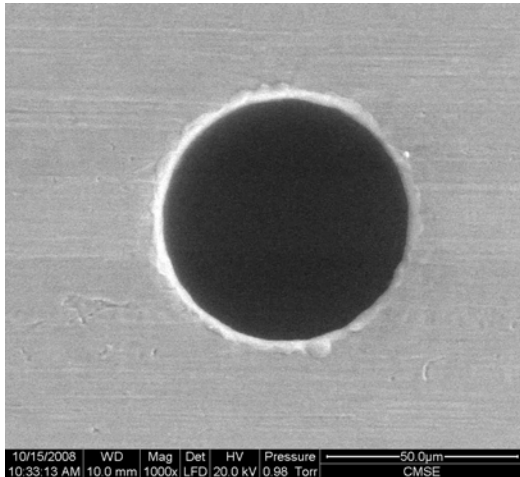
Figure 3.4 – SEM images of laser and mechanically drilled membranes.



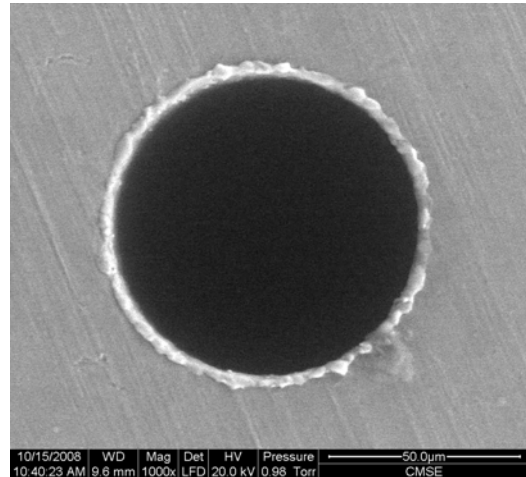
(a) Membrane 4 front side



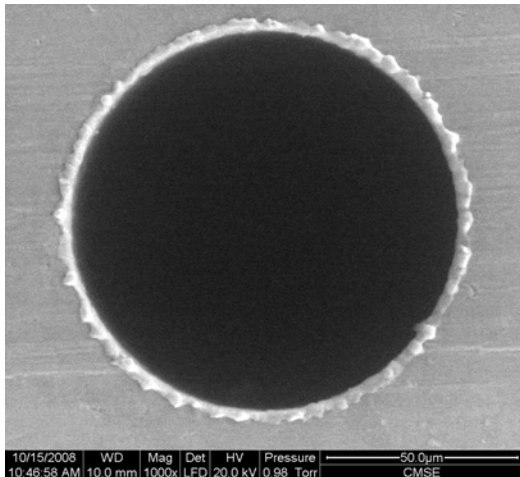
(b) Membrane 5 front side



(c) Membrane 6 front side



(d) Membrane 7 front side



(e) Membrane 8 front side

*All images courtesy of Leon Farber,
Merck Center for Materials Science and
Engineering

Figure 3.5 – SEM images of electrical discharge machined
membranes.

Figure 3.6 shows a process flow diagram containing the membrane emulsifier. The dispersed phase (DP) fluid is added to a 20 mL or 50 mL stainless steel syringe. The syringe plunger is driven by a KDS100 syringe pump (KD Scientific, Boston, MA) with a maximum linear driving force of 88 N. The desired flow rate is manually entered on the pump's digital display. The fluid is pumped through 1/8 in. outer diameter Teflon tubing until it couples to a tee at the entrance to the membrane emulsifier. A pressure transducer (SPT4V, Invensys, Milpitas, CA) is used to measure the DP static pressure at the same location.

The continuous phase (CP) is added to a 4 L stainless steel pressure vessel. The vessel is driven by a pressurized air source which is regulated between 0 and 100 psig. Upon applying pressure to the vessel, CP fluid is forced through a ball valve, woven filter and needle valve, all constructed of stainless steel. The ball valve is used to shut off the flow absolutely, while the needle valve is used in combination with the pressure regulator to set the desired flow rate. An inline flowmeter (FMTE4, DEA Engineering, Anza, CA) senses the flow rate, and this reading is recorded at a frequency of 1 Hz by the data acquisition system (OMB DAQ 56, Omega Engineering, Stamford, CT). The CP travels through 1/4" outer diameter stainless steel tubing until it reaches a tee where the static pressure is measured as the fluid enters the membrane emulsifier.

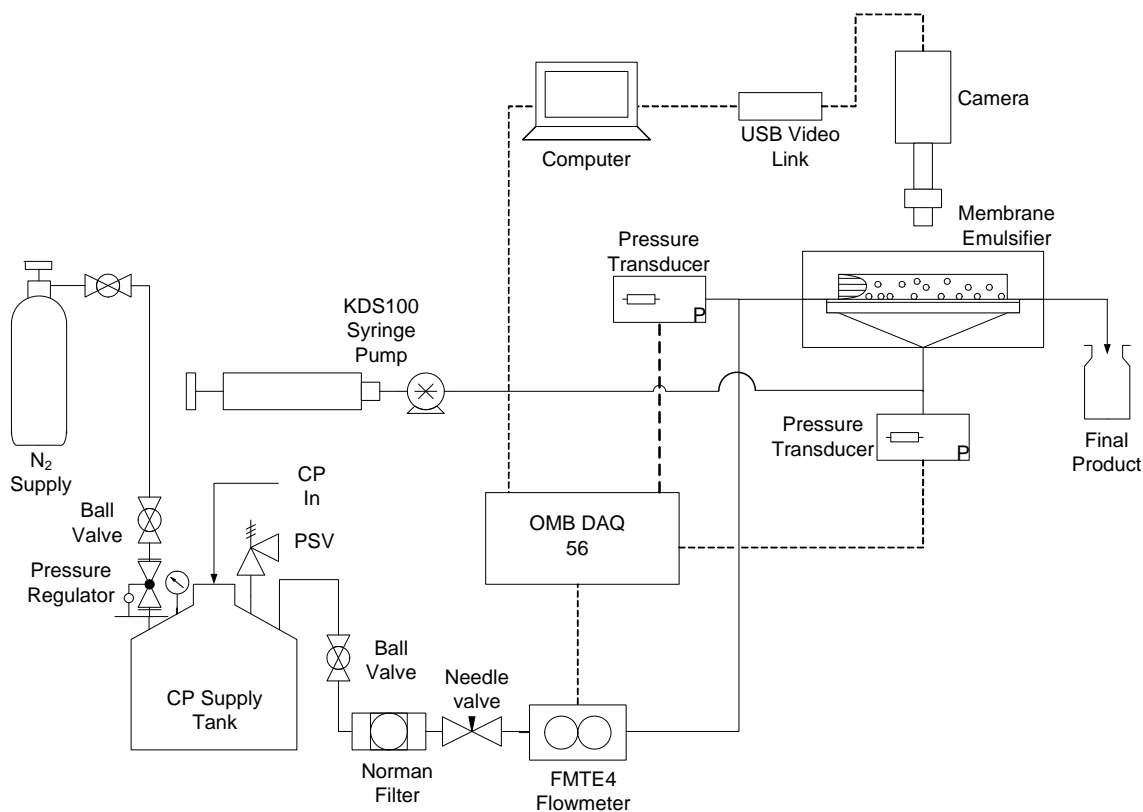


Figure 3.6 – Process flow diagram for XME.

3.1.2 Microscope and optics

A diagram of the microscope system used during membrane emulsification experiments is shown in Figure 3.7. A standard C-mount 640 x 480 resolution 8-bit COHU 4915 CCD camera is used to collect video images at a rate of 30 interlaced frames per second. The camera is mounted on an XYZ linear translation stage, providing two inches of travel in each direction. Light is focused on the camera's detector by a set of one inch diameter achromat lenses. The upper lens with a focal length of 150mm is fixed in place at the end of a six inch lens tube. The lower lens is interchangeable, and lens with focal lengths of 35 mm, 50 mm, 75 mm, 150 mm, or 300 mm were used throughout the study, thus providing magnification levels of 4.3x, 3x, 2x, 1x, or 0.5x.

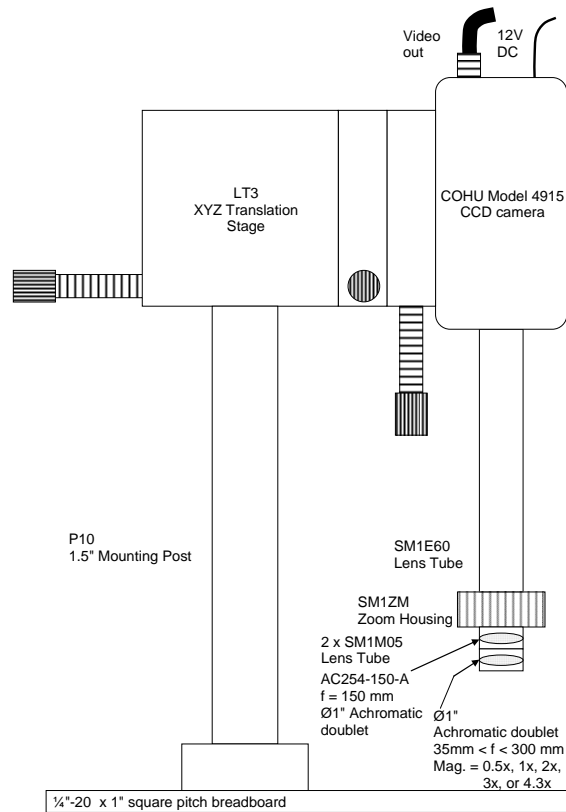


Figure 3.7 – Diagram of microscope system used during membrane emulsification experiments.

3.1.3 Computer and Data Acquisition System

Analog video from the COHU camera is digitized through a USB video link connector. Video images are collected using Video Toolbox (version 1.65, Zarbeco, Randolph, NJ), processed using VirtualDub (version 1.6.19, virtualdub.org), and analyzed using ImageJ (version 1.38x, rsb.info.nih.gov) and Matlab (R2007a, The Mathworks, Natick, MA). The Video Toolbox software timestamps each image with the date and time, using the system clock as the time source. Video exists as a sequence of uncompressed TIFF gray-scale images. All files are recorded to the system hard drive with the file name "date_fluid-system_magnification_file-number.avi".

The image length scale for each lens set is calibrated by imaging a standard micrometer slide or standard ruler in several different orientations and locations. Using ImageJ, a line is placed on the image of the slide perpendicular to the hash marks, then a line intensity profile is generated, thus generating a graph with peaks corresponding to the center of each hash mark. The average distance in pixels is then compared to the actual distance in microns, and thus the calibration ratio is determined.

Table 3.2 – Scale calibration factors for lenses used to view XME.

Mag.	Focal Length (mm)	Line Length (μm)	Line Length (pixels)	Scale Ratio ($\mu\text{m}/\text{pixel}$)	FOV x (mm)	FOV y (mm)
0.5	300	1000	87	11.494	7.4	5.4
1	150	3000	439	6.834	4.4	3.2
2	75	1000	275	3.636	2.3	1.7
3	50	1000	407	2.457	1.6	1.1

*FOV = Field Of View

The OMB-DAQ 56 data acquisition system collects data from various sensors, then digitizes and imports the data into Microsoft Excel. The program is set up to collect one datum point each second from the CP and DP pressure transducers, the CP flow meter, and the ambient and process temperature sensors. Calibration parameters are shown in Table 3.3.

Table 3.3 – Sensor calibration values.

System / Parameter	Value	Units
DP Pressure		
Scale	7.5	psig/V
Offset	-7.5	psig
CP Flow		
Scale	1.173	mL/min/Hz
Resolution	5	ms
Edge	rising	
CP Pressure		
Scale	1.673	psig/V
Offset	-1.673	psig

3.2 Continuous Phase and Dispersed Phase Fluid Preparation

3.2.1 Simple Systems

In some work, simple binary systems are used for the CP and DP. Typically, deionized (DI) water is used as the CP (18 M Ω /cm, Easypure Barnstead), and a variety of fluids are used for the DP. Some examples are n-butanol, n-pentanol, n-hexanol, n-decanol, dichloromethane, ethyl acetate, and their mixtures. All chemicals are obtained through Fisher Scientific (Fairlawn, NJ) or Sigma (St. Louis, MO). Each phase is saturated with the opposite phase and allowed to equilibrate overnight, so as to minimize mass transfer during emulsification.

3.2.2 Complex Systems

When generating drug-loaded polymer microspheres, the DP consists of the solvent dichloromethane (DCM), the biodegradable polymer poly(D,L-lactide-co-glycolide) (PLG), and haloperidol as a model drug. DCM was obtained from Fisher Scientific (Fairlawn, NJ). PLG (50:50 D,L-lactide/glycolide, ester terminated, inherent viscosity = 0.82 dL/g in HFIP) was obtained from Birmingham Polymers (Pelham, AL). Haloperidol was obtained from Sigma (St. Louis, MO). The CP consists of the surfactant

poly(vinyl alcohol) (PVA) dissolved in DI water. PVA (22 kDa, 88% hydrolyzed) was obtained from Acros Organics (New Jersey, USA).

For the production of polymer microspheres, CP is prepared by dissolving PVA in warm DI water at a concentration of 1% by weight. After dissolution of the PVA, the solution is filtered through a 14 μm cellulose acetate filter and allowed to cool to room temperature. DP is prepared by mixing haloperidol, PLG, and DCM in a closed container overnight. In most experiments, the DP contains 9% PLG and 1% haloperidol on a weight basis. In some experiments, the concentrations are raised to 11% PLG and 1.2% haloperidol, in order to raise the DP viscosity and increase resistance to droplet rupture.

3.3 Physical Property Measurements

3.3.1 Viscosity

Capillary viscometry is used exclusively for measurement of fluid shear viscosity. Viscometers with two different capillary diameters are used, type 0C and type 2 (Cannon Instrument Co., State College, PA). The viscosity is measured by drawing the fluid through the narrow capillary, then measuring the time required to pass between two timing lines. The viscosity μ is calculated as $\mu = k\rho t$, where k is provided by the viscometer manufacturer, and ρ is the mass density. In this case, $k = 0.002665 \text{ mm}^2/\text{s}^2$ or $0.09849 \text{ mm}^2/\text{s}^2$ for the type 0C and type 2 viscometers, respectively. The ambient temperature is recorded but not actively controlled. Typically, experiments are run in triplicate, and the average value is reported.

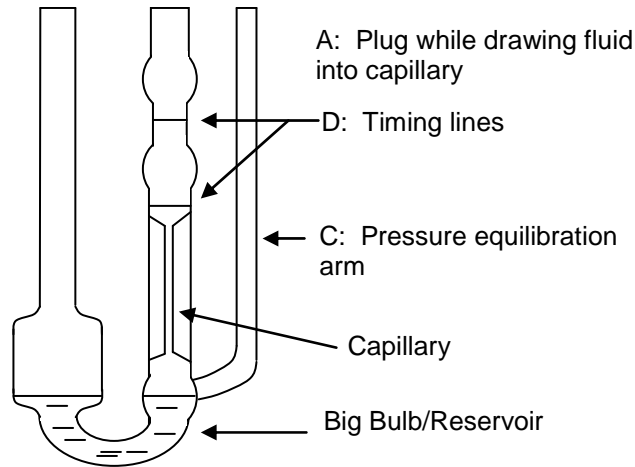


Figure 3.8 – Ubbelohde viscometer.

3.3.2 Density

The mass density of different fluids is measured by weighing the quantity of fluid required to fill a 50 mL volumetric flask to its fill line. The mass density ρ is calculated as $\rho = m/V$, where m and V are the mass and volume, respectively. Experiments are typically run in duplicate, and the average value is reported.

3.3.3 Interfacial Tension

The interfacial tension between the CP and DP fluid phases is measured using two different methods, namely, pendant drop profile analysis (PDPA) and the drop weight method. Each method, however, uses the same instrument set up, which is shown in Figure 3.9.

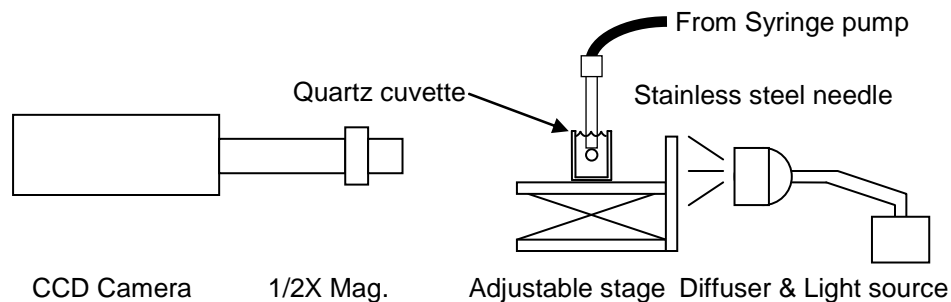


Figure 3.9 – Instrument set up used for interfacial tension measurements.

3.3.4 Pendant Drop Profile Analysis

Before beginning, the phases are equilibrated in contact with each other. As shown in Figure 3.9, a syringe pump is used to drip the DP into the CP at a controlled rate, generally from a needle tip. However, droplets can also be formed through a membrane pore, and the analysis works equally well. Videos of the dripping are recorded. Image processing starts from high contrast images of attached droplets, thresholding and converting the image from 8-bit to binary, then finding the edge coordinates as well as the drop apex in the image matrix. A coordinate transformation is then made to convert the drop apex to the zero position, and a scaling factor is added to give the coordinates proper SI units. Figure 3.10 shows this graphically.

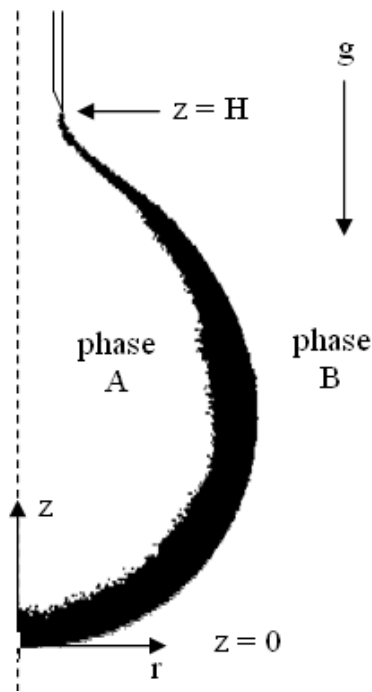


Figure 3.10 – Coordinate system for pendant drop profile analysis.

The edge coordinate array is then fit to the axisymmetric Laplace equation expressed in cylindrical coordinates¹,

$$\Delta p = \gamma \mathcal{N} \cdot \hat{n} \quad (3.1)$$

$$r = c(z) \quad (3.2)$$

$$p_H^B - p_H^A - (\rho^A - \rho^B)g(H - z) = \frac{\gamma}{c} \left[c \frac{d^2 c}{dz^2} - \left(\frac{dc}{dz} \right)^2 - 1 \right] \left[1 + \left(\frac{dc}{dz} \right)^2 \right]^{-3/2} \quad (3.3)$$

This expression can be non-dimensionalized to result in

$$-G + z^* = \frac{1}{c^*} \left[c^* \frac{d^2 c^*}{dz^{*2}} - \left(\frac{dc^*}{dz^*} \right)^2 - 1 \right] \left[1 + \left(\frac{dc^*}{dz^*} \right)^2 \right]^{-3/2} \quad (3.4)$$

with the dimensionless variables defined as

$$G \equiv [p_H^A - p_H^B + (\rho^A - \rho^B)gH] [\gamma(\rho^A - \rho^B)g]^{-1/2} \quad (3.5)$$

$$x^* = x \left[\frac{\gamma}{(\rho^A - \rho^B)g} \right]^{-1/2} \quad (3.6)$$

and the boundary conditions

$$z^* = 0 \Rightarrow c^* = 0 \quad (3.7)$$

$$z^* \rightarrow 0 \Rightarrow \frac{dc^*}{dz^*} \rightarrow \infty. \quad (3.8)$$

The Laplace equation expressed above has only two unknowns, γ and $\Delta p_H = p_H^B - p_H^A$, once the densities of each phase and the drop contour $r = c(z)$ are known. Using a non-linear least squares optimization routine, we solve for γ and Δp_H , then use these values to calculate G . This procedure is performed for each half of the drop, and the average of the two values is reported along with the sum of the squared errors. An example starting image and resultant drop are shown in Figure 3.11 and Figure 3.12.



Figure 3.11 – Drop of 1-pentanol in water attached to 90 µm pore.

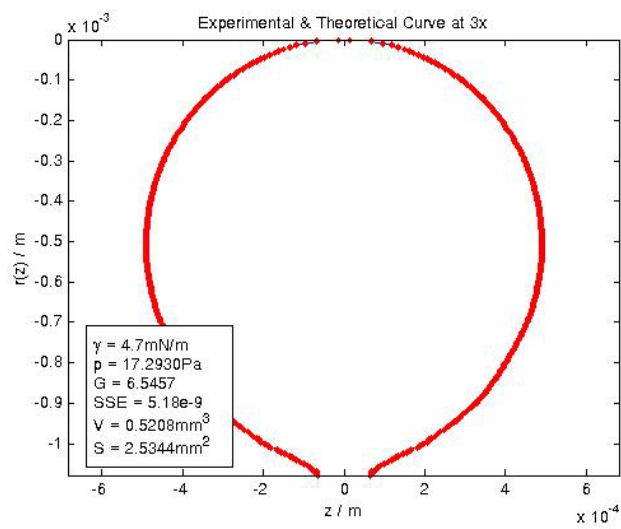


Figure 3.12 – Laplace equation fit (solid line) to 1-pentanol image edge coordinates (diamonds). The calculated interfacial tension $\gamma = 4.7$ mN/m is similar to the literature result² of $\gamma = 4.4$ mN/m \pm 0.2 mN/m. Also shown are the differential pressure inside and outside the drop at the apex, p , the sum of squared errors, SSE , the shape parameter, G , the drop volume, V , and the drop surface area, S .

Using the edge coordinate array, the volume of the drop, V , is calculated using the formula for a solid of revolution

$$V = \pi \int_0^H [c(z)]^2 dz \quad (3.9)$$

and the surface area, S , is calculated similarly using

$$S = 2\pi \int_0^H c(z) \sqrt{1 + \left(\frac{dc}{dz}\right)^2} dz. \quad (3.10)$$

Because movies are shot instead of individual images, it is possible to determine the reproducibility of interfacial tension measurements over time using an individual drop or multiple drops. Similarly, when surfactants are present in the system, the drop dynamic interfacial tension can be measured as additional surfactant is adsorbed to the interface. Because the PDPA technique assumes that the drop is static, low flow rates must be used if systemic errors are to be avoided. Figure 3.13 shows drop volumetric flow rate and interfacial expansion rate as a function of time for eight individual drops, with time zero defined as the point of drop snap off for the previous drop. Figure 3.14 shows average interfacial tension ($n = 11$) and relative standard deviation (RSD) across the same data set. As can be seen, the method is noisy for young drops, as measured by the RSD. This is due to the small deformations in young drops, which results in highly spherical drops, a consequence of the small ratio of gravitational to interfacial forces.

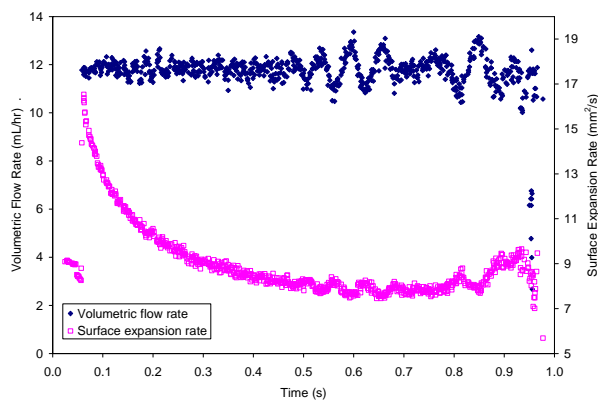


Figure 3.13 – Volume and surface expansion rates during PDPA.

These values are calculated for dispersed phase of a 9% solution of PLG in dichloromethane being pumped into a continuous phase of 1% poly(vinyl alcohol) in water. The flow rate set point is 11.0 mL/hr and the needle size is 460 μm .

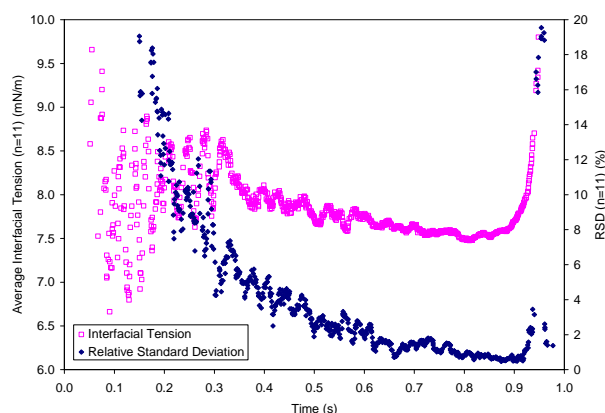


Figure 3.14 – Average interfacial tension ($n = 11$) (pink open squares) and associated relative standard deviation (blue closed diamonds) during PDPA. The values are calculated from a series of images of 9% PLG in dichloromethane being dripped into a continuous phase of 1% poly(vinyl alcohol) in water. The flow rate set point is 11.0 mL/hr and the needle size is 460 μm .

3.3.5 Drop Weight Method

Before beginning, the phases are equilibrated in contact with each other. As shown in Figure 3.9, a syringe pump is used to drip the DP into the CP at a controlled rate. Videos of the dripping are recorded. Droplet size is measured starting from high

contrast images of detached droplets, thresholding and converting the images to binary, then finding the edge coordinates, and numerically integrating the volume of the droplets by assuming axisymmetry.

The interfacial tension is determined using the Harkins and Brown methodology³.
⁴. A simple force balance predicts that the weight of a drop that falls from a needle tip is related to the interfacial tension according to

$$\pi D_0 \gamma = \Delta \rho g \frac{\pi}{6} D^3 \quad (3.11)$$

However, this expression only holds true in the limit of $D_0 \rightarrow 0$, due to non-linear effects that occur during droplet snap-off. For finite D_0 , it was shown by Harkins and Brown³ that an empirical correction factor could be found. Yildirim et al.⁴ refined this approach to a simple correlation

$$\text{Bo} = 3.60 \Phi^{2.81} \quad (3.12)$$

where the Bond number $\text{Bo} = \Delta \rho g D_0^2 / 4 \gamma$ and Φ is the dimensionless drop size $\Phi = 0.62 D_0 / D$. This expression can be further manipulated to yield

$$\gamma = 0.266 \Delta \rho g D_0^2 (D / D_0)^{2.81}. \quad (3.13)$$

Thus the interfacial tension γ between the two fluid phases can be calculated once the diameter D of the drop that falls is measured, assuming the density difference $\Delta \rho$ between the phases, gravitational acceleration g , and the needle diameter D_0 are known. Because the drops that fall are deformed due to gravity and hydrodynamic forces, the equivalent spherical diameter D is calculated from the volume V of the droplet according to

$$D = \left(\frac{6}{\pi} V \right)^{1/3}. \quad (3.14)$$

Generally speaking, the interfacial tension is a function of the time scale over which the measurement is performed. When using the drop weight method, we are interested in how the interfacial tension varies with the drop period Δt . The drop period is simply

$$\Delta t = \frac{\pi D^3}{6 Q_{DP}}. \quad (3.15)$$

The volumetric flow rate is calculated by measuring the drop volume and the time between drop detachments, and this flow rate is compared to the set point of the syringe pump in order to assure that the process is at steady state.

In order to measure interfacial tension using this method, the flow stream must be dripping and not jetting, thus implying $We \leq O(1)$, where $O(1)$ means a number on the order of 1. This occurs for

$$Q_{DP} \leq \left(\frac{\pi^2 \gamma D_0^3}{8 \rho_{DP}} \right)^{1/2}. \quad (3.16)$$

Setting $We = 1$ and then combining these relationships provides the appropriate scaling relationship for how droplet period changes with needle size:

$$\Delta t = 0.5 D_0^3 \left(\frac{\rho}{\gamma D_0^3} \right)^{0.5} \left(\frac{\gamma}{\Delta \rho g D_0^2} \right)^{1.07} \sim D_0^{-0.635}. \quad (3.17)$$

This implies that as the needle diameter grows larger, the droplet period decreases. But in order to maintain We constant, the volumetric flow rate must be increased quickly, with $Q_{DP} \sim D_0^{1.5}$. Figure 3.15 depicts these results.

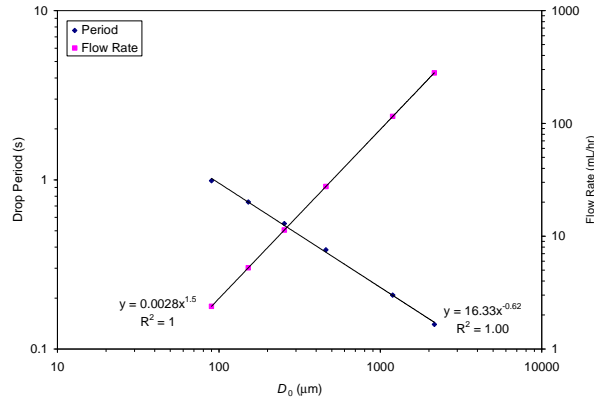


Figure 3.15 – Calculated drop period and corresponding flow rate to maintain $We = 0.1$. Calculations are for a fluid system with $\Delta\rho = 330 \text{ kg/m}^3$ and $\gamma = 8 \text{ mN/m}$.

3.3.6 Contact Angle Analysis

Contact angles of the various fluids against strips of stainless steel are measured by first cleaning the membranes via sonication in a 1% Alconox solution, then thoroughly rinsing and drying. The strips are then placed into a medium of one fluid, and the second fluid is dripped onto the surface of the strip. The process is recorded using the video microscope, and the contact lines are observed until equilibrium is reached. Subsequently the images are analyzed via the DropSnake ImageJ plugin⁵, which utilizes Laplace's equation to find the contact angle which results in the best fit of the drop contour. Depending on the preference for the outer phase (CP), either Method #1 or Method #2 is used, shown in Figure 3.16. Independent of which fluid is selected as the CP, the contact angles in these two methods should be related according to $\theta_{DP/SS} = 180^\circ - \theta_{CP/SS}$.

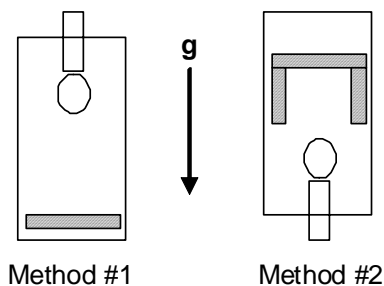


Figure 3.16 – Schematic of pendant or sessile drops during contact angle experiments. The drops are attached to needle tips prior to dripping onto a stainless steel substrate.

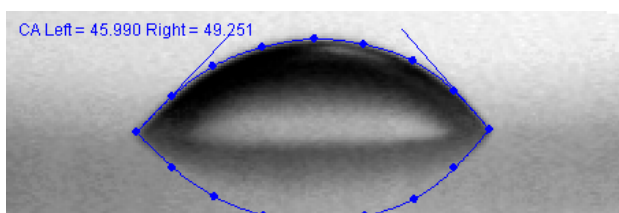


Figure 3.17 – Inverted image of water + 1% PVA on SS in a medium of DCM.

3.4 Preliminary Results from Physical Property Measurements

3.4.1 Interfacial tension measurements of normal alcohols

The interfacial tension of n-alcohols against water were measured by Villers and Platten² as a function of temperature using the Wilhelmy plate method, and these results are used for comparison to the PDPA results derived within this work. Figure 3.18 shows the reported values of Villers and Platten for different n-alcohols containing between 4 and 12 carbon atoms (solid line), as well as our results (diamonds). The data are comparable, with the largest difference being for decanol, where the difference is about 10%. This difference could be caused by system impurities or subtle temperature differences. Regardless, the differences across the range of compounds are small enough to conclude that the PDPA data are generally accurate.

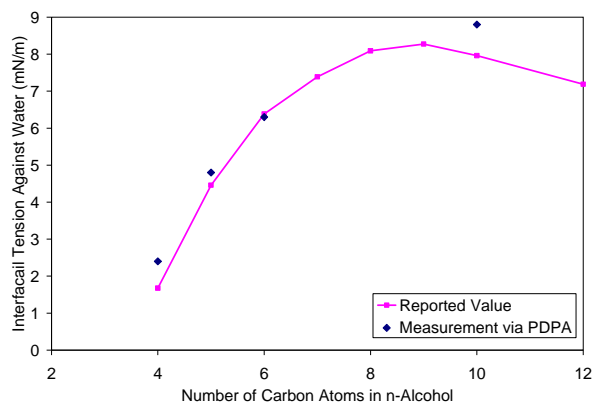
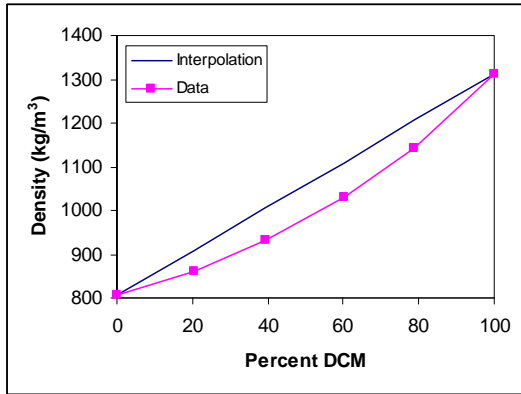


Figure 3.18 – Comparison of experimental and reported values of interfacial tension at 20°C.

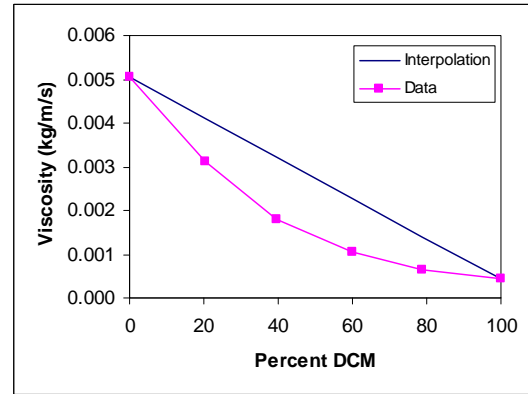
3.4.2 Physical properties of binary solutions of n-hexanol and dichloromethane

When examining the behavior of different fluids in the XME process, it is convenient to be able to tune physical properties through mixing two pure fluids. As a DP, n-hexanol and dichloromethane have disparate properties, and thus display drastically different dynamics during dripping-jetting transitions and droplet snap off in XME. Thus their mixtures are used to probe the transition between the different physical regimes. The physical properties of the mixtures as a function of weight percentage of DCM are shown in the four plots contained within Figure 3.19, with the solid lines generated by applying a weighted average to the values for the pure components. The density and viscosity of the mixtures show negative deviations from the interpolated predictions, which could be caused by a repulsive force between the two component molecules. The interfacial tension against water, measured via PDPA, also shows a negative deviation, and the trend also shows strange curvature. For this reason, replicate experiments were conducted, with the error bars indicating the standard deviation. The error bars show that the data are reproducible, and any error must be systematic in nature.

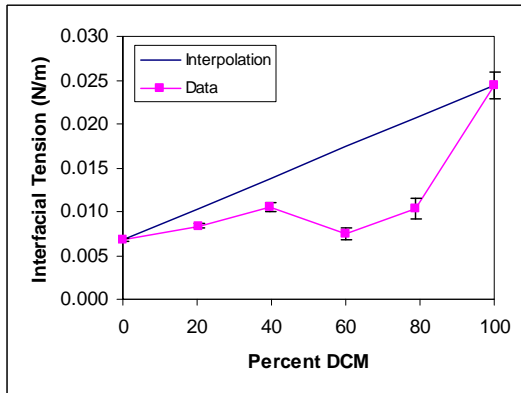
It is likely that some systematic error is introduced because the density of the solution is near that of water, and this reduces the accuracy of the PDPA technique. The fourth plot in Figure 3.19 shows the Ohnesorge number, $Oh = \mu/(\rho D_0 \gamma)^{1/2}$, with $D_0 = 90 \mu\text{m}$, as a function of concentration, and it can be seen that a wide range of Oh are accessible through the use of binary hexanol-DCM mixtures.



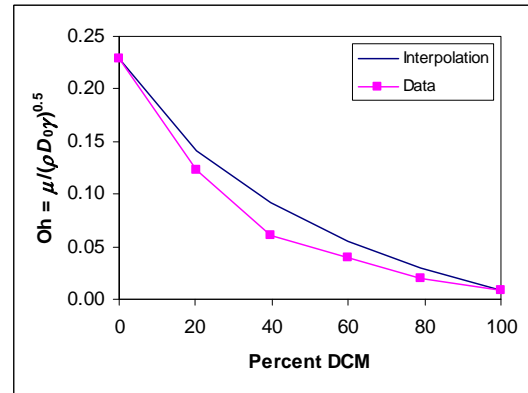
(a) Density of hexanol-DCM mixtures



(b) Viscosity of hexanol-DCM mixtures



(c) Interfacial tension of mixtures against water



(d) Oh_{DP} of mixtures with $D_0 = 90 \mu\text{m}$

Figure 3.19 – Physical properties of mixtures of n-hexanol and dichloromethane.

3.4.3 Viscosity of polymer solutions

When used as the dispersed phase in XME, the shear viscosity of the polymer solution has an appreciable impact on both the physics of droplet formation and break off, and also on the stability of droplets during downstream processing. For these

reasons, we measure the relationship between polymer concentration and shear viscosity for both a binary solution of PLG in DCM, and a PLG:haloperidol in DCM ternary system. Measurements are performed using capillary viscometry. Using the values obtained for the shear viscosity of both the pure solvent η_0 and the polymer solution η at a given polymer concentration c , we can calculate a number of other useful parameters that are widely used throughout the polymer literature. Table 3.4 gives the definitions of these terms.

Table 3.4 – Definitions of viscosity terms.

Parameter	Definition
Relative viscosity	$\eta_{rel} = \frac{\eta}{\eta_0}$
Reduced viscosity	$\eta_{red} = \frac{\eta_{rel} - 1}{c}$
Inherent viscosity	$\eta_{inh} = \frac{\ln(\eta_{rel})}{c}$
Intrinsic viscosity	$[\eta] = \lim_{c \rightarrow 0} \eta_{inh} = \lim_{c \rightarrow 0} \eta_{red}$

Utilizing these definitions, we calculate both the inherent viscosity η_{inh} and reduced viscosity η_{red} as a function of polymer concentration. At low concentrations, these relationships are both predicted to be linear. Figure 3.20 shows that this is indeed the case for the binary system. Both curves are predicted to intercept the y-axis at the intrinsic viscosity, $[\eta]$, which we measure to be 57.3 mL/g. The polymer overlap concentration, c^* , is approximately equal to the reciprocal of this value, $c^* \approx 1/[\eta] = 0.0175$ g/mL. The slope of the reduced viscosity curve is $[\eta]^2 k'$, where k' is called the Huggins' coefficient. For this system, $k' = 0.44$, and this value indicates that DCM is

neither a good solvent for PLG ($0.3 < k' < 0.4$) nor a theta solvent ($0.8 > k' > 0.5$), but rather is between these two extremes⁶.

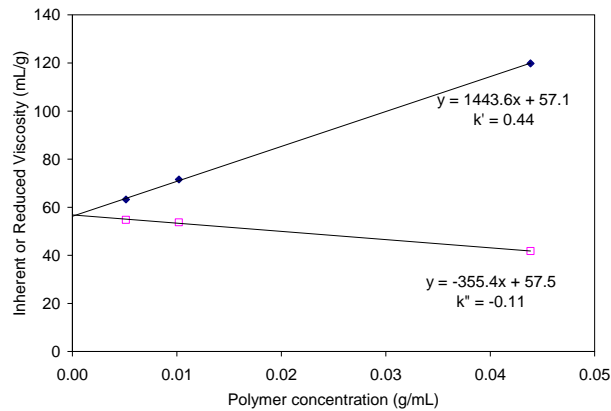


Figure 3.20 – Viscosity dependence on polymer concentration for PLG dissolved in DCM.

Above c^* , η_{red} is often observed to rise exponentially in accordance with the Martin equation

$$\eta_{red} = [\eta] \exp(kc[\eta]). \quad (3.18)$$

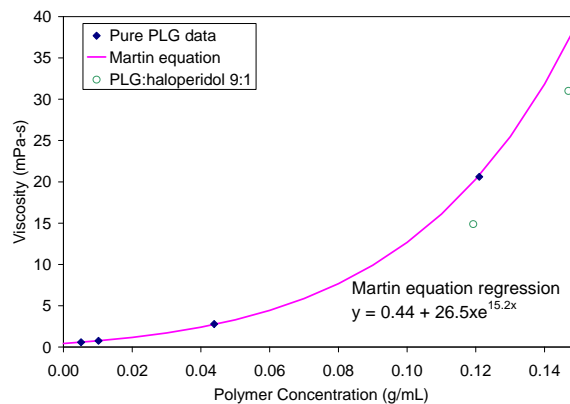


Figure 3.21 – Shear viscosity dependence on polymer concentration for PLG dissolved in DCM.

In Figure 3.21, we plot the shear viscosity as a function of polymer concentration, and fit the data to the Martin equation using a non-linear least squares regression. The

data fit well, despite the fact that only one fitting parameter is used. Also shown on the plot are viscosities of the PLG:haloperidol 9:1 ternary solution. The viscosities are similar, but systematically lower than the predictions for the binary system, most likely due to small temperature differences during the two experiments.

3.4.4 Zimm theory

In some experiments it is desirable to predict the polymer relaxation time λ while in solution. In particular, this prediction is relevant to the dynamics of droplet neck snap off, where polymer molecules are elongated due to the high elongational stresses in the flow. Zimm theory predicts that for dilute solutions, λ is related to the polymer and solution properties by

$$\lambda = \frac{6[\eta]\eta_0 M_w}{\pi^2 RT} \quad (3.19)$$

where M_w is the polymer molecular weight ($M_w = 137\,000$ g/mol for the PLG grade used here), and R and T are the gas constant and system temperature, respectively. At concentrations higher than the dilute limit, this relation is often used as an estimate of λ , with the solvent viscosity η_0 replaced by the solution viscosity η .⁷ The relaxation time in a standard 90% DCM, 9% PLG, and 1% haloperidol solution can then be estimated to be $\lambda = 3 \times 10^{-5}$ s. By doubling c , we predict an increase from $\eta = 15$ mPa-s to 240 mPa-s, which would result in $\lambda = 5 \times 10^{-4}$ s, a 17-fold increase. Similarly, by keeping concentration constant but instead doubling the molecular weight so that $M_w = 274\,000$ g/mol, we predict that $[\eta] = 90$ mL/g and $\eta = 73$ mPa-s. Coincidentally, this would also lead to $\lambda = 5 \times 10^{-4}$ s. During a typical XME experiment using this ternary system, the strain rate is found to be $\dot{\epsilon} = 2400$ s⁻¹, implying that the typical system will not exhibit

elastic effects, but that elastic effects should be found at higher M_w or c because $De = \dot{\epsilon} \lambda > 1$. These results are further discussed in Chapter 4.

3.5 Sizing of Microspheres

In most experiments, the droplets produced via XME are deformed from a sphere and into a prolate spheroid due to the shear stress imposed by the flowing CP. This complicates slightly the measurement of particle size. The diameter of a droplet is measured in two ways. In the simplified method, the major and minor diameters are measured manually in ImageJ from a video frame containing the droplet image. When higher resolution and/or larger sample sizes are needed, an automated image analysis routine in Matlab processes image sequences such that an ellipse can be fit to the droplet perimeter. This image analysis process is similar to what is used for interfacial tension measurements. Specifically, droplet images are converted to binary, thresholded, and the droplet edge coordinates are determined, from which the major and minor diameters and angle of rotation are determined. In all cases, the reported diameter is calculated as the average of the major and minor diameters. While an assumption that the particle takes the shape of a prolate spheroid with equivalent spherical diameter $D = (D_{\text{minor}}^2 D_{\text{major}})^{1/3}$ may be more appropriate for highly deformed particles, for the small deformations seen here the result is indistinguishable from this and other advanced diameter calculation techniques.

3.6 Downstream Processing of Drug and Polymer Loaded Emulsion Droplets

The classical oil-in-water emulsion-solvent evaporation method is used in preparation of solid microspheres⁸. After production of the emulsion droplets via XME,

they are collected in a large vessel and allowed to settle under gravity. Only gentle agitation is used so as to prevent shear break up of the particles. Over a period of many hours, DCM is slowly extracted into the CP, where it is sparingly soluble (solubility of 13 g/L in pure DI water at 20°C). The DCM is then readily evaporated from the collection vessel due to its low boiling point (vapor pressure of 47 kPa at 20°C), yielding solid drug-loaded polymer microspheres. These solid microspheres are then isolated from the suspending medium by filtration, and in the process are washed with pure DI water to eliminate residual PVA.

3.7 Computational Fluid Dynamics

Two software programs, Fluent 6.3 and Gambit, are used to perform Computational Fluid Dynamics (CFD) simulations of the membrane emulsifier CP flow and the emulsification process.

3.7.1 Continuous Phase Flow Simulations

Although the velocity profile for fully developed laminar flow in a rectangular channel can be found analytically, it is difficult to assess whether flow is fully developed when it passes the membrane pore. CFD simulations of the velocity in the entire CP flow channel as a function of the total flow rate Q_{CP} yield the results shown in Figure 3.22. In the simulations, $\rho = 1020 \text{ kg/m}^3$, $\mu = 0.0034 \text{ kg/m/s}$, and the simulation is set up using steady state, three dimensional, double precision, pressure-based Navier-Stokes equation in laminar flow. Boundary conditions are constant velocity at the inlet, and constant pressure at the outlet, with no slip at the chamber walls. As can be seen, flow profiles at the y - z plane $x = 0$ are fully developed and symmetric for $Q_{CP} = 10 \text{ mL/min}$ and $Q_{CP} =$

100 mL/min, whereas at $Q_{CP} = 1000$ mL/min the flow is no longer well behaved. Consequently, experiments are conducted such that $Q_{CP} < 300$ mL/min.

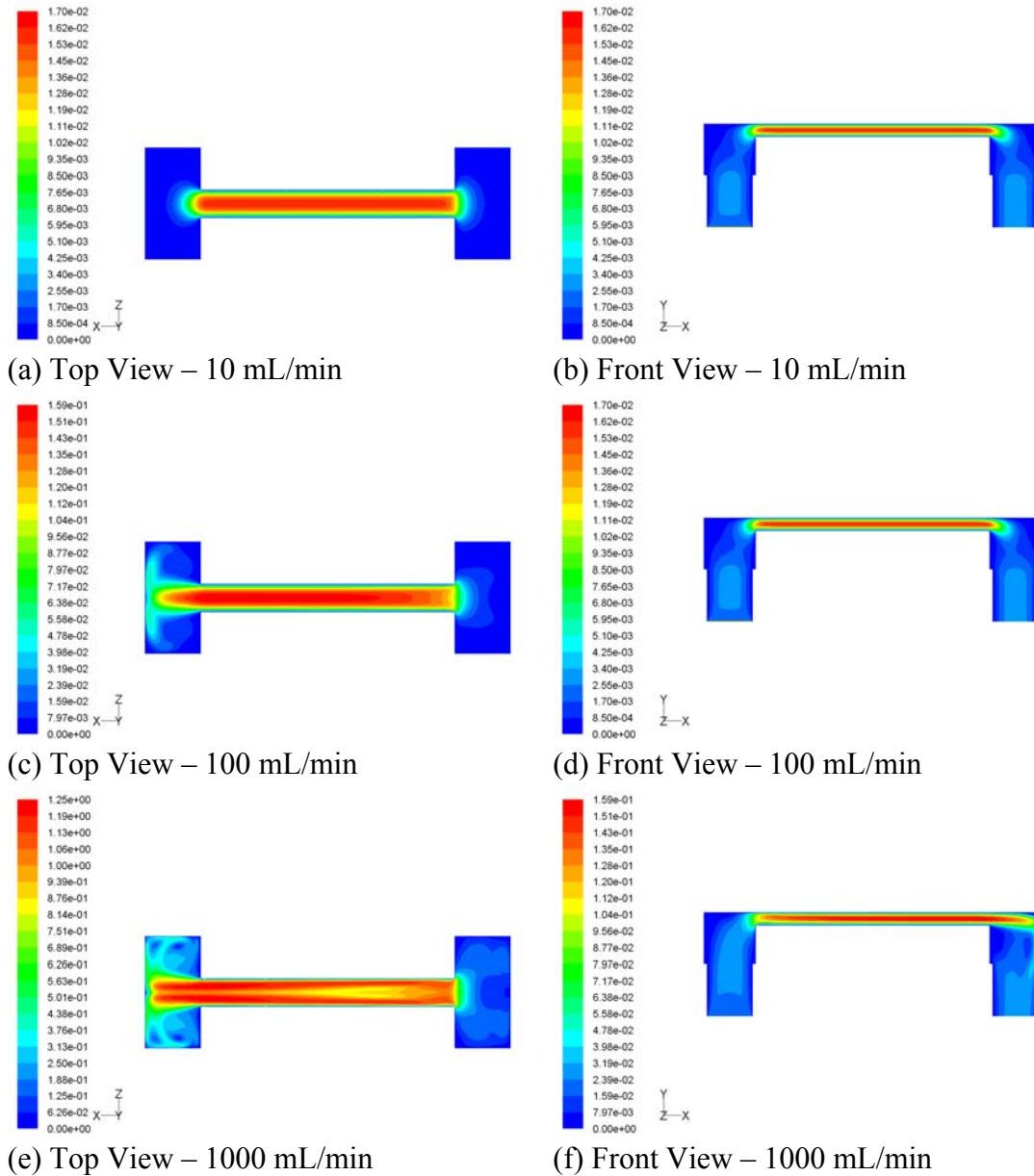


Figure 3.22 – Contours of velocity magnitude (m/s) calculated in Fluent 6.3. Flow is in +x-direction.

3.7.2 Cross-flow membrane emulsification simulations

Simulations of the cross-flow membrane emulsification process are performed to further validate experimental and theoretical results. In the simulations, the computational mesh is set up with the following properties:

- CP Zone (x by y by z) = 6.35 mm by 3.175 mm by 3.175 mm
- DP Zone (diameter by length in y) = 0.090 mm by 0.3048 mm
- Single x - y symmetry plane at pore midline $z = 0$
- Number of cells = 6×10^5

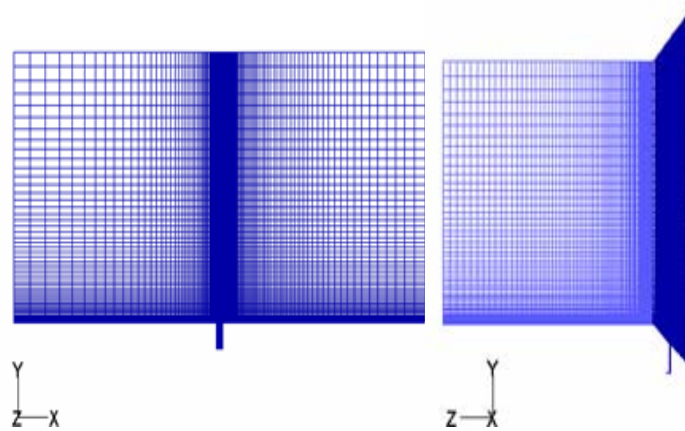


Figure 3.23 – Computational mesh used for CFD simulations of membrane emulsification.

Fluid properties used in the simulations are shown in Table 3.5. Through the simulations, the CP volumetric flow rate Q_{CP} is varied, while the DP flow rate Q_{DP} is held constant. Simulation boundary conditions are constant velocity at both inlets, constant pressure at the outlet, and a contact angle of 180° between the DP and the chamber walls.

Figure 3.24 shows typical results.

Table 3.5 – Physical properties of fluids in Fluent simulation.

Chamber Properties			DP Properties		CP Properties		CP/DP
D_0 (μm)	H (mm)	W (mm)	ρ (kg/m^3)	μ ($\text{kg}/\text{m}/\text{s}$)	ρ (kg/m^3)	μ ($\text{kg}/\text{m}/\text{s}$)	γ (kg/s^2)
90	3.18	6.35	1326.5	0.000437	1000	0.00125	0.0061

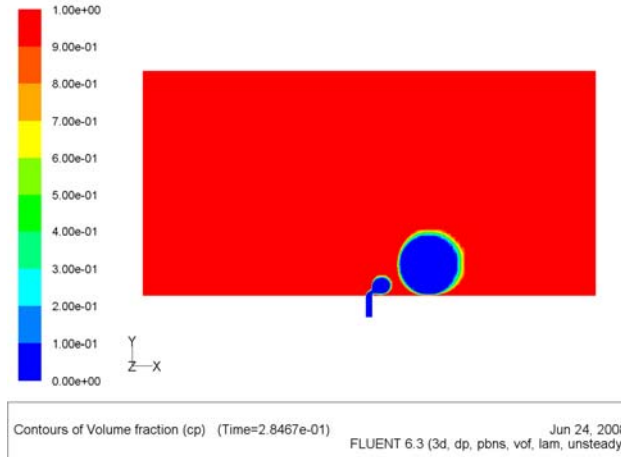


Figure 3.24 – Volume fraction contours shown at the symmetry plane during a cross-flow membrane emulsification simulation. In this simulation, $Q_{CP} = 50$ mL/min and $Q_{DP} = 5.1$ mL/hr.

3.7.3 Cross-flow membrane emulsification simulation results

Simulations are performed across the range $50 \text{ mL/min} < Q_{CP} < 400 \text{ mL/min}$, and all at $Q_{DP} = 5.1 \text{ mL/hr}$. In each case, the simulation is run until a droplet breaks off from the membrane pore. The image is then analyzed to determine the diameter of the droplet. The dimensionless droplet size D/D_0 is plotted against the capillary number,

$$Ca = \mu_{CP} \frac{dv}{dz} D_0 / \gamma. \quad (3.20)$$

A regression line fit to the data yields the form $D/D_0 = kCa^{-0.5}$, with $k = 0.42$.

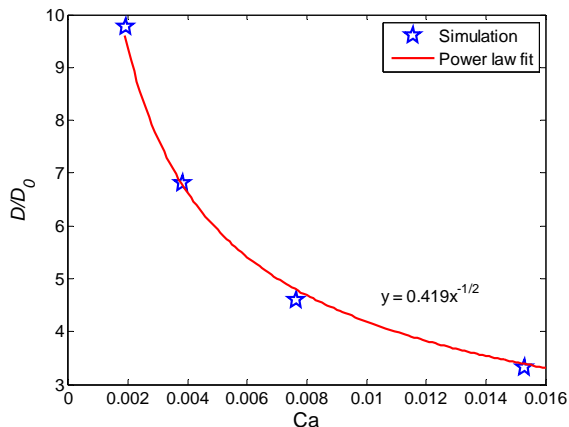


Figure 3.25 – Dimensionless droplet diameter vs. capillary number from Fluent simulations.

3.8 Model Drug Haloperidol

Haloperidol is a popular drug indicated for use in the management of psychotic disorders, as well as for the control of tics of Tourette's Disorder⁹. It is an excellent model drug for use in microencapsulation studies due to its low daily dose and high hydrophobicity¹⁰. Furthermore, because the drug has been studied since at least 1960¹¹, it has been the subject of numerous investigations¹²⁻¹⁷, and physical and chemical properties are widely available. For these reasons, haloperidol is used throughout the present studies.

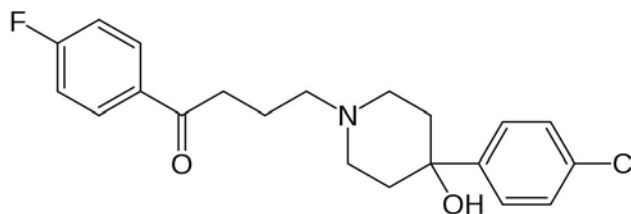


Figure 3.26 – Haloperidol molecular structure.

Table 3.6 – Physical and chemical properties of haloperidol.

Property	Value	Units
Molecular weight ¹¹	375.86	g/mol
Crystalline melting point (free base) ¹¹	148	°C
Water solubility at pH = 7.4 and room temperature ¹⁷	15	mg/L
Water solubility at pH = 6.0 and room temperature ¹⁷	201	mg/L
pK _a ¹⁷	8.25	
Peak UV absorbance ¹⁸	244	nm
Extinction coefficient at 244 nm ¹⁸	0.0341	L/mg/cm
Typical oral dose range (BID or TID) ⁹	0.5 – 5.0	mg
Elimination half-life ¹⁹	15.1 ± 2.5	hr
Relative bioavailability ¹⁹	0.64 ± 0.23	

3.9 In Vitro Drug Release Measurement System

A dual reactor and flow system coupled to a dual inline spectrophotometer are used to measure drug release from polymer particles over time. The two independent systems can be used to conduct two release studies simultaneously, or one can be used as a control or to continuously monitor background absorbance. These components are described below.

3.9.1 Drug release microenvironment

A Spectra/Por Float-a-lyzer G2 1 mL dialysis device with 100K MWCO cellulose ester membrane (Sigma-Aldrich, St. Louis, MO) is used to retain the particles in a static state without convection during drug release studies, which is similar to the physiological environment particles experience when injected subcutaneously or intramuscularly.⁸ The particles are added to the container along with buffer solution, and a screw on cap with o-ring positively seals the container. A flotation ring surrounds the outside of the device and thus maintains the device oriented upright at the fluid surface within the stirred tank.

3.9.2 Reactor and Flow System

Figure 3.27 shows a diagram of the system flow setup, which is designed as follows. A recirculating controlled temperature water bath sends warm water through two daisy-chained glass jacketed mixing tanks, thus keeping the vessels at the desired temperature set point, typically 37°C. The two mixing tanks are typically filled with 900 mL phosphate buffered saline solution, and sometimes a surfactant such as polysorbate 20, and an antimicrobial agent such as NaN₃. At the bottom of the tanks are magnetic stir bars, driven by the magnetic stir plates below. Three through holes are cut into the custom-made lid for each vessel. A long supply dip tube is located near the bottom of the vessel. From the supply dip tube, silicone silastic tubing leads to the bottom of the quartz flow cell so that any air entrained in the system can escape. The top of the flow cell is connected to Cole-Parmer Pharmed tubing, which is more resilient to continuous use. The tubing passes through the peristaltic pump, and then leads back to the return dip tube in the same mixing tank. One ¼ inch diameter type K immersible thermocouple is located in each tank and is connected to the data acquisition system to provide continuous temperature monitoring.

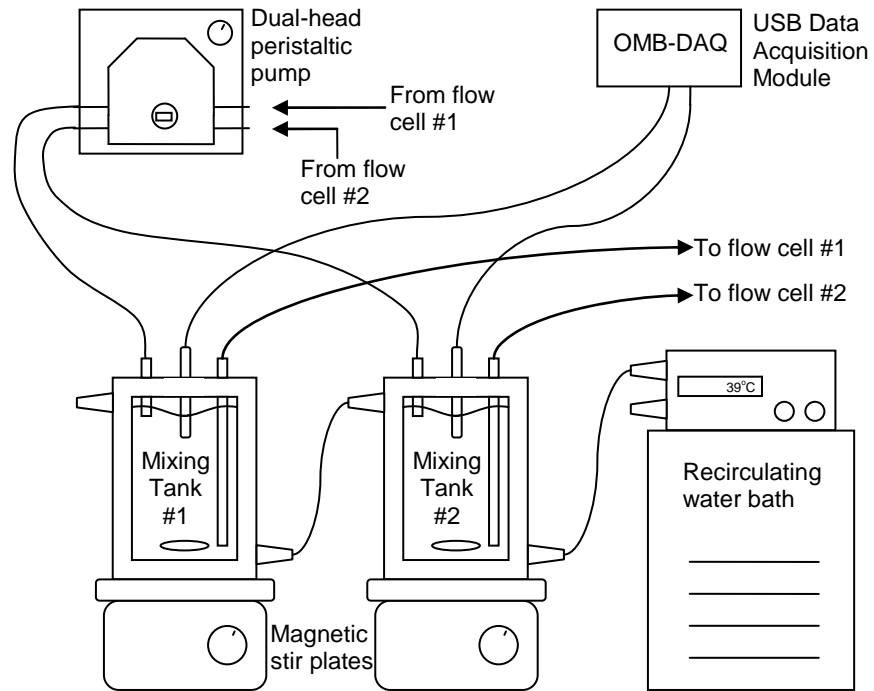


Figure 3.27 – Reactor and flow system used for drug release studies.

3.9.3 Dual-Channel Spectrophotometer

The dual-channel spectrophotometer shown in Figure 3.28 can be used to measure the UV absorbance at $\lambda = 250$ nm of any solution contained in a standard 1 cm cuvette. The wavelength of 250 nm is used because there is a maximum in haloperidol absorption near this value ($\lambda_{\text{max}} = 244$ nm). Other wavelengths can be selected by replacing the band-pass filter that follows the collimating lens.

The spectrophotometer is designed as follows. A function generator is used to set the frequency with which light is produced. Typically, a frequency of 1 pulse per second is used, and the monostable multivibrator 74HC123 chip is used to stretch the pulse to the desired width. See Figure 3.29 for the circuit design. The PX-2 UV (Ocean Optics, Dunedin, FL) light source produces a pulse of wide spectrum UV light when it detects the rising edge from a 0 to 5 V TTL signal from the peak-hold circuit. After being

transmitted through a fiber optic cable, the light is collimated and passed through a 250 nm band pass filter. A polka dot beam splitter (Thorlabs, Newton, NJ) divides the collimated light beam into two roughly equal beams 90° apart. Each collimated light beam passes through a quartz cuvette. Glass absorbs UV light and thus cannot be used. Any absorbing species reduces the amount of light that is transmitted through the cell. A 40 mm focal length lens contained within a 1 inch diameter lens tube focuses each light beam onto the 2.54 x 2.54 mm active area on the PDA25K photodiode (Thorlabs). The photodiode, set to a gain of 70dB, sends a 0 to 10 V signal to the LF398 chip on the peak-hold circuit. The signal output of the LF398 chip tracks the signal input from the photodiode as long as the logic input voltage to the chip is 5 V. When the logic input falls to 0 V, the logic gate closes and the capacitor on the chip holds the signal output at the voltage read when the falling edge was detected. The monostable multivibrator 74HC123 is used to set the square wave pulse to the desired width, such that the falling edge corresponds with the peak output from the photodiode. The OMB-DAQ USB data acquisition module reads the signal output voltage on the LF398 chip and records to a Microsoft Excel file. The signal output reads the peak of the photodiode signal except when the TTL signal is at 5 V. Because this only occurs for about 10 μs every second, this is a rare occurrence. The peak hold circuit shown in Figure 3.29 is used to collect the photodiode signal and transmit it to the data acquisition device.

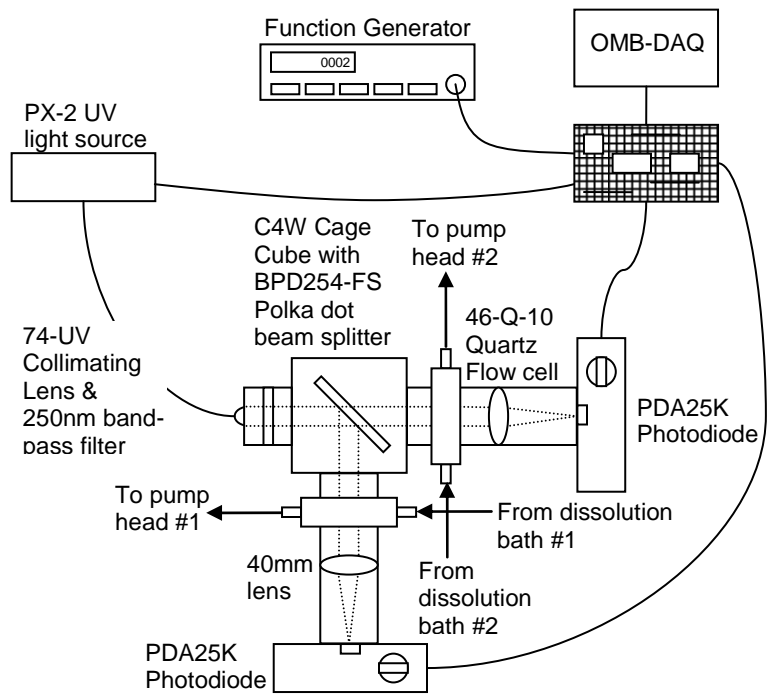


Figure 3.28 – Spectrophotometer optics and electronics configuration.

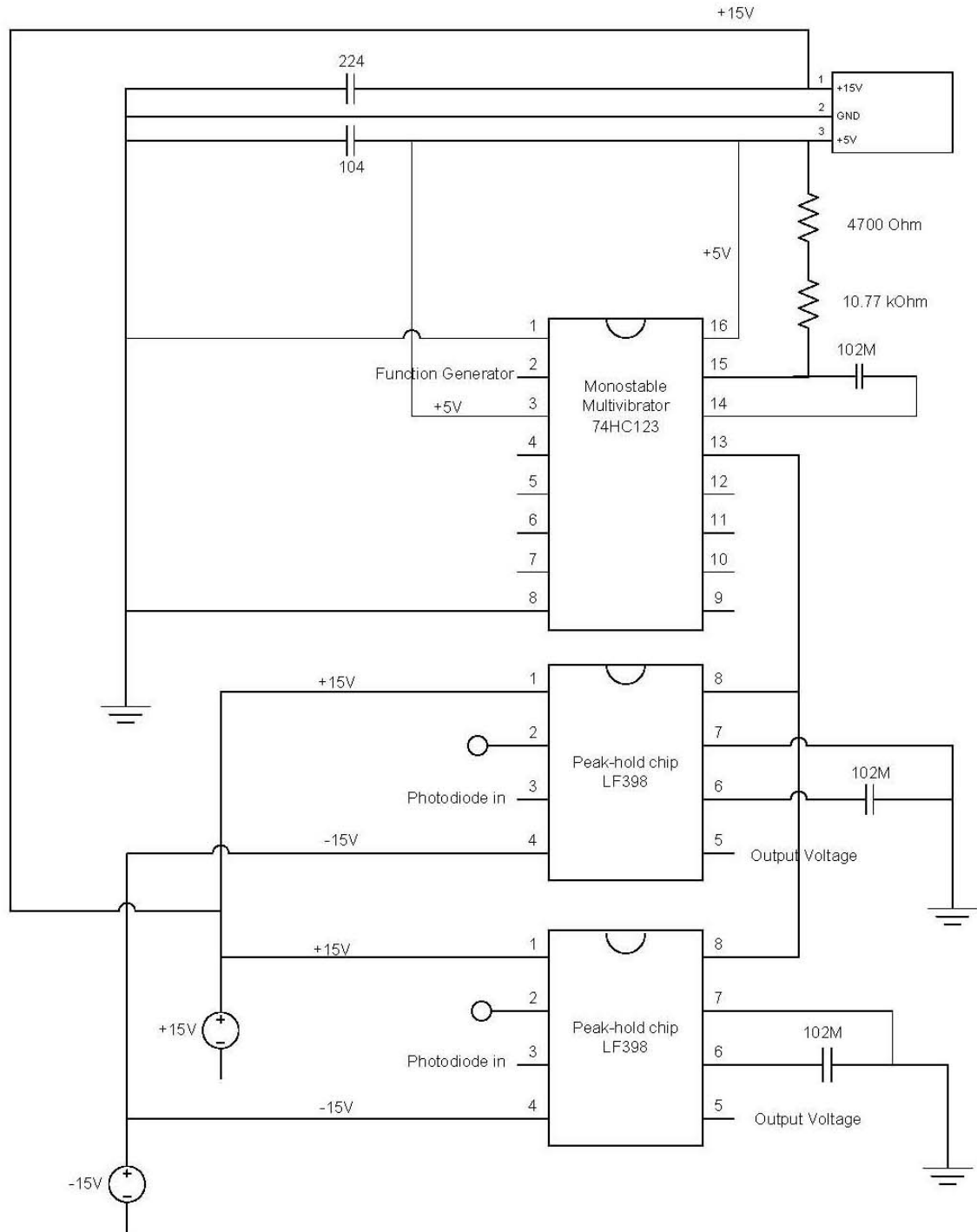


Figure 3.29 – Timing circuit and peak-hold circuit used within the spectrophotometer.

The photodiode gives readings in voltage, and the absorbance A is calculated using

$$A = \log\left(\frac{V_0}{V}\right) \quad (3.21)$$

where V is the reading of the sample, and V_0 is the reading of the cell with solvent (but no sample). Beer's Law states that

$$A = \varepsilon_i c_i L \quad (3.22)$$

where ε_i is the extinction coefficient of species i , c_i is the solute concentration, and L is the cell path length. Using these relationships, the concentration of dissolved species can be determined from the absorbance readings once the absorption coefficient is known. A calibration curve generated using numerous dilutions of a 50 mg/L haloperidol in 0.1% lactic acid aqueous solution shows that Beer's law holds true up to at least $c = 50$ mg/L, and the limit of detection for haloperidol is around $c = 0.1$ mg/L.

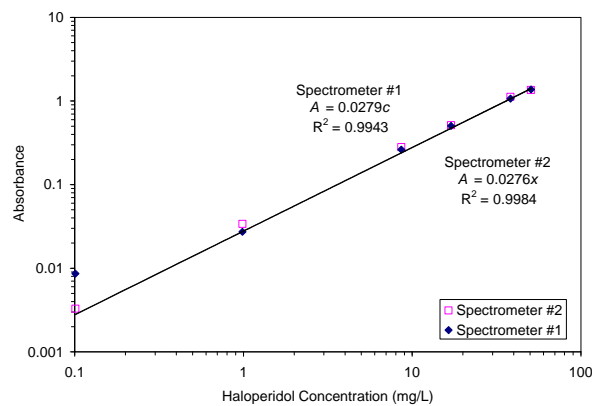


Figure 3.30 – Calibration curve of spectrophotometers using haloperidol.

3.9.4 Pure haloperidol dissolution experimental results

To test the reactor and flow system, we measure the dissolution of haloperidol in phosphate buffered saline (PBS) containing 0.02% sodium azide and 1% polysorbate 20 at a temperature of 37°C. Because the system is not closed during the experiment, we observe significant evaporation from the vessels, which are at elevated temperature. For this reason, the second parallel spectrometer is used as a baseline throughout the experiment. The photodiode gives readings in voltage, and the absorbance value is calculated using $A = -\log(V_1/(V_2 - V_{2,0} + V_{1,0}))$, where V_1 is the reading of the sample in system #1, V_2 is the reading of flow system #2, and $V_{i,0}$ is the initial reading in each system. After preparing the solution as described and heating to the proper temperature, we sprinkle ~100 mg of haloperidol on top of the stirring tank.

The dissolution results are shown in Figure 3.31. The experimental data are fit to a standard exponential curve

$$c / c_{\infty} = 1 - \exp\left(-\left(t - t_{lag}\right) / \tau\right) \quad (3.23)$$

with $c_{\infty} = 9.90$ mg/L, $t_{lag} = 0$ hr, and $\tau = 4.60$ hr. Surprisingly, the experiment did not show any increase in the equilibrium solubility of haloperidol compared to pure PBS at 37°C, which has previously been measured as ~10 mg/L (data not shown). However, the rate at which equilibrium is reached is faster than previous experiments. This is likely caused by improved wetting of the haloperidol particles due to the presence of the surfactant in the system.

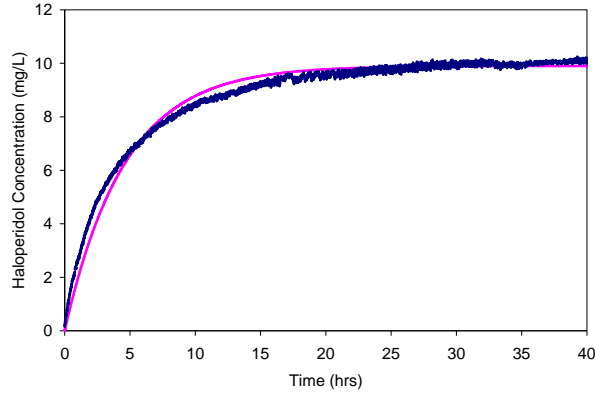


Figure 3.31 – Haloperidol dissolution into PBS at 37°C with 0.02% sodium azide and 1% polysorbate 20.

3.10 Mathematics of Fluid Flow Through a Rectangular Channel

Because the CP travels in laminar flow down a long rectangular channel through the membrane emulsifier, it is important to understand the mathematics that describe the flow profile. Figure 3.32 describes the geometry.

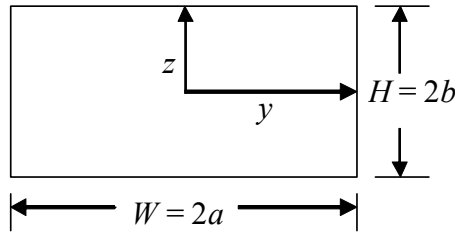


Figure 3.32 – Geometry of a rectangular channel.

For Newtonian fluids in fully developed laminar flow, solving the Navier-Stokes equation results in the following expression for the fluid velocity v_x in the x -direction as a function of position in the y and z directions.

$$\frac{v_x(y, z)}{v_{\max}} = \sum_{i=1,3,5,\dots}^{\infty} (-1)^{(i-1)/2} \left[1 - \frac{\cosh(i\pi z / 2a)}{\cosh(i\pi b / 2a)} \right] \frac{\cos(i\pi y / 2a)}{i^3} \quad (3.24)$$

However, because of the slow convergence of this infinite series, it is much more convenient to work with an approximate solution. Purday proposed the following expression²⁰

$$\frac{v_x(y, z)}{v_{\max}} = \left[1 - \left(\frac{z}{b} \right)^2 \right] \left[1 - \left(\frac{y}{a} \right)^\alpha \right] \quad (3.25)$$

with the parameter α defined as

$$\alpha = \begin{cases} 1.54 \frac{W}{H}, & 0 \leq \frac{H}{W} \leq \frac{2}{3} \\ 2.3, & \frac{2}{3} \leq \frac{H}{W} \leq 1 \end{cases}. \quad (3.26)$$

The maximum velocity v_x can be related to the total volumetric flow rate Q_{CP} through integration

$$Q_{CP} = 4v_{\max} \int_0^a \int_0^b \left[1 - \left(\frac{z}{b} \right)^2 \right] \left[1 - \left(\frac{y}{a} \right)^\alpha \right] dz dy \quad (3.27)$$

which yields

$$v_{\max} = \frac{3}{2} \left(\frac{\alpha}{\alpha + 1} \right) \frac{Q_{CP}}{HW} \quad (3.28)$$

To test the accuracy of the Purday approximation, we plot both the full solution and the approximate solution at the channel center for the two different channel heights used in this research, and Figure 3.33 is the result. As can be seen, there are only negligible differences in the two equations for the set of parameters studied here.

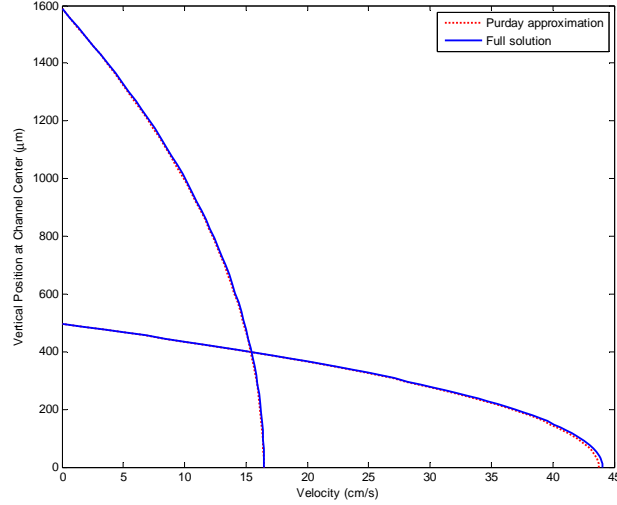


Figure 3.33 – Velocity profiles calculated for flow in a rectangular duct. Solid lines give the profile from the full analytical solution, while dotted lines give the approximate solution of Purday. Shown are the velocity profiles for the two channel heights used in our study, $b = H/2 = 1.59$ mm and $b = 0.50$ mm.

Ultimately, we are interested in the shear rate at the membrane pore, which can be calculated through differentiating the velocity profile from the Purday equation

$$\left(\frac{dv}{dz}\right)_{pore} = \frac{6Q_{CP}}{H^2W} \left(\frac{m+1}{m}\right) \quad (3.29)$$

For the special case of $1 < W/H < 3$, an alternate expression for the shear rate was derived from the full analytical solution, and this expression is included here for completeness.

$$\left(\frac{dv}{dz}\right)_{pore} = \frac{9.7Q_{CP}}{H^{1.67}W^{1.33}} \quad (3.30)$$

Either expression can be used within the specified limits, but in general the expression derived from the Purday equation is preferred due to wider applicability.

3.11 References

- (1) Slattery, J. C.; Sagis, L.; Oh, E.-S., *Interfacial Transport Phenomena*. Second ed.; Springer: New York, 2007.
- (2) Villers, D.; Platten, J. K. *Journal of Physical Chemistry* **1988**, *92*, 4023-4024.
- (3) Harkins, W. D.; Brown, F. E. *Journal of the American Chemical Society* **1919**, *41*, 499-524.
- (4) Yildirim, O. E.; Xu, Q.; Basaran, O. A. *Phys. Fluids* **2005**, *17*, 062107.
- (5) Stalder, A. F.; Kulik, G.; Sage, D.; Barbieri, L.; Hoffmann, P. *Colloid Surface A* **2006**, *286*, 92-103.
- (6) Macosko, C. W., *Rheology: principles, measurements, and applications*. Wiley-VCH: 1994.
- (7) Husny, J.; Cooper-White, J. J. *J. Non-Newton. Fluid* **2006**, *137*, 121-136.
- (8) Wischke, C.; Schwendeman, S. P. *Int. J. Pharm.* **2008**, *364*, 298-327.
- (9) Haloperidol Official FDA information, side effects and uses. www.drugs.com/pro/haloperidol-tablets.html (11/9/2008).
- (10) Cheng, Y. H.; Illum, L.; Davis, S. S. *J. Controlled Release* **1998**, *55*, 203-212.
- (11) Demoen, P. J. A. W. *J Pharm Sci-Us* **1961**, *50*, 350-353.
- (12) Budhian, A.; Siegel, S. J.; Winey, K. I. *Int. J. Pharm.* **2007**, *336*, 367-375.
- (13) Budhian, A.; Siegel, S. J.; Winey, K. I. *Int. J. Pharm.* **2008**, *346*, 151-159.
- (14) Siegel, S. J.; Kahn, J. B.; Metzger, K.; Winey, K. I.; Werner, K.; Dan, N. *Eur J Pharm Biopharm* **2006**, *64*, 287-293.
- (15) Siegel, S. J.; Winey, K. I.; Gur, R. E.; Lenox, R. H.; Bilker, W. B.; Ikeda, D.; Gandhi, N.; Zhang, W.-X. *Neuropsychopharmacology* **2002**, *26*, 817-823.
- (16) Wang, C.-K.; Wang, W.-Y.; Meyer, R. F.; Liang, Y.; Winey, K. I.; Siegel, S. J. *J. Biomed. Mater. Res. Part B Appl. Biomater.* **2010**, *93B*, 562-572.
- (17) Bergström, C. A. S.; Luthman, K.; Artursson, P. *European Journal of Pharmaceutical Sciences* **2004**, *22*, 387-398.
- (18) Ouanes, S.; Kallel, M.; Trabelsi, H.; Safta, F.; Bouzouita, K. *Journal of Pharmaceutical and Biomedical Analysis* **1998**, *17*, 361-364.
- (19) Magliozzi, J. R.; Hollister, L. E. *Journal of Clinical Psychiatry* **1985**, *46*, 20-21.
- (20) Holmes, D. B.; Vermeule, Jr. *Chem. Eng. Sci.* **1968**, *23*, 717-722.

Chapter 4: Universal dripping and jetting in a transverse shear flow

One particularly efficient approach to making emulsions having mono-sized droplets is to push a fluid through an orifice into a transverse flow of a second immiscible fluid. We find that at intermediate particle Reynolds number, the final droplet size can be readily computed using a simple force balance. Remarkably like the well-known dripping faucet, this system displays both dripping and jetting behavior, controlled by the capillary, Weber and Ohnesorge numbers of the relevant fluids, and interesting non-linear behavior such as period doubling near the transition between these two regimes.

Appeared in *Physical Review Letters*, by Robert F. Meyer and John C. Crocker, Vol. 102, Article 194501, 12 May 2009. © 2009 by The American Physical Society.

4.1 Introduction

Drop formation and breakup have long been an object of interest due to the surprising complexity of the phenomena¹. Breakup occurs either by an external force tearing a growing drop from an orifice, as in the dripping faucet, or at higher flow rates, by the breakup of a jet emerging from the orifice, as in the Rayleigh instability². Near the transition between dripping and jetting, drop formation shows interesting non-linear dynamics, including period doubling and chaos³⁻⁴. More recent studies have probed drop formation in several microfluidic geometries, such as coaxial flow⁵⁻⁶ and T-junctions⁷, where controlled droplet formation is an important technological problem.

Here, we study droplet formation in a cross-flow membrane emulsification (XME) geometry, a high-throughput method for generating mono-disperse droplets⁸⁻¹⁰. In XME, the dispersed phase (DP) is forced through an orifice in a planar membrane into a simple shear flow set up by a second continuous phase (CP) flowing parallel to the membrane surface, see Figure 4.1(a). In the dripping regime, when buoyancy forces are negligible¹¹, the final droplet diameter, D , results from the competition between hydrodynamic stresses proportional to the CP shear rate, dv/dz , and forces from the interfacial tension, γ . This leads us to introduce the capillary number, which is a ratio of a drag force, $\mu_{CP}(dv/dz)D_0^2$, and an interfacial tension force, γD_0 : $Ca = \mu_{CP}(dv/dz)D_0/\gamma$, where μ is the viscosity and D_0 the orifice diameter. At high DP flow rates, the inertial force of the fluid emerging from the orifice, $\rho_{DP}Q_{DP}^2/D_0^2$, exceeds the interfacial tension force, leading to a transition to jetting behavior, where Q is the volumetric flow rate and ρ the mass density. The ratio of these forces is the Weber number: $We = \rho_{DP}Q_{DP}^2/D_0^3\gamma$.

We find that the droplet size in the dripping regime scales with the applied forces in a manner different from those in the dripping faucet and coaxial flow geometries, but that the transition between dripping and jetting is remarkably similar. This latter point is more surprising given the lack of axial symmetry in our system.

4.2 Methods

Our experimental apparatus consists of a long rectangular channel with height $H = 3.2\text{mm}$ and width $W = 6.4\text{mm}$ through which the CP flows. The DP is forced through a single circular pore ($D_0 = 15, 90$ or $132\mu\text{m}$) on the centerline of the bottom wall, using a syringe pump. Drop formation is monitored from the side, with a viewing angle $\approx 7^\circ$ above the membrane plane, using a long-working distance video microscope. A pair of right angle prisms straddling the channel redirects illumination and viewing light through a window at the top of the channel. Several fluids were used for the DP, listed in Table 4.1, while the CP was limited to water, sometimes with poly(vinyl alcohol) (PVA) as a surfactant. For each system studied, the two fluids were equilibrated in contact, so as to minimize mass transfer during the experiment. The densities ρ_{CP} and ρ_{DP} , viscosities μ_{CP} and μ_{DP} and interfacial tension γ for each equilibrated combination were measured directly by mass, capillary viscometry and pendant drop profilometry¹², respectively (cf. Table 4.1).

Table 4.1 – Liquids used and some of their physical properties at 18°C. Mixture proportions are given in w/w. Small, medium and large symbols represent a D_0 of 15, 90 or 132 μm , respectively.

Dispersed Phase (surfactant)	ρ_{DP} (kg/m^3)	μ_{DP} (mPa s)	γ (mN/m)	Symbol
n-butanol	827	3.31	2.4	$\diamond\diamond$
n-pentanol	817	3.61	4.8	\square
n-hexanol	809	5.06	6.3	$\circ\circ$
DCM ^a + hexanol 20/80	871	3.12	7.5	\oplus
DCM + hexanol 40/60	943	1.79	9.7	\otimes
DCM + hexanol 60/40	1039	1.14	9.1	\odot
DCM (0.05% PVA)	1320	0.44	12.0	$\triangle\triangle$
DCM (0.50% PVA)	1320	0.44	6.1	∇
DCM (0.50% PVA) ^b	1320	0.44	6.1	\star
ethyl acetate	902	0.50	6.5	\blacktriangleright

^adichloromethane, ^bcomputational fluid dynamics simulation¹⁵

4.3 Qualitative results

The qualitative features of the dripping and jetting behavior in XME are shown by the images in Figure 4.1, taken at a constant Ca . At low Weber number, $We = 0.5$, simple dripping is observed, Figure 4.1(b-d). Because the interfacial force is dominant, the droplet is able to grow reproducibly each cycle until detached by the flowing CP. At $We = 1.1$, the location of droplet snap-off moves away from the orifice, but the size of the resultant droplet remains roughly the same, Figure 4.1(e-g). The momentum of the flowing DP distends the droplet neck noticeably; for these parameters the distended neck also snaps-off reproducibly to form a satellite droplet. Increasing the DP flow rate further by 20%, $We = 1.6$, causes further extension of the droplet neck, with multiple peaks and nodes observed, and a noticeable decrease in droplet size, Figure 4.1(h-j). An additional 10% increase in Q_{DP} , $We = 2.0$, leads to a stable bifurcation of the resultant droplet size, where the elongated neck/jet alternates production of small and large droplets, Figure 4.1(k-m). These and more complex non-linear dynamical behavior (not shown) were observed near the transition, over the entire range of different Ca we studied.

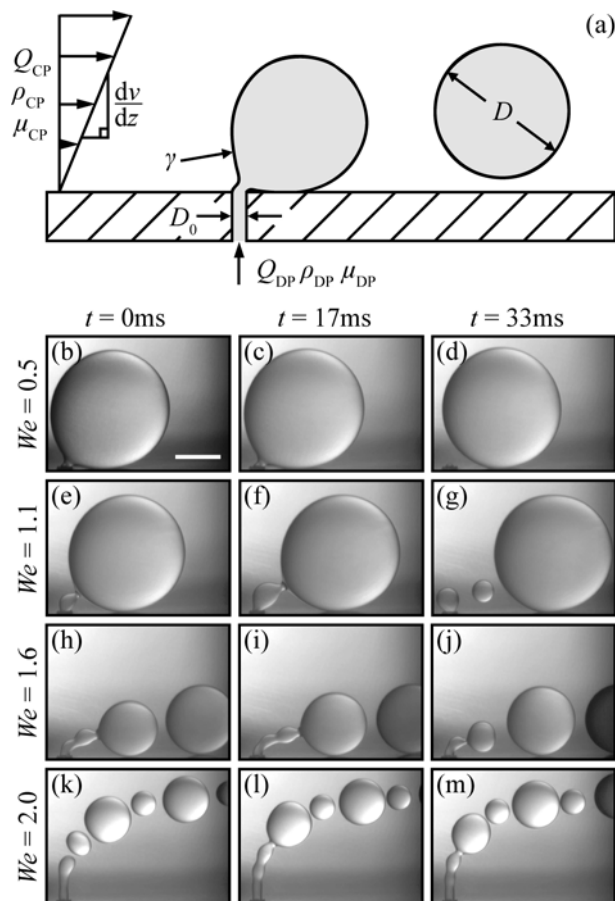


Figure 4.1 – Dripping and jetting at various We for $Ca = 8 \times 10^{-4}$ and $Oh_{DP} = 4 \times 10^{-2}$, variables defined in text. (a) Cartoon representation of the XME process, where droplets of dispersed phase (DP) are torn from an orifice by a simple shear flow in the continuous phase (CP). At low DP flow rates, monodisperse drops form and break off near the pore (b-d); scale bar = 500 μm . As the DP flow is increased, first droplets are the same size, but move away from the pore prior to snap-off, forming satellite drops (e-g). Eventually, the fluid neck lengthens further and droplet sizes decrease (h-j). Ultimately, a bent fluid jet breaks into droplets, exhibiting period doubling (k-m).

4.4 Development of droplet size model

Given the interest in using XME to produce monodisperse emulsions, we first seek to understand the particle size in the dripping regime (i.e. low We), as a function of the hydrodynamic stress due to the shear flow; typical data are shown in Figure 4.2(a).

For all systems studied, the droplet diameter scales as $D \propto (dv/dz)^{-1/2}$. This square root dependence has a simple physical origin. In our geometry, the mean velocity of the fluid at the drop center is itself proportional to the droplet size, as larger droplets poke up higher to impinge on faster flows, leading the hydrodynamic stress to depend quadratically on the droplet diameter. Equating that hydrodynamic stress with a constant, maximal interfacial tension at snap-off trivially yields the desired scaling exponent.

To make such a force balance relation more precise, we begin by equating the drag force F_d with the interfacial tension force F_γ at the moment of snap-off

$$F_d = \frac{\pi}{8} C_d \rho_{CP} v_\infty^2 D^2 = F_\gamma = \pi D_0 \gamma, \quad (4.1)$$

where v_∞ is the far-field velocity at droplet midline and $C_d = C_d(Re_p, \lambda)$ is the drag coefficient for a spherical droplet with particle Reynolds number $Re_p = \rho_{CP} v_\infty D / \mu_{CP}$ and viscosity ratio $\lambda = \mu_{DP} / \mu_{CP}$. Eq. (4.1) can be rearranged as

$$\frac{\rho_{CP}^2 v_\infty^2 D^2}{\mu_{CP}^2} = Re_p^2 = \frac{8}{C_d} \frac{\rho_{CP} D_0 \gamma}{\mu_{CP}^2} = \frac{8}{C_d} Oh_{CP}^{-2}, \quad (4.2)$$

where we have introduced the CP Ohnesorge number, $Oh_{CP} = \mu_{CP} / (\rho_{CP} D_0 \gamma)^{1/2}$, which is a ratio of viscous and capillary time scales. Solving Eq. (4.2) for the droplet diameter is not trivial since Re_p and C_d depend on D . Careful examination of Eq. (4.2) reveals that Re_p at snap-off is independent of Ca , and a function only of material properties and the pore size. Substituting the approximation $v_\infty = (D/2)(dv/dz)$ and rearranging dimensionless groups yields:

$$D/D_0 = \left\{ (32/C_d)^{1/4} Oh_{CP}^{1/2} \right\} Ca^{-1/2} = kCa^{-1/2}, \quad (4.3)$$

where we have introduced k for the prefactor in braces. The parameter k is nearly independent of Ca , and depends almost entirely on CP properties, with the only DP contribution coming from the viscosity ratio λ . Because of the small exponents on C_d and Oh_{CP} , k varies little over a wide variety of fluid-fluid systems. This corresponds to the earlier mentioned square root scaling with shear rate, as $Ca \propto dv/dz$.

For creeping flows, $Re_p < 1$, Eq. (4.3) can be solved by substituting the Hadamard and Rybczynski relation¹³, $C_d = [8(3\lambda+2)/(1+\lambda)]Re_p^{-1}$, which was derived for liquid spheres in a shear flow (in the absence of a wall), canceling Oh_{CP}

$$\left(\frac{D}{D_0} \right) = \left(\frac{2\lambda+2}{3\lambda+2} \right)^{1/2} Ca^{-1/2}. \quad (4.4)$$

Thus, for small pores and slow flows, we can derive an exact force balance expression for D/D_0 . The Re_p in our experiments, however, ranges from $2 < Re_p < 150$, so we solve Eq. (4.3) iteratively using an expression for C_d given by Saboni and Alexandrova¹³ appropriate for our intermediate Re_p case, which amounts to a 35% correction in the drop diameter for the highest Re_p . Moreover, we compute the shear rate from our measured volumetric flow rate, Q_{CP} , using an analytical solution by White¹⁴, to derive the expression $dv/dz = 9.7Q_{CP}/H^{1.67}W^{1.33}$.

Figure 4.2(b) shows the Ca dependent droplet size data, rescaled as $(1/k)D/D_0$. If our force balance were exact, the data would fall along the line $(1/k)D/D_0 = Ca^{-1/2}$. This procedure does collapse the droplet size data, with a residual spread in normalized drop sizes of about 10% across all the fluid systems studied. The collapsed data, however, fall

systematically below the expected curve by about 20%. To investigate this discrepancy, we simulated the XME process using computational fluid dynamics¹⁵⁻¹⁶. The simulation results, also plotted in Figure 4.2(b) with the symbol (\star), show excellent agreement with the experimental findings. Thus, the discrepancy is presumed due to the simplifying assumptions made in the force balance, e.g. neglecting the hydrodynamic effect of the membrane¹⁷, assuming that the drag force acts perfectly antiparallel to the interfacial tension force, or neglecting neck effects similar to those in the dripping faucet¹⁸. To predict the XME droplet size *a priori*, one should use a value about 80% of that predicted by Eq. (4.3).

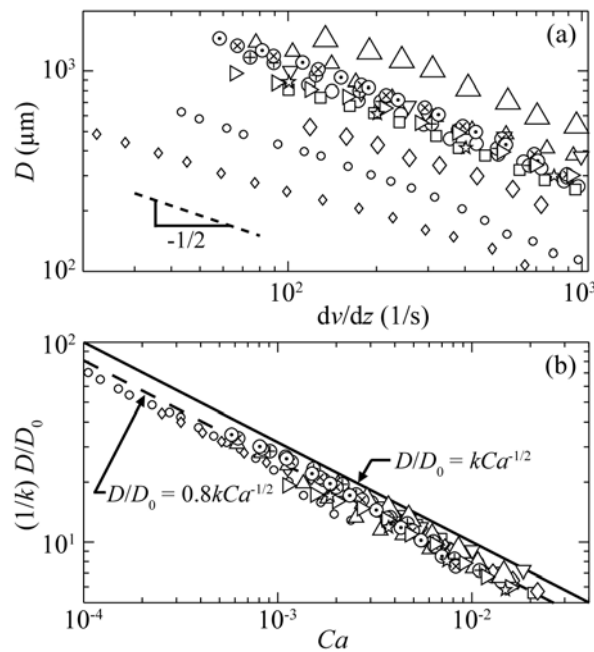


Figure 4.2 – (a) Droplet diameter D versus shear rate dv/dz for all fluid systems, and (b) Collapse of scaled droplet size $(1/k)D/D_0$ as a function of Ca , with k calculated from Eq. (4.3). The collapsed experimental data fall roughly 20% lower than the force-balance prediction (solid line), comparable to results from computational fluid dynamics (\star). See Table 4.1 for symbol definitions.

4.5 Modeling of the dripping-jetting transition

Next we construct phase diagrams that delimit where dripping and jetting occur as a function of We and Ca , shown in Figure 4.4(a,c). We define jetting as occurring when the length of the neck, L_n , at snap-off exceeds the droplet diameter: $L_n/D > 1$, which correlates with large changes in D/D_0 over the range of Ca studied, cf. Figure 4.3. A similar criterion is used in the dripping faucet literature¹⁹. At sufficiently low We and Ca , dripping is always observed, and as either is increased, the behavior will eventually transition to jetting. Qualitatively, these phase diagrams exhibit the same form as those for coaxial liquid streams⁵ and dripping faucets²⁰, at least when Ca is substituted for the Bond number Bo in the latter case.¹¹ In retrospect, one could have anticipated that jetting will occur whenever the force causing surface extension exceeds that causing surface contraction. This will happen independent of whether that force comes from the kinetic energy of the DP, the drag from the flowing CP, or from gravity. The transition, however, does not occur at the same location in $Ca-We$ space for all fluid systems, rather, it is also controlled by the DP Ohnesorge number, $Oh_{DP} = \mu_{DP}/(\rho_{DP}D_0\gamma)^{1/2}$. Figure 4.4(b) shows how the transition varies in $We-Oh_{DP}$ space at low Ca , and again we find remarkable similarity to what has been observed in the dripping faucet geometry¹⁹.

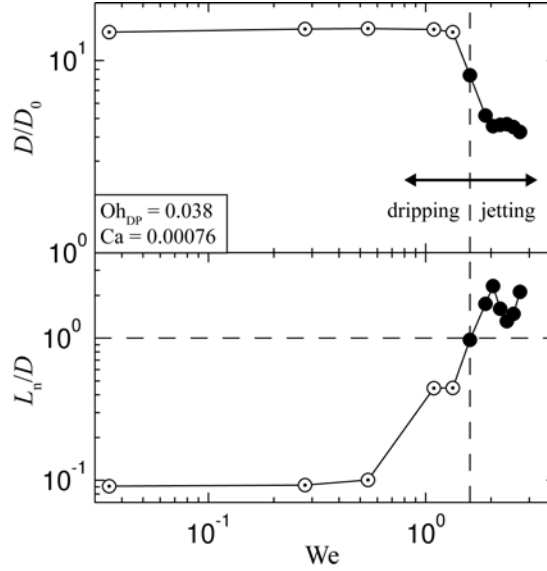


Figure 4.3 – (a) Increase in neck length L_n relative to droplet diameter D as We is increased, and (b) corresponding decrease in droplet diameter ratio D/D_0 as the dripping-jetting transition $L_n/D = 1$ is exceeded. Neck length L_n always grows near the transition, and D/D_0 subsequently varies (but does not always decrease) from the stable size observed in the dripping regime. See Table 4.1 for symbol definitions.

In the dripping faucet, the separatrix between dripping and jetting has been determined. Clanet and Lasheras derived an analytical expression²⁰ to describe the dripping-jetting transition in $We-Bo$ space when $Oh_{DP} \rightarrow 0$. For finite Oh_{DP} , their expression quantitatively describes our low and high Oh_{DP} data when their We and Bo are replaced by a rescaled We and Ca , respectively, as shown by the solid lines in Figure 4.4(a) and Figure 4.4(c). Similarly, Ambravaneswaran et al. generated a phase diagram in $We-Oh_{DP}$ space at fixed Bo through numerical simulations¹⁹; their data are reasonably well described by a two-segment piecewise power-law in Oh_{DP} (corresponding to the inviscid and finite μ_{DP} limits). Again, this expression describes our data when Oh_{DP} is rescaled; the solid line in Figure 4.4(b) shows this result. We find that the product of

these two functions (with rescaled Ca and Oh_{DP}) describes our dripping-jetting transition surface in Ca - Oh_{DP} - We space:

$$We = (c_1 Oh_{DP}^{-\alpha}) \left\{ 1 + c_2 Ca^2 - \left[(1 + c_2 Ca^2)^2 - 1 \right]^{1/2} \right\}, \quad (4.5)$$

where $c_2 = 860$, and $c_1 = 0.10$ and $\alpha = 0.89$ for $Oh_{DP} \geq 0.03$, or $c_1 = 2.27 = (0.10)(0.03)^{0.89}$ and $\alpha = 0$ for $Oh_{DP} < 0.03$, as determined by least squares minimization. This surface is plotted in Figure 4.4(d).

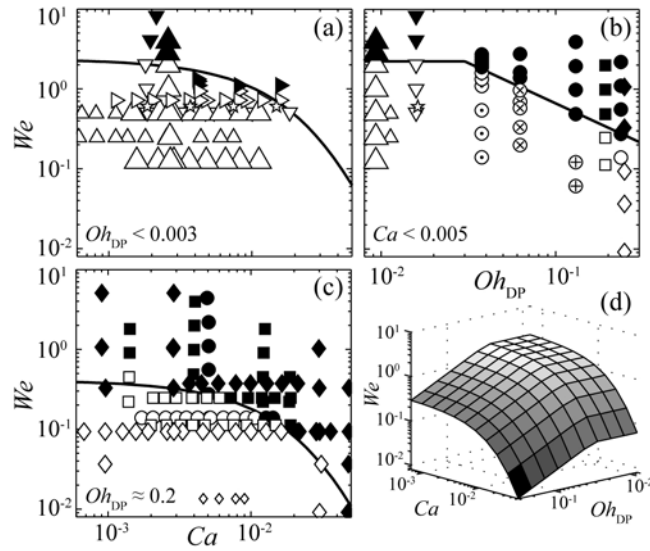


Figure 4.4 – Dripping to jetting phase behavior as a function of We , Ca and Oh_{DP} . Dripping is indicated by open symbols, jetting by filled symbols. In (a) and (c), which plot the same region of Ca - We space at different Oh_{DP} , jetting is always seen at sufficiently high values of either We or Ca . The transition curve, shown by the solid lines, is a function of Oh_{DP} and moves downward as Oh_{DP} is increased. In (b), viewing the data in Oh_{DP} - We space highlights the Oh_{DP} dependence (at low Ca). In (d), the surface separating dripping and jetting regimes, based on Eq. (4.5), is adapted from the references.¹⁹⁻²⁰. Jetting can also be observed below this surface if the predicted droplet size is $D/D_0 < 2$, not shown. See Table 4.1 for symbol definitions.

We also observe another dripping to jetting transition mechanism. Even at small Ca and We , under conditions where Eq. (4.3) predicts droplet sizes below the Rayleigh limit $D/D_0 \approx 2$, dripping gives way to a jet running tangent to the membrane, without apparently wetting it. In this case, the jet breaks up downstream to yield droplets of size $D/D_0 \approx 2$. This condition resembles operating conditions that prevail during emulsification in T-junctions⁷. Taken with the preceding result, the (Ca, Oh_{DP}, We) triple appears sufficient to determine whether dripping or jetting will occur during any XME process.

4.6 Summary

Dripping, jetting and the transition between them show remarkably similar characteristics in radically different geometries. Indeed, we were even able to adapt and analytically extend functional forms derived for the transition in faucets to the XME geometry with simple rescaling of the groups. Less surprising, the geometric details influence the relationship between droplet size and the relevant dimensionless groups. In the cross-flow membrane geometry as in the others, a force balance suffices for a precise prediction of droplet size as a function of process conditions. It seems likely that such relationships prevail in other microfluidic geometries as well. It remains unknown to what extent the lack of axisymmetry in our geometry affects the hydrodynamic singularity at the moment of snap-off²¹, or how the process is modified by non-Newtonian fluid behaviors such as extensional elasticity²².

4.7 Acknowledgements

We thank M.T. McClendon for developing the pendant drop profile analysis technique and W.B. Rogers for helpful discussions. This work was supported by Merck & Co., Inc.

4.8 References

- (1) Eggers, J. *Rev. Mod. Phys.* **1997**, *69*, 865-929.
- (2) Rayleigh, L. *Proc. R. Soc. London* **1879**, *29*, 71-97.
- (3) Ambravaneswaran, B.; Phillips, S. D.; Basaran, O. A. *Phys. Rev. Lett.* **2000**, *85*, 5332.
- (4) Garstecki, P.; Fuerstman, M. J.; Whitesides, G. M. *Phys. Rev. Lett.* **2005**, *94*, 234502-234504.
- (5) Utada, A. S.; Fernandez-Nieves, A.; Stone, H. A.; Weitz, D. A. *Phys. Rev. Lett.* **2007**, *99*, 094502-094504.
- (6) Umbanhowar, P. B.; Prasad, V.; Weitz, D. A. *Langmuir* **2000**, *16*, 347-351.
- (7) van der Graaf, S.; Steegmans, M. L. J.; van der Sman, R. G. M.; Schroen, C. G. P. H.; Boom, R. M. *Colloids Surf., A* **2005**, *266*, 106-116.
- (8) Gijsbertsen-Abrahamse, A. J.; van der Padt, A.; Boom, R. M. *J. Membr. Sci.* **2004**, *230*, 149-159.
- (9) Joscelyne, S. M.; Trägårdh, G. *J. Membr. Sci.* **2000**, *169*, 107-117.
- (10) Kobayashi, I.; Nakajima, M.; Chun, K.; Kikuchi, Y.; Fujita, H. *AIChE J.* **2002**, *48*, 1639-1644.
- (11) The strength of the buoyancy force relative to the interfacial tension force is characterized by the Bond number, $Bo = \Delta\rho g D^2 / \gamma$, and is negligible so long as $Bo \ll 1$. In our experiments, $Bo < 0.5$ in all cases.
- (12) Song, B.; Springer, J. *J. Colloid Interface Sci.* **1996**, *184*, 64-76.
- (13) Saboni, A.; Alexandrova, S. *AIChE J.* **2002**, *48*, 2992-2994.
- (14) White, F. M., *Viscous Fluid Flow*. McGraw-Hill: New York, 1974.
- (15) CFD calculations were performed with the Fluent 6.3 software package using the unsteady-state Volume Of Fluid simulation scheme. Calculations were performed using a 6×10^5 cell grid with a symmetry plane dividing the space in two. Time steps were typically 10^{-5} s. The constant physical properties used were given in Table 4.1. Boundary conditions were constant velocity at both inlets, constant pressure at the outlet, and a contact angle of 180° between the DP and the chamber walls.
- (16) Abrahamse, A. J.; Padt, A. v. d.; Boom, R. M.; Heij, W. B. C. d. *AIChE J.* **2001**, *47*, 1285-1291.
- (17) O'Neill, M. E. *Chem. Eng. Sci.* **1968**, *23*, 1293-1298.
- (18) Harkins, W. D.; Brown, F. E. *J. Am. Chem. Soc.* **1919**, *41*, 499
- (19) Ambravaneswaran, B.; Subramani, H. J.; Phillips, S. D.; Basaran, O. A. *Phys. Rev. Lett.* **2004**, *93*, 034501.
- (20) Clanet, C.; Lasheras, J. C. *J. Fluid Mech.* **2000**, *383*, 307-326.

- (21) Cohen, I.; Brenner, M. P.; Eggers, J.; Nagel, S. R. *Phys. Rev. Lett.* **1999**, *83*, 1147-1150.
- (22) Arratia, P. E.; Thomas, C. C.; Diorio, J.; Gollub, J. P. *Phys. Rev. Lett.* **2006**, *96*, 144502-144505.

Chapter 5: Producing Monodisperse Drug-Loaded Polymer Microspheres via Cross-Flow Membrane Emulsification: The Effects of Polymers and Surfactants

Cross-flow membrane emulsification (XME) is a method for producing highly uniform droplets by forcing a fluid through a small orifice into a transverse flow of a second, immiscible fluid. We investigate the feasibility of using XME to produce monodisperse solid microspheres made of a hydrolysable polymer and a hydrophobic drug, a model system for depot drug delivery applications. This entails the emulsification of a drug and polymer-loaded volatile solvent into water followed by evaporation of the solvent. We use a unique side-view visualization technique to observe the details of emulsion droplet production, providing direct information regarding droplet size, dripping frequency, wetting of the membrane surface by the two phases, neck thinning during droplet break off, and droplet deformation before and after break off. To probe the effects that dissolved polymers, surfactants, and dynamic interfacial tension may have on droplet production, we compare our results to a polymer and surfactant-free fluid system with closely matched physical properties. Comparing the two systems, we find little difference in the variation of particle size as a function of continuous phase flow rate. In contrast, at low dripping frequencies, dynamic interfacial tension causes the particle size to vary significantly with drip frequency, which is not seen in simple fluids. No effects due to shear thinning or fluid elasticity are detected. Overall, we find no significant impediments to the application of XME to forming highly uniform drug-loaded microspheres.

Appeared in *Langmuir*, by Robert F. Meyer, W. Benjamin Rogers, Mark T. McClendon and John C. Crocker, Vol. 26, Issue 18, pp. 14479-14487. © 2010 by American Chemical Society.

5.1 Introduction

Emulsion-based materials have a diverse set of applications across many fields including electronics, cosmetics, foods, and pharmaceuticals¹. In controlled release drug delivery applications, it has been shown that particles generated from monodisperse emulsions have well defined drug release rates, and thus particle size can be used to engineer improved formulations that deliver drug in a predetermined manner²⁻³. Methods for producing monodisperse emulsions have been a popular topic of investigation in recent years, employing techniques such as flow focusing⁴, shear rupturing⁵, acoustic excitation⁶, microfluidic T-junction emulsification⁷, and membrane emulsification⁸. Membrane emulsification describes a wide variety of techniques whereby a dispersed phase (DP) is forced through an orifice in a membrane into an immiscible continuous phase (CP), thereby generating an emulsion. To date, researchers have investigated the impact of the type of membrane and pore used, the method for detaching emulsion droplets, and the geometry in which the droplets are formed^{1, 9-10}.

We focus on cross-flow membrane emulsification (XME), due to the wide adjustability of particle size and the potential for high production rates through the use of multiple orifices in one device. In XME, nascent droplets are formed at the membrane pore while subjected to a transverse shear flow, as shown in Figure 5.1(a). The drag force exerted by the CP increases as the drop grows larger, until such point that the interfacial tension force can no longer hold onto the drop, and the process begins anew. It is this balance of drag and interfacial tension forces which allows for precise control over the size of the droplets which are produced, as we showed recently in simple fluids¹¹.

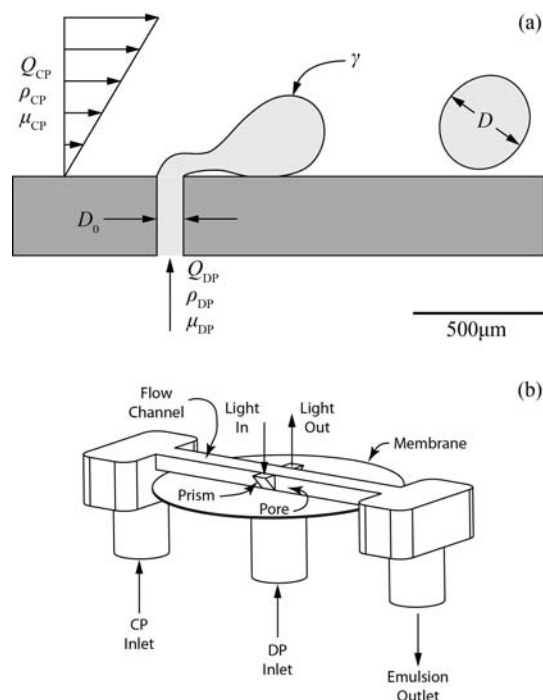


Figure 5.1 – (a) Schematic of the XME process and the important parameters, and (b) scale rendering of the CP fluid channel, membrane and optical path. All components are contained within a machined aluminum carrier which is not shown.

For many practical applications, including the production of drug-loaded microspheres¹², emulsions must contain polymers, surfactants, and other substances which introduce non-idealities into the system's fluid mechanics. In this work, we examine the feasibility of using XME to generate such drug-loaded particles. Specifically, we investigate whether non-Newtonian viscosity, elasticity, and dynamic interfacial tension modify the XME process in an observable way, largely by comparing the drug and polymer-loaded system to a simple fluid system with similar physical properties. Next, we investigate operational aspects related to the production of particles, including the uniformity of particles produced. Finally, we explore droplet deformation

and rupture which can occur after particle generation but prior to drying, and result in size distributions of lower uniformity.

5.2 Background

Because membrane emulsification has received significant attention in recent years, considerable background can be found in recent review papers^{1, 9-10, 12}. XME in particular was studied experimentally by Peng and Williams¹³, and numerically by Abrahamse, et al.¹⁴ The effect of dynamic interfacial tension on XME was studied by van der Graaf, et al.¹⁵, but their study did not show a clear relationship between droplet production rate, the interfacial tension at that rate, and the resultant droplet size. Using a T-shaped microchannel geometry, Husny and Cooper-White¹⁶ demonstrated the substantial consequences fluid elasticity has on droplet production, including long-lived droplet necks and abundant satellite droplets. However, this study used a DP of water with dilute concentrations of high molecular weight poly(ethylene oxide), which is well known to exhibit elastic effects, and was not oriented towards manufacturing solid particles. Preparation of PLG particles using stirred cell membrane emulsification was performed by Gasparini et al.¹⁷, and this study investigated many aspects of the process, including formulation variables and the drying procedure, but the study generated fairly polydisperse particles and did not investigate the physics of the emulsification process itself.

In our earlier study in pure fluids¹¹, we found two distinct processing regimes: dripping and jetting. When the DP volumetric flow rate, Q_{DP} , is sufficiently low, the system will drip, and droplets of constant size are formed and detach near the membrane

pore. The final droplet diameter, D , decreases in relation to the magnitude of the shear stress, which is proportional to the CP viscosity, μ_{CP} , and the CP shear rate, dv/dz . Conversely, D increases in relation to the interfacial tension, γ , and the pore diameter, D_0 . This leads us to introduce the capillary number Ca , which is a ratio of these drag and interfacial forces: $Ca = \mu_{CP}(dv/dz)D_0/\gamma$. These are the only two significant forces present as long as buoyancy is negligible, which is the case for the small droplets studied here. At higher Q_{DP} , the inertia of the DP can no longer be neglected. A jet forms, and the jet breaks into rather polydisperse droplets far from the membrane pore due to the Rayleigh instability¹⁸. The system gets closer to jetting with increasing inertial force of the DP, $\rho_{DP}Q_{DP}^2/D_0^2$, where ρ_{DP} is the DP mass density. However, the tendency to jet is decreased by the interfacial tension force, γD_0 . Thus we are interested also in the ratio of these forces, which is the Weber number, $We = \rho_{DP}Q_{DP}^2/D_0^3\gamma$.

For a system consisting of pure fluids, we can use dimensional analysis¹⁹ to determine the dimensionless groups other than Ca and We which might be useful for study. In XME there are 5 physical properties, 2 flow rates, and 2 length scales that are relevant. Since these contain the dimensions of length, mass and time, there should be at most $9 - 3 = 6$ independent dimensionless groups. It is intuitive that the droplet diameter ratio D/D_0 is a function of We and Ca , but dimensional analysis indicates that there are three additional dimensionless groups present. These can be chosen as a viscosity ratio $\lambda = \mu_{DP}/\mu_{CP}$, and two Ohnesorge numbers, Oh_{CP} and Oh_{DP} , where $Oh = \mu/(\rho D_0 \gamma)^{1/2}$. The Ohnesorge numbers for each phase are a ratio of viscous and capillary time scales within

that phase. Thus it is expected that $D/D_0 = f(\text{Ca}, \text{We}, \text{Oh}_{\text{DP}}, \text{Oh}_{\text{CP}}, \lambda)$. In practice, it has been shown that for systems of low to moderate Oh_{DP} operating at low We ¹¹:

$$\frac{D}{D_0} = k_0 \text{Ca}^{-1/2} \quad (5.1)$$

where k_0 is a function of physical properties and length scales alone, and can be treated as a constant within a given experiment. The value of k_0 can be calculated according to

$$k_0 = \left(\frac{32}{C_d} \right)^{1/4} \text{Oh}_{\text{CP}}^{1/2}. \quad (5.2)$$

In the preceding expression, C_d is the drag coefficient for the droplet in the cross-flowing CP, and can be estimated from empirical correlations²⁰ which relate to the Reynolds number $\text{Re} = \rho v_{\text{CP}} D / \mu$, and the viscosity ratio λ :

$$C_d = \frac{\left[\lambda \left(\frac{24}{\text{Re}} + \frac{4}{\text{Re}^{1/3}} \right) + \frac{14.9}{\text{Re}^{0.78}} \right] \text{Re}^2 + 40 \frac{3\lambda + 2}{\text{Re}} + 15\lambda + 10}{(1 + \lambda)(5 + \text{Re}^2)}. \quad (5.3)$$

This expression, derived for fluid spheres in an external flow (in the absence of a wall) is accurate for $0.01 < \text{Re} < 400$ and any viscosity ratio. It should be noted that Re is not an independent dimensionless group, and can be expressed in terms of the other groups previously discussed, $\text{Re} = \text{Ca} \text{Oh}_{\text{CP}}^{-2} (D/D_0)^2$.

5.3 Methods

5.3.1 Experimental Apparatus

Figure 5.1(a) shows a schematic of the XME process, and Figure 5.1(b) shows an isometric drawing of the interior of the apparatus used in these experiments. The

membrane holder is constructed from aluminum stock, and consists of a top and bottom half, between which the membrane is sandwiched. CP is pushed from a pressurized tank through a flowmeter (FMTE4, DEA Engineering, Anza, CA) and into the membrane holder from the bottom. DP is pumped into the bottom of the membrane holder using a syringe pump (Model 11 Plus, Harvard Apparatus, Harvard MA). The pressures of both CP and DP are measured via pressure transducers (SPT4V, Invensys, Milpitas, CA). After changing direction, the CP flows along the membrane surface down a long rectangular channel 6.4mm wide by 3.2mm high. In some experiments, a solid insert is placed in the channel to decrease the height to 1.0mm. In the center of the channel, DP passes through the membrane and into the cross-flowing CP, generating a droplet. The emulsion then travels down the remainder of the channel, and exits the membrane holder at the bottom, and finally proceeds to the collection vessel.

5.3.2 Membranes

Disk-shaped membranes are constructed of stainless steel and cut to 50mm in diameter from 0.30mm thick sheet stock. For each membrane, a single pore is cut into the center of the membrane using one of three methods: laser drilling (Oxford Lasers, Shirley, MA), mechanical drilling (Roland Research Devices, Trenton, NJ), or electrical discharge machining (EDM) (Makino / Hummingbird Precision Machine Co., Lacey, WA). Electron micrographs showing the pores made via the various methods are provided in Figure 5.2. For the majority of the studies, the mechanically drilled membrane shown in Figure 5.2(c) is used, because of the membrane's favorable wetting properties. Wetting of the membrane by the DP, readily visualized in our apparatus, can lead to a larger effective orifice size, and correspondingly anomalous droplet sizes. The

EDM membrane in Figure 5.2(b) is used for the mass-produced particles shown in Figure 12, while the laser drilled membrane in Figure 5.2(a) is not used in the present work, but is shown for comparison purposes.

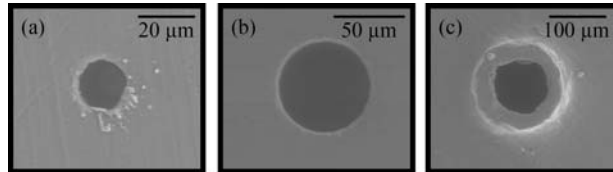


Figure 5.2 – Membranes manufactured via different methods.

Parts (a), (b) and (c) show stainless steel membranes of varying pore diameters, manufactured using laser drilling, electrical discharge machining (EDM), and mechanical drilling, respectively.

5.3.3 Video Microscopy

During production of the emulsion droplets, the process is observed from the side of the channel, through the use of two 1/8" right-angle prisms (Thorlabs, Newton, NJ) flush mounted in the channel wall. Light is directed from above into the first prism, where it is then reflected through the droplet-forming region and into the second prism. The second prism subsequently reflects the light up through a long working distance video microscope and into a CCD camera (COHU 4915, San Diego, CA) collecting 30 interlaced frames per second at 640 x 480 resolution. Video images are collected using Video Toolbox (version 1.65, Zarbeco, Randolph, NJ), processed using VirtualDub (version 1.6.19, virtualdub.org), and analyzed using ImageJ (version 1.38x, rsb.info.nih.gov) and Matlab (R2007a, The Mathworks, Natick, MA).

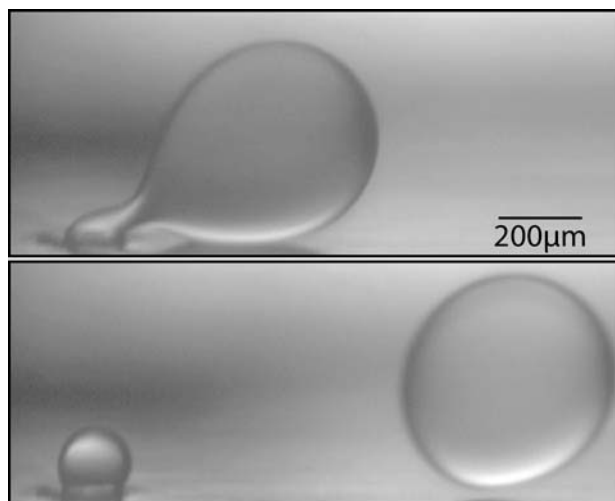


Figure 5.3 – Example images of PLG droplets. The side view set up allows for observation of phenomena not observable from above, such as wetting of the membrane surface, thinning of the droplet neck during break-off, and droplet deformation due to the shear flow.

5.3.4 Materials

When generating drug loaded polymer microspheres, the DP consists of the solvent dichloromethane (DCM), the biodegradable polymer poly(D,L-lactide-*co*-glycolide) (PLG), and haloperidol as a model drug. DCM was obtained from Fisher Scientific (Fairlawn, NJ). PLG (50:50 D,L-lactide:glycolide, ester terminated, inherent viscosity = 0.82dL/g in HFIP) was obtained from Birmingham Polymers (Pelham, AL). Haloperidol was obtained from Sigma (St. Louis, MO). The CP consists of the surfactant poly(vinyl alcohol) (PVA) dissolved in deionized (DI) water. PVA (22kDa, 88% hydrolyzed) was obtained from Acros Organics (New Jersey, USA). DI water (18 MΩ/cm, Easypure Barnstead) was used throughout this study. For comparison to ideal fluids, 1-decanol (Acros Organics) acts as the DP, and the CP consists of DI water.

Table 5.1 – Formulations of decanol and polymer-loaded systems.

System	CP	DP
Decanol	DI water	decanol
Polymer	99% DI water 1% PVA	90% DCM 9% PLG 1% haloperidol

5.3.5 Preparation of CP and DP

For the production of polymer microspheres, CP is prepared by dissolving PVA in warm DI water at a concentration of 1% by weight. After dissolution of the PVA, the solution is filtered through a 14 μ m cellulose acetate filter and allowed to cool to room temperature. DP is prepared by mixing haloperidol, PLG and DCM in a closed container overnight. In most experiments, the DP contained 9% PLG and 1% haloperidol on a weight basis, and in one experiment, the concentrations were raised to 11% PLG and 1.2% haloperidol so that droplets could be collected and dried without affecting the particle size distribution.

5.3.6 Microsphere Drying

The classical oil-in-water emulsion-solvent evaporation method is used in preparation of the microspheres²¹⁻²². In brief, after production of the emulsion droplets via XME, DCM is extracted into the CP, where it is sparingly soluble. The DCM is then readily evaporated from the collection vessel due to its low boiling point, yielding solid drug-loaded polymer microspheres.

5.3.7 Sizing of Microspheres

In most experiments, the droplets produced via XME are deformed from a sphere and into a prolate spheroid due to the shear stress imposed by the flowing CP. This

complicates slightly the measurement of particle size. The diameter of a droplet is measured in two ways. In the simplified method, the major and minor diameters are measured manually from a video frame containing the droplet image. When higher resolution and/or larger sample sizes are needed, an automated image analysis routine processes the images such that an ellipse can be fit to the droplet perimeter. In both cases, the reported diameter is then calculated as the average of the major and minor diameters. While an assumption that the particle takes the shape of a prolate spheroid with equivalent spherical diameter $D = (D_{\text{minor}}^2 D_{\text{major}})^{1/3}$ may be more appropriate for highly deformed particles, for the small deformations seen here the result is indistinguishable from this and other advanced diameter calculation techniques.

5.3.8 Physical Properties

Fluid physical properties are calculated in the following ways. Densities are calculated by weighing a known volume of fluid. Viscosity is measured by capillary viscometry in an Ubbelohde viscometer. Interfacial tension is measured via the drop weight method, which was analyzed in detail by Yildirim, Xu and Basaran²³. In this technique, the interfacial tension between the two phases is inferred by measurement of the weight of a drop that falls from a needle tip, and applying an empirical correlation. By varying the rate of droplet production, we are able to measure the interfacial tension at the moment of drop snap-off, as a function of the drop period. This dynamic interfacial tension is a complex phenomenon, and has been well described in a recent review paper by Eastoe and Dalton²⁴. The physical properties of the various DPs are provided in Table 5.2.

Table 5.2 – Physical properties of decanol and polymer-loaded systems.

$T=18^{\circ}\text{C}$ System	DP Properties		CP Properties		CP/DP	Calculated		
	ρ (kg/m^3)	μ ($\text{mPa}\cdot\text{s}$)	ρ (kg/m^3)	μ ($\text{mPa}\cdot\text{s}$)	γ (mN/m)	Oh_{CP}	Oh_{DP}	λ
Decanol	824	13.6	998	0.98	9.5	0.034	0.514	13.9
Polymer	1327	14.9	998	1.41	8.0*	0.053*	0.483*	10.6

*evaluated at a drop period of $\Delta t = 1\text{ s}$ using the drop weight method²³

5.3.9 Calculation and Measurement of Channel Shear Rate

To relate the measured CP volumetric flow rate Q_{CP} to the shear rate dv/dz in the center of the channel and at the membrane surface, we utilize an empirical expression proposed by Purday²⁵

$$\left(\frac{dv}{dz}\right)_{\text{pore}} = \frac{6Q_{\text{CP}}}{H^2W} \left(\frac{m+1}{m}\right) \quad (5.4)$$

where H is the channel height, W is the channel width, and m is an empirical factor defined by $m = 1.54W/H$ when $H/W < 2/3$. This expression is far less cumbersome than the full analytical solution for laminar flow in a rectangular channel, and has minimal error across the range of conditions studied here.

To confirm the predictions of Eq. (5.4), titania coated glass microspheres (Isospheres-T, Microsphere Technology, Edinburgh, UK) are used to observe the CP flow dynamics *in situ*. The microspheres are observable as a dark spot on a bright background, but only when they are within the focal plane of the microscope. Because we are interested in the velocity at the center of the channel, and the channel is wide with respect to its height, variations in the depth of observed microspheres are unimportant. By analyzing the movement of individual microspheres across adjacent video frames, the velocity of the microspheres and thus the carrier fluid can be calculated.

5.4 Results and Discussion

We are primarily concerned with the size of the particles that are produced, and the rate of their production, and these factors can be controlled by two parameters within a given experiment: Q_{CP} and Q_{DP} . These flow rates are directly proportional to the more intuitive parameters of shear rate, dv/dz , and DP velocity, $v_{DP} = 4Q_{DP}/\pi D_0^2$. Looking first at the size of droplets produced as a function of the shear rate, we find there is great similarity when comparing the PLG and decanol systems, see Figure 5.4. This is surprising given the complexity of the PLG system relative to the decanol system. Both show the expected trend of rapidly decreasing particle size with the initial increase in shear rate, followed by more gradual decreases as the shear rate is increased further. This will be shown later to be consistent with the model presented in Eq. (5.1), which states that $D \propto (dv/dz)^{-1/2}$.

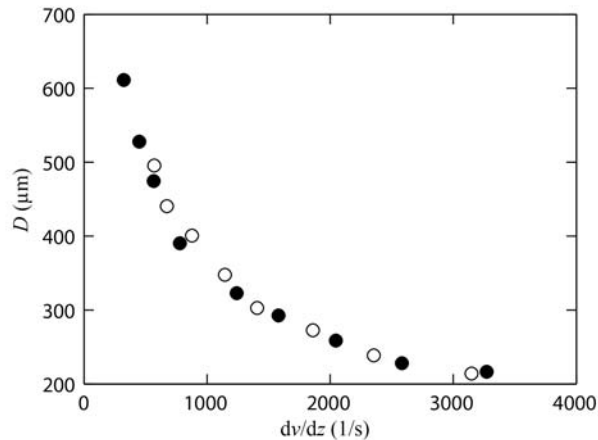


Figure 5.4 – Drop diameter D as a function of CP shear rate dv/dz for the PLG (filled circles) and decanol (open circles) systems. For both systems, $D_0 = 90\mu\text{m}$, and the flow rates were similar at $Q_{DP} = 0.7\text{mL/hr}$ and $Q_{DP} = 1.0\text{mL/hr}$ for the PLG and decanol systems, respectively.

In Figure 5.5, we examine the size of droplets produced as a function of Q_{DP} , while dv/dz is held constant. In general, a small increase in D is expected as Q_{DP} is increased, as has been seen in both XME²⁶⁻²⁷ and in other geometries²³. Indeed, this trend is observed, and as can be seen, there is a significant difference in the functional relationship between the decanol and PLG systems. The decanol system shows a gradual linear increase in D as Q_{DP} is increased, with a slope of about $20\mu\text{m}/(\text{mL}/\text{hr})$. The PLG system shows a similar increase in D at high flow rates, but shows a drastic change in D at low flow rates. These two trends are consistently seen independent of the value of dv/dz . It appears that the primary difference between the decanol and PLG systems is this dependence of particle size on production rate.

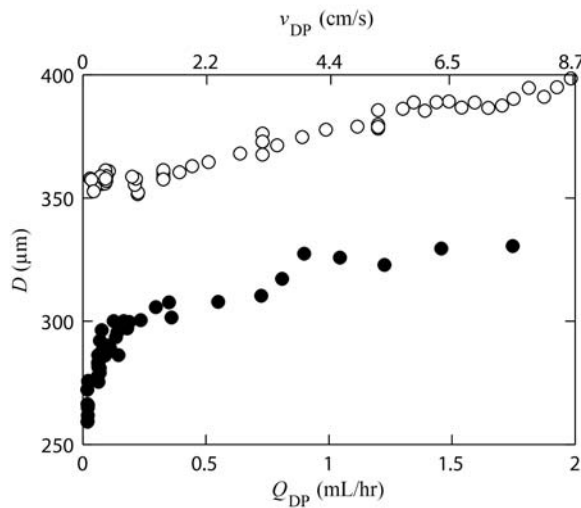


Figure 5.5 – Drop diameter D as a function of DP flow rate Q_{DP} or velocity v_{DP} for the PLG (filled circles) and decanol (open circles) systems. For both systems, $D_0 = 90\mu\text{m}$, and the CP shear rates were similar at $dv/dz = 1210\text{s}^{-1}$ and $dv/dz = 970\text{s}^{-1}$ for the PLG and decanol systems, respectively.

Since in a production setting, the DP flow rate determines the rate of particle production, it is desirable to modify the size model given in Eq. (5.1) in such a way that

the model is predictive of particle size as a function of both dv/dz and Q_{DP} . It is clear from Figure 5.5 that for decanol, at constant dv/dz , $D = mQ_{DP} + b$, where m and b are constants for a given shear rate. In non-dimensional form, the relationship can be generalized to

$$\frac{D}{D_0} = (k_0 + k_1 We^{1/2}) Ca^{-1/2} \quad (5.5)$$

where k_1 is a constant for a given experiment with set dv/dz , and is expected to be a function of Oh_{DP} . This relationship is consistent with what has been observed in the dripping faucet²³, a geometry quite similar to that encountered in XME. Of course this model is phenomenological in nature, and does little to help elucidate the cause of the phenomena we observe. Yet it will prove useful in analyzing the differences seen between our simple decanol and complex polymer systems.

While it seems natural when comparing these systems to utilize the dimensionless variables introduced earlier; such an approach is complicated by the complexities of the PLG system. In particular, shear thinning of the CP, viscoelasticity of the DP, and dynamic interfacial tension can all cause the physical properties of the system to become functions of the process conditions, leading them to be coupled in non-trivial ways. Thus before non-dimensionalizing the systems under study, we check the requisite physical properties for non-ideal behavior.

PVA is a common polymeric surfactant for manufacturing PLG microspheres, due to its ability to lower interfacial tension and stabilize emulsion droplets against coalescence²¹⁻²². Relative to pure water, it also raises the viscosity of the CP by about 40% at a concentration of 1% by weight. This then increases the shear stress at a given

shear rate. But for polymer solutions, viscosity is often a function of shear rate, and typically decreases with increasing shear. If this were the case, it would negate the assumed velocity profile and subsequent calculations. Because of our ability to observe the region of droplet formation from the side, we use particle velocimetry to observe the velocity profile *in situ*²⁵. Typical results are provided in Figure 5.6. For all cases studied, the experimentally measured v_{CP} and dv/dz match the theoretical predictions from Eq. (5.4) to within experimental error, and thus we conclude that an assumption of constant viscosity in the CP is appropriate.

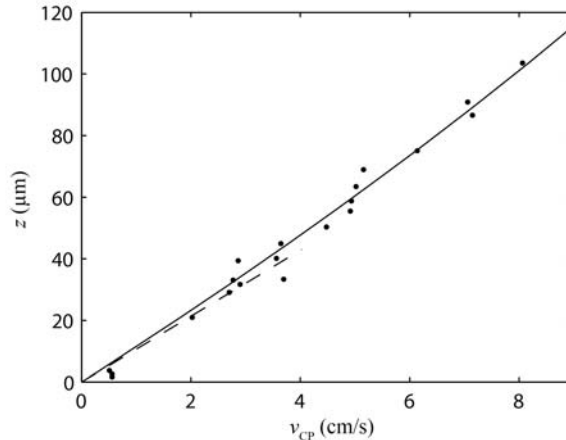


Figure 5.6 – Distance from membrane surface as a function of continuous phase velocity v_{CP} for the PLG system with a CP containing 1% PVA. Solid points are experimentally measured velocities, the solid line is the theoretical prediction, and the dashed line is the slope at the wall based on a parabolic least-squares fit to the entire data set.

Having examined the CP and finding no effects of the dissolved polymer, we now investigate the DP, where the polymer is present at much higher concentration and has higher molecular weight. There are two possible effects that could influence the dynamics of our system. As before, we would not be surprised to find that the viscosity

is shear thinning. However, once the DP passes through the membrane and into the CP, it experiences only a moderate shear rate due to its high viscosity and stress continuity at the DP/CP interface. In addition, DP shear viscosity only plays a minor role in the size model presented here, Eqs. (5.1) and (5.3). Thus it is not expected that shear thinning in the DP will cause any deleterious behavior during XME. It is also possible that elastic effects such as non-linear elongational viscosity could be observed, which result in long-lived droplet necks, and thus droplets that detach far from the membrane pore along with numerous satellite drops¹⁶. To test for this second possibility, we measure the diameter of a droplet neck, from the first instant of droplet formation up until the critical time of neck breakage, t_c . If no elastic effects are present, the neck diameter should decrease in size according to $D_n \sim (t_c - t)^{2/3}$. Figure 5.7 shows the results, which are generated by imaging the process stroboscopically. That is, by adjusting the dripping frequency to near a multiple of the frame rate we can access sub-millisecond dynamics with a conventional video camera. In general, we see only slight differences between the decanol and PLG systems, and both systems display the expected scaling of D_n with t at times near the critical point. Furthermore, we do not witness the long lived droplet necks seen elsewhere, thereby indicating the lack of significant elastic effects^{16,28}.

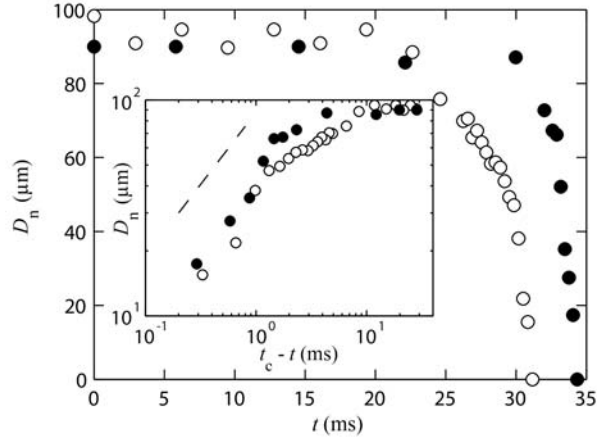


Figure 5.7 – Droplet neck diameter D_n as a function of time t for the PLG (filled circles) and decanol (open circles) systems. The difference in breakup time is due to slightly different production rates. The inset shows the same data plotted as D_n vs. $(t_c - t)$ on logarithmic coordinates, where t_c is the critical time of neck breakage; the dashed line demonstrates the theoretically predicted slope of $2/3$.

Although not observed in the current system, in general, nonlinear elongational elasticity is expected to arise if the relaxation time of the polymer exceeds the characteristic flow time within the droplet neck, i.e. the Deborah number $De = \lambda \dot{\epsilon} > 1$, where λ is the longest polymer relaxation time and $\dot{\epsilon}$ is the highest strain rate of the flow field. With the data collected in this study, we can calculate $\dot{\epsilon}$ and λ as follows. The strain rate $\dot{\epsilon}$ as the droplet nears snap off can be estimated²⁸ as $\dot{\epsilon} = -\frac{2}{D_n} \frac{dD_n}{dt}$, which results in $\dot{\epsilon} = 2400\text{s}^{-1}$ for the data presented in Figure 5.7. The relaxation time λ in dilute solutions can be estimated from Zimm theory²⁹

$$\lambda = \frac{6[\eta]\eta_s M_w}{\pi^2 RT} \quad (5.6)$$

where $[\eta]$ is the intrinsic viscosity of the polymer solution, η_s is the solvent viscosity, M_w is the polymer molecular weight, R is the gas constant and T the temperature. Even though the polymer concentrations used herein are far from dilute, we can use Eq. (5.6) to gain a rough idea of how close we are to the onset of elastic effects³⁰. Using $\eta_s = \mu_{DP} = 14.9\text{mPa}\cdot\text{s}$, $[\eta] = 57\text{mL/g}$ and $M_w = 137\,000\text{g/mol}$, we calculate $\lambda = 3 \times 10^{-5}\text{s}$. Thus $De = 0.07$, significantly below the transition region. Even though the solution viscosity is high, and this retards polymer relaxation, the molecular weight is low enough that the chains can fully recoil when strained, and hence elastic effects are not seen. An analysis of the relationship $\mu_{DP} = \mu_{DP}(x_{PLG})$ (data not shown) reveals that a doubling of the DP polymer fraction, to $x_{PLG} = 18\%$, would result in $De \approx 1$. Similarly, a doubling of the polymer molecular weight to $M_w = 270\,000\text{g/mol}$ would also result in $De \approx 1$. For typical manufacturing of drug loaded polymer microspheres, these points represent extreme operating conditions, yet there are certainly other applications where high polymer concentration and/or M_w could lead to elastic effects being observed.

Moving now to an analysis of the effects of dynamics interfacial tension, in essence, we expect the interfacial tension at the moment of snap-off to differ significantly from its long-time value. One conventional approach for characterizing the dynamic interfacial tension is the drop weight method²³. We performed such measurements, despite expecting the conditions during XME to differ somewhat from the dynamics of gravity driven drop break off from a needle tip. To probe different time scales for droplet production, we use a variety of needle diameters and volumetric flow rates, all while maintaining the droplet production in the dripping regime. The results are shown in

Figure 5.8. As can be seen, the interfacial tension of the decanol system does not change significantly across the range of droplet frequencies studied, with a relative standard deviation of 6%. But the PLG system shows a large effect, dropping from about $\gamma = 11\text{mN/m}$ at $\Delta t = 0.5\text{s}$ to $\gamma = 3\text{mN/m}$ at $\Delta t = 30\text{s}$. For typical XME experiments conducted here, the time scale for droplet production $\Delta t = \pi D^3/6Q_{\text{DP}}$ ranges from $\Delta t \approx 0.01\text{s}$ to $\Delta t \approx 1\text{s}$. Due to the dripping-jetting transition, we are unable to directly measure the interfacial tension at time scales less than $\Delta t \approx 0.5\text{s}$, and thus we turn to modeling to predict what may occur at shorter times. The phenomenological Rosen equation²⁴ predicts that at times infinitesimally close to zero, the interface will behave as if there is no surfactant adsorbed, and at very long times, surfactant will completely cover the interface, and the interfacial tension will plateau. In between, a power law dependence is predicted:

$$\frac{\gamma_0 - \gamma(t)}{\gamma(t) - \gamma_\infty} = \left(\frac{t}{\tau}\right)^{-n} \quad (5.7)$$

where γ_0 and γ_∞ are the interfacial tensions at time zero and infinity, and τ and n are fitting constants. We find γ_0 by measuring the interfacial tension when no surfactant is present, and γ_∞ by forming droplets over time periods greater than 500s. Using these initial and terminal values, and then adjusting τ and n to fit the intermediate data, we find that the Rosen equation fits our drop weight method data well over the time period observed, with the average error being about 5%.

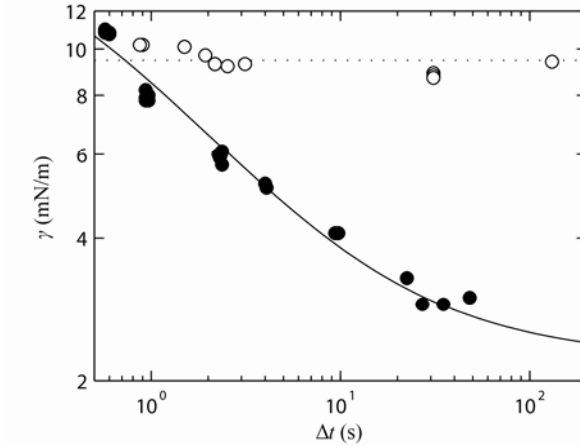


Figure 5.8 – Interfacial tension γ as a function of drop period Δt for the PLG (filled circles) and decanol (open circles) systems, as measured using the drop weight method²³. The dotted line shows the average value of γ for the decanol system, and the solid line is a fit of the PLG data to Eq. (5.7).

Summarizing the non-ideal effects investigated thus far, we have seen that shear thinning viscosity and fluid elasticity do not play a role in the dynamics of XME under the conditions studied here. Interfacial tension, however, seems to change significantly over large time scales, and thus could be responsible for the differences seen in droplet size vs. production rate for the decanol and PLG systems. Using the insight provided by the Rosen equation, we could directly substitute Eq. (5.7) into Eq. (5.5) to see if the results of Figure 5.5 can be predicted. However, when γ is not constant, both Ca and We are affected simultaneously. Thus it is more instructive to use Eq. (5.5) to directly compute γ using the measured flow rates and droplet diameters, as a function of the XME dripping period, shown in Figure 5.9. As expected, the results for the simple decanol system show no sign of dynamic interfacial tension, and yield an average value, 9.63mN/m, consistent with what was measured via the drop weight method, 9.47mN/m. The scatter in the data is a consequence of the fact that $\gamma \sim D^3$, implied by Eq. (5.1), (5.2)

and (5.3), making the computed tension very sensitive to small errors in the measurement of droplet diameter.

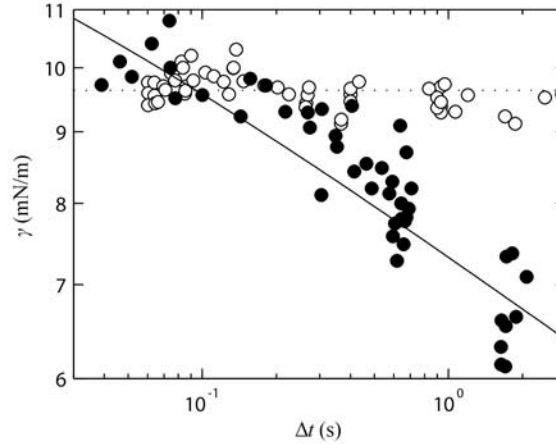


Figure 5.9 – Interfacial tension γ as a function of drop period Δt for the PLG (filled circles) and decanol (open circles) systems as calculated from Eq. (5.5) during XME. The dotted line shows the average value of γ for the decanol system, and the solid line is a fit of the PLG data to the Rosen equation.

The PLG data do show the expected trend of decreasing interfacial tension with increasing droplet period, and the measured values are within the range observed previously, however the values are significantly lower than what is predicted by Eq. (5.7) at comparable dripping frequencies in both processes. We again use the Rosen equation to fit the γ – Δt curve, and assume the same initial and terminal values γ_0 and γ_∞ , with fit parameters shown in Table 5.3. The time constant τ , which moves the curve horizontally, is an order of magnitude smaller for the XME data. This is not surprising given that during XME, convection drives surfactant to the droplet interface, an effect not seen in the drop weight method. Thus the droplet interface achieves a given surfactant concentration an order of magnitude faster during XME. The exponent n , which changes the slope of the curve in log-log space, is about 1/3 of that measured via the drop weight

method. A smaller slope is also predictable due to the strong convection present during XME. When considering the strong convective forces, it could be considered surprising that interfacial tension changes at all as a function of drop period. However, this result could be explained by a slow surfactant adsorption process. Regardless, it seems that dynamic interfacial tension can be held solely responsible for the subtle non-ideal behavior we observe in the PLG system.

Table 5.3 – Rosen equation fit parameters.

Method	γ_0 (mN/m)	γ_∞ (mN/m)	τ (s)	n
Drop weight	19.2	2.2	0.49	0.75
XME	19.2	2.2	0.04	0.25

Although dynamic interfacial tension provides an adequate explanation for the significant changes in D at low Q_{DP} seen in Figure 5.5, it is interesting to note that there is no significant dynamic interfacial tension effect observed in Figure 5.4, where D is plotted as a function of dv/dz . Thus we are tempted to simplify the problem, and test the validity of Eq. (5.5) using a constant, average interfacial tension. This simplification is further reinforced by the following fact. We saw before that when calculating γ from measured values of D , errors are amplified because $\gamma \sim D^3$. However, when observing D in an environment with changing γ , the dynamics are dampened because $D \sim \gamma^{1/3}$. Using this methodology, we construct Figure 5.10, assuming for the PLG system $\gamma = 9.6 \text{ mN/m}$, which is the average value in Figure 5.9 for drops produced across the same frequency range. We find that the model does predict well the relationship between Ca and D/D_0 for both the decanol and PLG systems. Yet we have argued that dynamic interfacial tension is present in the XME system. We expect if dynamic interfacial tension is

present, as Ca is increased, smaller drops will be made at a higher frequency. This shorter time period between drops means that the interfacial tension at the time of snap off will be higher, and thus the droplets will be slightly larger than otherwise expected. Thus, when dynamic interfacial tension is present in XME, instead of $D/D_0 \sim Ca^{-0.5}$, the exponent of Ca should be higher (closer to zero). Testing this quantitatively, a power law fit to the PLG interfacial tension vs. time data presented in Figure 5.9 results in $\gamma \sim \Delta t^{-0.11}$. Using the fact that $D \sim \gamma^{1/3}$ and combining with Eq. (5.1), we find that the exponent of Ca should be $-0.5+0.11/3 = -0.46$. Indeed, a power law fit to the PLG data presented in Figure 5.10 reveals $D/D_0 \sim Ca^{-0.46}$. Consequently we conclude that an assumption of constant interfacial tension results in minimal error when calculating Ca and using Eq. (5.5), and the deviations from Eq. (5.5) can be readily determined if the relationship between γ and Δt is known.

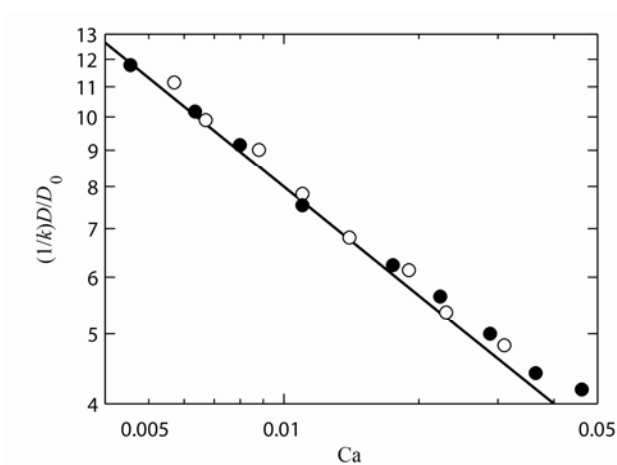


Figure 5.10 – Scaled diameter ratio $(1/k)D/D_0$ as a function of capillary number Ca for the PLG (filled circles) and decanol (open circles) systems. The solid line is a prediction based on Eq. (5.5), $(1/k)D/D_0 = Ca^{-1/2}$.

In the end, our goal is to understand the effects processing parameters have on the size of the particles produced, and the rate of their production, and use this information to manufacture monodisperse polymer particles. Despite the sometimes non-ideal behavior that is seen when polymers and surfactants are introduced to the system, particles can be produced over a wide range of sizes and rates with a remarkable degree of precision. An analysis using the automated sizing technique of $n = 261$ wet particles over a 10 min period reveals a relative standard deviation (RSD) of 1.2%, while an independent analysis of $n = 81$ close-packed, fully dry particles results in $RSD = 1.6\%$. See Figure 5.11 and Figure 5.12 for additional details. This small variability demonstrates that the ability to manufacture uniform particles via XME is limited primarily by the operator's ability to control those parameters that appear in the size model, namely the flow rates Q_{DP} and Q_{CP} .

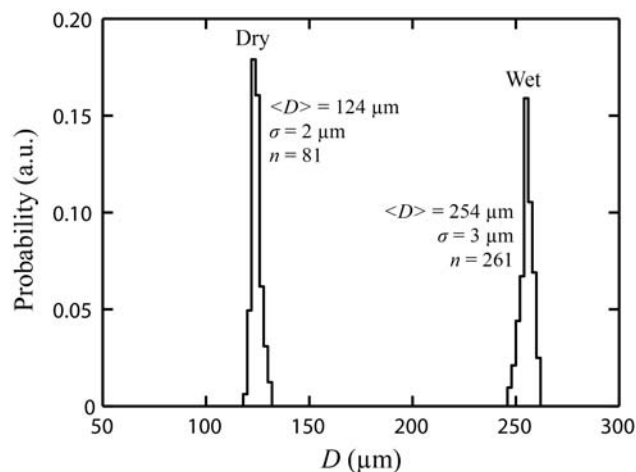


Figure 5.11 – Diameter histograms for wet and dry drug loaded PLG particles produced over a 10min time period, measured independently via image analysis. The dry particles are shown in Figure 5.12. The variables $\langle D \rangle$, σ , and n refer to the mean, standard deviation, and number of samples, respectively. We observe the ratio of dry and wet particle diameters to be $D_{\text{dry}}/D_{\text{wet}} = 0.488$, which is close to the expected value of $D_{\text{dry}}/D_{\text{wet}} = (\rho_{\text{wet}}/\rho_{\text{dry}} x_{\text{DP}})^{1/3} = [(1)(0.122)]^{1/3} = 0.496$ because the dry particles have no porosity and the polymer has nearly identical density to the solvent.

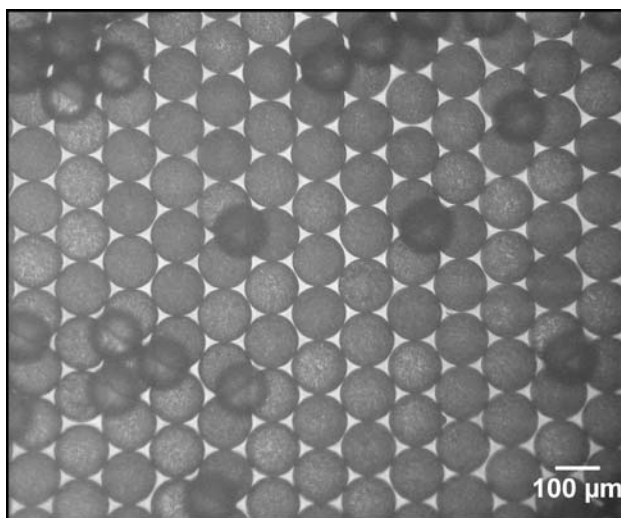


Figure 5.12 – Fully dry drug loaded PLG particles produced over a 10min time period using the 60 μm membrane shown in Figure 5.2(b), at a shear rate of $dv/dz = 2150 \pm 110 \text{ s}^{-1}$. In some locations two layers of particles can be seen. The mean diameter is 124μm with

a standard deviation of 2 μm ($n = 81$). A histogram of the sizes is shown in Figure 5.11.

From an operational viewpoint, it is important to understand the influence the various model parameters have on the process. First, the production rate per pore calculated on a mass basis, i.e. the mass flow rate, dm/dt , is simply the product of the DP solids fraction x_{DP} with the total mass flow rate of the DP, $dm/dt = x_{\text{DP}}\rho_{\text{DP}}Q_{\text{DP}}$. Increases in x_{DP} make dm/dt rise proportionally, but make μ_{DP} , λ and Oh_{DP} increase much more quickly, decreasing process robustness. In practice, solids loadings between 5% and 15% are common. The flow rate Q_{DP} is the most logical parameter for raising dm/dt , but can not be increased indefinitely. Changes to Q_{DP} modify We , the ratio of inertial forces to interfacial forces. When $\text{We} > 1$, inertia dominates interfacial tension, and a jet is formed from the membrane pore. Above this dripping-jetting transition, droplets break off far from the membrane pore and are typically polydisperse¹¹. Thus for normal operation, production is optimal when Q_{DP} is chosen such that $\text{We} \approx 1$, which occurs for $Q_{\text{DP}} = (\gamma D_0^3 / \rho_{\text{DP}})^{1/2}$. At this condition, the production rate per pore is $dm/dt = x_{\text{DP}}(\rho_{\text{DP}} D_0^3 \gamma)^{1/2}$. For further increases in dm/dt , it makes sense to increase the number of pores until the desired production rate is achieved. If each pore releases droplets into a common CP, care must be taken in spacing the pores so that the presence of one droplet does not interact with the growth and break off of nearby droplets. Because a force-free droplet in a shear field only perturbs the flow field $\sim (D/r)^{-3}$, a single line of pores arranged diagonally relative to the flow would only need to be spaced by a few droplet diameters perpendicular to the flow to avoid perturbations from the single pore result. A useful property of the XME system is that although variations in pore permeability might cause

Q_{DP} to vary from pore to pore, in the dripping regime this effect does not lead to a significant change in droplet diameter among pores.

Using the size models and physical and geometric parameters, we can predict the range of particle sizes that are achievable using our XME system. On the large end, particles can be manufactured up to the size restrictions set by the geometry of the system. In order to make monodisperse spherical particles, care must be taken that gravitational forces do not exceed interfacial forces, i.e. the Bond number does not exceed unity, $Bo = \rho_{DP}D^2g/\gamma < 1$. For our system, this means that particles must remain below about 800 μm in the wet state, or 400 μm when fully dry. On the small end, particles can be made as small as $D/D_0 \approx 2$, but only if high shear stresses are employed, which can be achieved through high μ_{CP} , high Q_{CP} , or small H . Thus the minimum size of particles is set by D_0 , which we found to be at minimum $D_0 = 15\mu\text{m}$ for our 300 μm thick membranes, resulting in 30 μm wet or 15 μm dry particles. However, as reported by Yanagishita et al.³¹, advanced manufacturing techniques can be used to produce membranes and particles down to $D \approx D_0 \approx 100\text{nm}$.

When manufacturing particles via XME, care must be taken such that the particles remain uniform until they are ready to be used. Unfortunately, natural processes such as coalescence and shear break up act to widen the particle size distribution. In simple systems such as the decanol-water system studied here, droplets readily coalesce due to the absence of surfactant. Addition of a surfactant does stabilize the particle size distribution from growing larger, but also decreases the interfacial tension, and thus weakens the droplets against shear breakup. In the PLG system studied here, droplets are

stabilized by the surfactant PVA, and the interfacial tension continues to decrease over a droplet's lifetime as additional surfactant is adsorbed to the interface. Our goal is to prevent shear breakup of the nascent PLG particles until such point that the solvent is extracted, thus generating solid particles with a stable size distribution.

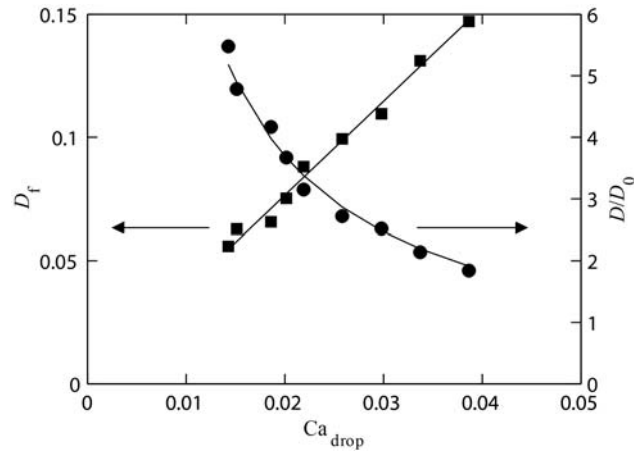


Figure 5.13 – Droplet deformation D_f , (squares) and droplet size D/D_0 (circles) as a function of Ca_{drop} for the PLG system. The deformation data utilize a linear fit, while the size data are fit according to Eq. (5.5). Rupture occurs at $D_{f,c} = 0.4$. The figure uses the same data set presented in Figure 5.10.

Because shear is used to generate the initial monodisperse emulsions, the operating conditions during XME are inherently close to the critical condition where breakup of droplets occurs. For insight into this potential problem, we look to the results of Bentley and Leal³² who used a four-roll mill to experimentally measure the deformation and point of breakup as a function of droplet capillary number, Ca_{drop} , viscosity ratio, λ , and a flow parameter, α , which characterized the relative importance of elongation and shear in the flow field. In their work, which primarily studied pure fluids, they utilized a deformation parameter D_f to measure droplet deformation, where $D_f = (L - B)/(L + B)$, and L and B are the lengths of the droplet's major and minor semiaxes,

respectively. It was shown that for $\lambda > 1$, D_f will increase linearly with Ca_{drop} until it reaches $D_{f,c} \approx 0.4$, at which point the droplet will rupture.

The critical value of Ca_{drop} where $D_f = 0.4$ depends on λ and α , but typically varied from $0.1 < Ca_{\text{drop}} < 0.5$ for $\lambda > 1$. Using the relationship between the different capillary numbers, $Ca_{\text{drop}} = 0.5CaD/D_0$, we plot D_f and D/D_0 against Ca_{drop} using the same PLG data set that was previously presented. Then we calculate the ratio of Ca needed to generate a droplet of a given size to the critical value where rupture is expected to occur, Ca_c . Figure 5.13 and Figure 5.14 show these results.

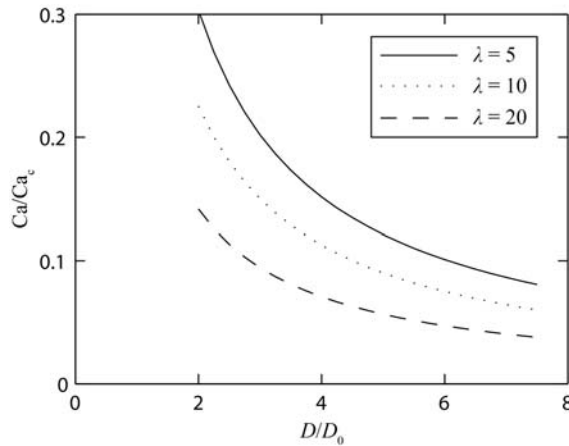


Figure 5.14 – Ratio of Ca to the critical value Ca_c where droplet rupture occurs, calculated as a function of the diameter ratio D/D_0 and viscosity ratio λ . The solid line represents $\lambda = 5$, the dotted line is $\lambda = 10$, and the dashed line is $\lambda = 20$.

We know already that XME can be used to generate emulsions down to $D/D_0 \approx 2$, but from these calculations we learn that the process is near an unstable operating point, where a small increase in shear rate downstream of the membrane pore could result in $Ca > Ca_c$. As can be seen, increasing λ increases the stability of the system against shear breakup. Fortunately, in a laminar flow, after a droplet is generated it will tend toward a position away from the wall²⁹, where the shear rate is lower. But care must be taken in

constructing the areas downstream of the membrane pore, as any bends or obstructions will increase the local shear rate, again increasing the likelihood of breakup. This potential problem can be avoided through intelligent apparatus design, by expanding channel dimensions downstream of the pore, thus decreasing velocities and shear rates and thereby increasing the likelihood that the final size distribution will be uniform.

5.5 Summary

We have shown that XME is a robust technique that can be used for the production of complex polymeric particles as well as simple emulsion droplets. The relationship between the size of droplets and the CP shear rate, derived elsewhere from first principles, was shown to apply equally well to the simple decanol-water system and a complex system containing a dissolved polymer, drug, and surfactant. In contrast, the polymer system showed an unexpected scaling of droplet size as a function of the DP flow rate, which we have shown to be consistent with the presence of dynamic interfacial tension. The inferred interfacial tension at a given dripping period was significantly lower than values measured independently at the same period using the drop weight method, which is not too surprising in light of the stagnant nature of the outer fluid in the latter method, slowing surfactant transport to the interface. The CP velocity profile and the thinning dynamics of the DP droplet neck were both directly observed, and both were consistent with theoretical predictions for Newtonian fluids, indicating shear-thinning viscosity and fluid elasticity are negligible. Detached droplets were seen to have an ellipsoidal deformation, which increased linearly with the capillary number. Finally, the distribution of wet droplet sizes was consistent with measurements from close-packed

arrays of dry particles, and both result in a relative standard deviation of between 1 and 2%. In conclusion, over a wide range of conditions, the XME process can be used to manufacture monodisperse droplets of predictable size, even when the fluids contain dissolved polymers and surfactants.

5.6 Acknowledgements

We thank O. M. Guzman for her work on the particle velocimetry technique. This research was supported by Merck & Co., Inc., the NSF Research Experience for Undergraduates program, and the University of Pennsylvania LRSM.

5.7 References

- (1) Joscelyne, S. M.; Trägårdh, G. *J. Membrane Sci.* **2000**, *169*, 107-117.
- (2) Siepmann, J.; Faisant, N.; Akiki, J.; Richard, J.; Benoit, J. P. *J. Controlled Release* **2004**, *96*, 123-134.
- (3) Berkland, C.; King, M.; Cox, A.; Kim, K.; Pack, D. W. *J. Controlled Release* **2002**, *82*, 137-147.
- (4) Utada, A. S.; Lorenceau, E.; Link, D. R.; Kaplan, P. D.; Stone, H. A.; Weitz, D. A. *Science* **2005**, *308*, 537-541.
- (5) Mason, T. G.; Bibette, J. *Langmuir* **1997**, *13*, 4600-4613.
- (6) Berkland, C.; Kim, K. K.; Pack, D. W. *J. Controlled Release* **2001**, *73*, 59-74.
- (7) Okushima, S.; Nisisako, T.; Torii, T.; Higuchi, T. *Langmuir* **2004**, *20*, 9905-9908.
- (8) Kobayashi, I.; Mukataka, S.; Nakajima, M. *Langmuir* **2005**, *21*, 7629-7632.
- (9) Vladisavljevic, G. T.; Williams, R. A. *Adv. Colloid Interface Sci.* **2005**, *113*, 1-20.
- (10) Gijsbertsen-Abrahamse, A. J.; van der Padt, A.; Boom, R. M. *J. Membrane Sci.* **2004**, *230*, 149-159.
- (11) Meyer, R. F.; Crocker, J. C. *Phys. Rev. Lett.* **2009**, *102*, 194501.
- (12) Freitas, S.; Merkle, H. P.; Gander, B. *J. Controlled Release* **2005**, *102*, 313-332.
- (13) Peng, S. J.; Williams, R. A. *Chem. Eng. Res. Des.* **1998**, *76*, 894-901.
- (14) Abrahamse, A. J.; Padt, A. v. d.; Boom, R. M.; Heij, W. B. C. d. *AIChE J.* **2001**, *47*, 1285-1291.
- (15) van der Graaf, S.; Schroën, C. G. P. H.; van der Sman, R. G. M.; Boom, R. M. *J. Colloid Interf. Sci.* **2004**, *277*, 456-463.
- (16) Husny, J.; Cooper-White, J. J. *J. Non-Newton. Fluid* **2006**, *137*, 121-136.
- (17) Gasparini, G.; Kosvintsev, S. R.; Stillwell, M. T.; Holdich, R. G. *Colloid Surface B* **2008**, *61*, 199-207.
- (18) Rayleigh, L. *P. R. Soc. London* **1879**, *29*, 71-97.
- (19) Buckingham, E. *Phys. Rev.* **1914**, *4*, 345.

- (20) Saboni, A.; Alexandrova, S. *AIChE J.* **2002**, *48*, 2992-2994.
- (21) Cheng, Y. H.; Illum, L.; Davis, S. S. *J. Controlled Release* **1998**, *55*, 203-212.
- (22) Li, M.; Rouaud, O.; Poncelet, D. *Int. J. Pharm.* **2008**, *363*, 26-39.
- (23) Yildirim, O. E.; Xu, Q.; Basaran, O. A. *Phys. Fluids* **2005**, *17*, 062107.
- (24) Eastoe, J.; Dalton, J. S. *Adv. Colloid Interface Sci.* **2000**, *85*, 103-144.
- (25) Holmes, D. B.; Vermeule, Jr. *Chem. Eng. Sci.* **1968**, *23*, 717-722.
- (26) Rayner, M.; Tragardh, G.; Tragardh, C. *Colloid Surface A* **2005**, *266*, 1-17.
- (27) Stillwell, M. T.; Holdich, R. G.; Kosvintsev, S. R.; Gasparini, G.; Cumming, I. W. *Ind. Eng. Chem. Res.* **2007**, *46*, 965-972.
- (28) Amarouchene, Y.; Bonn, D.; Meunier, J.; Kellay, H. *Phys. Rev. Lett.* **2001**, *86*, 3558.
- (29) Macosko, C. W., *Rheology: principles, measurements, and applications*. Wiley-VCH: 1994.
- (30) Tirtaatmadja, V.; McKinley, G. H.; Cooper-White, J. J. *Phys. Fluids* **2006**, *18*, 043101.
- (31) Yanagishita, T.; Fujimura, R.; Nishio, K.; Masuda, H. *Langmuir* **2009**, *26*, 1516-1519.
- (32) Bentley, B. J.; Leal, L. G. *J. Fluid Mech.* **1986**, *167*, 241-283.

Chapter 6: Future Work

In the end, the desired outcome of this project was to demonstrate that cross-flow membrane emulsification (XME) can be used for the production of drug-loaded polymer microspheres with controllable release profiles that exceed the performance of existing commercial products. While the original goal has not been met, the tools to accomplish this are in place such that a researcher need only follow the recipe presented in this chapter to make the proposed demonstration. This chapter is organized as follows. First, we lay out the requirements for designing long-acting release (LAR) formulations in general, and specifically a one month depot formulation of haloperidol, our model drug of choice. Then we review existing literature on immediate and LAR haloperidol formulations. This is followed by a review of the parameters that can be tuned in order to achieve the desired release duration and rate. Finally, we end with what experiments would need to be run in order to complete the formulation design.

6.1 Formulation Requirements

The basic requirements for LAR formulations are that they are sterile, physically and chemically stable for at least two years when refrigerated, and stable for at least one week at room temperature. Additionally, the product should be formulated so that no greater than 3 mL per injection site need be administered, and the product should be easily syringable (can be pushed through a syringe without requiring excessive force) through a 20 gauge 1.5 inch needle. Additional requirements that would improve upon existing formulations are that an LAR product should not exhibit any burst release, and

should produce a near-constant release rate that is approximately equal to the average elimination rate for the drug.

The model drug studied here, haloperidol, is especially well suited for controlled release applications. The drug is indicated for use in the treatment of schizophrenia, as well as the control of tics associated with Tourette's Disorder. It is well suited for controlled release applications¹ due to the low daily dose, the drug hydrophobicity, high non-compliance rates in the intended treatment group, and existence of dose-proportional side effects². Furthermore, the wealth of literature available on the drug aids in the formulation design. Haloperidol is typically supplied as an oral dosage form, taken one or two times per day³. For acute use, haloperidol injection USP is prescribed, and for chronic use, a LAR formulation of haloperidol decanoate is prescribed for monthly administration³. In this case study, we will attempt to design a formulation that exceeds the performance of the existing haloperidol decanoate product.

For a theoretical haloperidol LAR formulation, a review of existing data is helpful in the design. An assortment of physical and chemical property data are provided in Chapter 3, and the reader is directed there for further information. Table 6.1 displays pharmacokinetic data for intravenous and oral haloperidol, and intramuscular haloperidol decanoate.

Table 6.1 – Pharmacokinetic parameters for haloperidol.³⁻⁵

Parameter	Mean	SEM ^a
Elimination half life (hr)	26.2	8.0
Volume of distribution (L/kg)	21.7	6.9
Clearance (mL/kg/min)	10.8	2.6
Elimination constant (1/hr)	0.030	-
Bioavailability (relative AUC _{0-∞} ^b)	0.65	0.14
Plasma concentration for 10 mg oral dose (ng/mL)	7.79	4.79
Plasma concentration for 100 mg decanoate dose (ng/mL)	7.95	4.94
Plasma concentration before next dose (ng/mL)	2.62	0.27
Dosing rate for 70 kg man (mg/day)	2.8	-

^aSEM = standard error of the mean, ^bAUC_{0-∞} = area under the concentration – time curve

A number of parameters from this table are relevant. First, the drug has an incredibly large volume of distribution, indicating that it is absorbed in both the blood stream and tissues throughout the body. The drug has a fairly high bioavailability, and thus the average daily dose administered via parenteral administration should not vary significantly from the daily oral dose. Specifically, it has been found that patients receiving 10 mg/day oral haloperidol achieve the same steady state average blood serum concentration when 100 mg/month haloperidol decanoate injection is utilized. We can also calculate the desired dosing rate (i.e. the amount of haloperidol released per day) by multiplying the clearance by the desired plasma concentration, yielding about 3 mg/day. Thus, this is the target quantity to be released from our PLG microspheres.

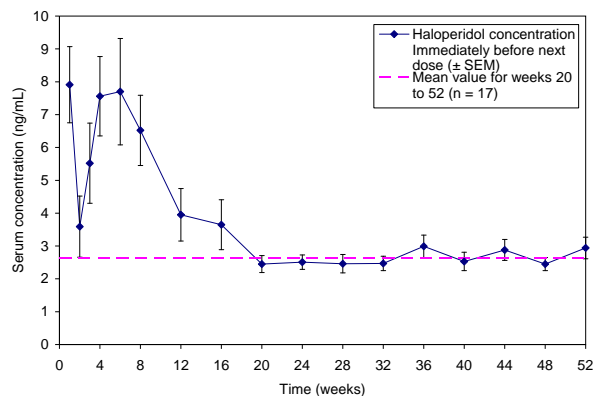


Figure 6.1 - Plot of average haloperidol blood serum concentration following a loading dose regimen of 100 mg haloperidol equivalent (administered as haloperidol decanoate). The dosing schedule was once weekly for the first four weeks, then once every two weeks until week eight, and once every four weeks after week eight.⁵

To achieve a release rate of 3 mg/day over the course of 30 days, then 90 mg must be administered. A typical formulation might start with 20% drug loading (i.e. 1:4 drug to polymer ratio in the solvent). If it is assumed that the encapsulation efficiency during the emulsification process is 100% then a 20% drug loading of the microspheres results. Thus, 450 mg of microspheres would be administered. To suspend the microspheres, we assume that 100 mg microspheres per 1 mL of suspending medium would be used, and thus our injection volume would be 4.5 mL of medium plus about 0.5 mL for the microspheres, yielding 5 mL. Thus two separate injections would be required, in order to stay under the 3 mL per injection site guideline. This works out to be very similar to the marketed naltrexone LAR formulation, which has 112 mg microspheres per 1 mL of diluent, and is administered as two separate injections.⁶

6.2 Previous studies of haloperidol LAR formulations

Many other researchers have published data on LAR formulations of haloperidol. Wang et al.⁷ used melt extrusion to generate haloperidol loaded rods at 40% drug loading in a matrix of 50:50 poly(DL-lactide-co-glycolide) (PLG) (inherent viscosity 0.47 dL/g), and compared this formulation to a 20% drug loaded solvent cast pellet.⁸ Although in vitro release experiments showed a roughly 7 day lag phase before significant drug was released from the rods, the same rods demonstrated in vivo in rats a serum concentration maximum on day 7, and continued release into the serum up until about day 40. The study demonstrated that melt extrusion could be used to rapidly make implants that provide fairly consistent release over a prolonged period.

Other studies investigating incorporation of haloperidol into PLG microspheres were conducted by Cheng et al.⁹ and by Budhian et al.¹⁰⁻¹¹ Cheng et al. used high shear homogenization to generate particles, while Budhian et al. used ultrasonics, and both used a batch production system. All found relatively constant release rates in vitro, and both studies demonstrated very low encapsulation efficiency and final drug loading, which is not surprising given that the particles produced were between 0.1 and 10 μm . Finally, Budhian et al. reported that the diffusivity of haloperidol in 50:50 PLG particles $8 \times 10^{-18} \text{ cm}^2/\text{s}$, a finding that is useful for prediction of drug release rates from particles of different sizes.

6.3 Future XME and in vitro release experiments

The next step in the product design is the generation of microspheres that release at a rate of 3 mg/day at a drug loading of 20%. Finding guidance from the work of other researchers, it appears that 50:50 PLG copolymers of intermediate inherent viscosity are

appropriate for developing once monthly LAR formulations of haloperidol. Because PLG polymers break down by cleavage of the ester bond between lactide and/or glycolide residues, a higher inherent viscosity (which equates to higher initial molecular weight) results in a longer time period before the polymer completely breaks down and the microsphere disintegrates. Thus polymer inherent viscosity is a key parameter that can be adjusted to affect drug release rate and duration, in addition to microsphere size. Based on this and other data reported thus far, a starting formulation for XME would look like that presented in Table 6.2.

Table 6.2 – Starting compositions for once monthly haloperidol LAR formulation.

Continuous Phase Component	Composition (%)	Dispersed Phase Component	Composition (%)
poly(vinyl alcohol)	1	50:50 PLG (I.V. 0.47 dL/g)	9.6
haloperidol	trace *	haloperidol	2.4
water	99	dichloromethane	88

* concentration needed to achieve saturation

At this point, the rate of drug release for a microsphere of a given size and composition would need to be determined. The best way to accomplish this is to run a single XME experiment, and use the continuous phase (CP) flow rate to change microsphere size, while holding all other process variables constant. It is recommended that about 4 different monodisperse size samples be collected, each containing at least 200 mg of microspheres. Because the CP is saturated with the drug, no mass transfer should occur during emulsification, and thus all samples should exhibit approximately 100% encapsulation efficiency. Using the procedures outlined in Chapter 3, the particles should be hardened, washed, filtered and dried.

Subsequent to the generation of the particles, the in vitro drug release can be measured using the existing apparatus described in Chapter 3. Briefly, the dry microspheres are added to a dialysis chamber along with a small amount of release medium, and this chamber is sealed and placed in a larger reservoir of medium. The release medium recommended is phosphate buffered saline at pH of 7.4 and a temperature of 37°C. To better simulate the release environment in vivo, a surfactant such as polysorbate 80 should be added to the medium. The surfactant improves microsphere wetting, and because of the very low solubility of haloperidol in water at pH = 7.4, it also acts to better simulate the sink conditions of the body. In addition, an agent such as sodium azide should be employed in the release medium to control microbial growth. The concentration of haloperidol in solution can be monitored using the inline UV spectrometer, and if the concentration exceeds approximately 10% of the equilibrium concentration (which is dependent on the surfactant), the release medium should be replaced. Drug release should be monitored until no changes are observed for at least two weeks, at which point the dialysis chamber should be removed and inspected for particle residue. If no residue is found, then the experiment is concluded, and the release rate, duration and total amount of drug released can be calculated.

6.4 Achieving the optimal release profile

Once a representative set of release experiments have been conducted, the protocol of Berchane et al. can be used to calculate what combination of monodisperse sizes should be combined to provide the closest match to the desired release profile.¹² This is possible because the release rate from a mixture of monodisperse sizes is simply

the weighted average of the individual release rates. In brief, their protocol calls for the user to begin with a cumulative solution to the diffusion equation,

$$\frac{M_t}{M_\infty} = 1 - \frac{6}{\pi^2} \sum_{j=1}^{\infty} \frac{1}{j^2} e^{-j^2 \pi^2 T / R^2} \quad (6.1)$$

where M_t / M_∞ is the ratio of mass released at time t to mass released at infinite time, R is the radius of the microsphere, and $T = \int_0^t D(t) dt$, where $D(t)$ is the drug diffusivity at time t , which is a function of polymer molecular weight, and thus is a function of time. The boundary and initial conditions used are $c(r = R, t > 0) = 0$ and $c(r, t = 0) = c_i$, where c is concentration and r is radial position. The diffusivity is linked to the polymer molecular weight through an empirical polynomial relationship, and molecular weight M_w decreases as a function of time, $M_w = M_w(t=0) \exp(-k_{\text{deg}} t)$, where k_{deg} is the degradation rate constant. In the fitting, it is assumed that there exists an initial diffusivity, D_0 , which explains the burst release, and this diffusivity is used until the calculated diffusivity $D(t)$ exceeds D_0 . The parameters D_0 and k_{deg} are the only parameters used to fit the release profile. This method has been demonstrated successfully in fitting release profiles for the drug piroxicam loaded into two different grades of PLG with three different microsphere diameters.

Modeling provides great validation that drug release can be explained by a combination of diffusion and degradation, but ultimately we want to use the model to predict the combination of particle sizes that will result in the desired release rate. Berchane et al. were limited to three different size fractions, set by the standard sieve sizes used to separate their initially polydisperse size distributions.¹² Still, they used a

non-linear least squares regression to minimize the squared error between the target release profile and a linear combination of the available profiles, and they achieved great success. Using XME, a much wider range of release profiles is possible, because a much wider range of particle sizes is possible. Instead of a discrete combination of monodisperse size distributions, the model can be used to create a smoothly varying function relating microsphere size and drug release rate from the initial release profiles. Modeling could then be used to generate a more detailed particle size population for use in constructing the ideal release profile, and a follow up XME experiment could be performed where the exact distribution is made within a single experiment.

With the methods in this chapter as a guide, we conclude that generation of an ideal once-monthly formulation of haloperidol-loaded PLG microspheres using cross-flow membrane emulsification is readily achievable. And after this goal is achieved, the methods can be expanded to a much wider class of drugs and release profiles, with the potential result being a significant improvement in human health.

6.5 References

- (1) Wischke, C.; Schwendeman, S. P. *Int. J. Pharm.* **2008**, *364*, 298-327.
- (2) Hummer, M.; Kemmler, G.; Kurz, M.; Kurzthaler, I.; Oberbauer, H.; Fleischhacker, W. W. *Am J Psychiatry* **1999**, *156*, 631-633.
- (3) Wei, F. C.; Jann, M. W.; Lin, H. N.; Piao-Chien, C.; Chang, W. H. *J Clin Psychiatry* **1996**, *57*, 298-302.
- (4) Holley, F. O.; Magliozzi, J. R.; Stanski, D. R.; Lombrozo, L.; Hollister, L. E. *Clin. Pharm. Ther.* **1983**, *33*, 477-484.
- (5) Jann, M. W.; Wei, F. C.; Lin, H. N.; Piao-Chien, C.; Chang, W. H. *Prog Neuropsychopharmacol Biol Psychiatry* **1996**, *20*, 73-86.
- (6) Dunbar, J. L.; Turncliff, R. Z.; Dong, Q.; Silverman, B. L.; Ehrich, E. W.; Lasseter, K. C. *Alcoholism: Clinical and Experimental Research* **2006**, *30*, 480-490.
- (7) Wang, C.-K.; Wang, W.-Y.; Meyer, R. F.; Liang, Y.; Winey, K. I.; Siegel, S. J. *J. Biomed. Mater. Res. Part B Appl. Biomater.* **2010**, *93B*, 562-572.

- (8) Metzger, K. L.; Shoemaker, J. M.; Kahn, J. B.; Maxwell, C. R.; Liang, Y.; Tokarczyk, J.; Kaness, S. J.; Hans, M.; Lowman, A. M.; Dan, N.; Winey, K. I.; Swerdlow, N. R.; Siegel, S. J. *Psychopharmacology (Berl)* **2007**, *190*, 201-211.
- (9) Cheng, Y. H.; Illum, L.; Davis, S. S. *J. Controlled Release* **1998**, *55*, 203-212.
- (10) Budhian, A.; Siegel, S. J.; Winey, K. I. *Int. J. Pharm.* **2007**, *336*, 367-375.
- (11) Budhian, A.; Siegel, S. J.; Winey, K. I. *Int. J. Pharm.* **2008**, *346*, 151-159.
- (12) Berchane, N. S.; Jebrail, F. F.; Andrews, M. J. *Int. J. Pharm.* **2010**, *383*, 81-88.